



HAL
open science

Development of signal processing algorithms for the detection of micro-emboli using a new TCD system

Maroun Geryes

► **To cite this version:**

Maroun Geryes. Development of signal processing algorithms for the detection of micro-emboli using a new TCD system. Signal and Image processing. Université François-Rabelais de Tours; Université libanaise, 2016. English. NNT: . tel-01445786

HAL Id: tel-01445786

<https://theses.hal.science/tel-01445786>

Submitted on 25 Jan 2017

HAL is a multi-disciplinary open access archive for the deposit and dissemination of scientific research documents, whether they are published or not. The documents may come from teaching and research institutions in France or abroad, or from public or private research centers.

L'archive ouverte pluridisciplinaire **HAL**, est destinée au dépôt et à la diffusion de documents scientifiques de niveau recherche, publiés ou non, émanant des établissements d'enseignement et de recherche français ou étrangers, des laboratoires publics ou privés.



UNIVERSITÉ FRANÇOIS RABELAIS DE TOURS

DOCTORAL SCHOOL OF ENERGY, MATERIAL, EARTH AND UNIVERSE SCIENCES
LABORATORY AND RESEARCH TEAM : Imaging and Brain Laboratory, Imaging and
Ultrasound Team, National Institute of Medical and Health Sciences Unit 930

AND

The Lebanese University

DOCTORAL SCHOOL OF SCIENCES AND TECHNOLOGY
LABORATORY AND RESEARCH TEAM : BIOMEDICAL GROUP, DEPARTMENT OF
PHYSICS AND ELECTRONICS

DOCTORAL DISSERTATION presented by :

Maroun Geryes

To be Defended on : 05 December 2016

in partial fulfilment of the requirements for the degree of: **Doctor of Philosophy**
From François Rabelais University of Tours, France and The Lebanese University,
Lebanon

Discipline/ Speciality : Science for Engineers / Biomedical Signal Processing

**Development of signal processing algorithms for the detection
of micro-emboli using a new TCD system**

Committee Members :

GIRAULT Jean-Marc	PhD-HDR, <i>Université François Rabelais de Tours, France</i>	Director
CHARARA Jamal	Professor, <i>Lebanese University, Beirut, Lebanon</i>	Director
HASSAN Walid	PhD, <i>Thomson Reuters</i>	Co-director
MÉNIGOT Sébastien	PhD, <i>François Rabelais University, Tours, France</i>	Invited
LE DUFF Alain	PhD-HDR <i>Université du Maine , Tours, France</i>	Report examiner
KOUAMÉ Denis	Professor, <i>Université Paul Sabatier, Toulouse, France</i>	Examiner
HAMADEY Ramsey	Professor, <i>American University of Beirut</i>	Report Examiner
MÉNIGOT Sébastien	PhD, <i>Université François Rabelais de Tours, France</i>	Invited

Acknowledgments

First, I would like to express my gratitude to my supervisors Dr. Jean-Marc Girault, Prof. Jamal Charara and Dr. Walid Hassan for their guidance and sincere advice and my profound gratitude goes to their efforts in each and every step involved in this dissertation.

I would also like to acknowledge Dr. Sébastien Ménigot who was always next to me particularly through my three period stays in France. Dr. Sébastien has been a tutor, a support and a friend.

I also thank Pr. Denis Kouamé and Dr. Alain Le Duff for being in the committee of my PhD and for their valuable comments. Special thanks to Pr. Ramsey Hamede for being in the committee of my dissertation and for his supportive comments.

The same gratitude goes to my colleagues in the Imaging and Brain Laboratory, Drs. Fatima Sbeity and Amira Zaylaa for their assistance in my project.

Special thank is due to Prof. Charles Tabet and Mrs. Tamara el Zein from the National Council for Scientific Research (Lebanon) for their support and accessibility.

I am deeply grateful to my parents for keeping me inspired throughout the thesis, and for their support and encouragement that are a constant source of power for me. I would like to thank all my friends who have always been there for me in my difficult times.

Abstract

Several years ago the detection of micro-embolic signatures through Transcranial Doppler signal monitoring has become a great interest due to the increasing number of Cerebrovascular Accidents they cause.

However, TCD clinical use has been limited by several hindering points such as the considerably long time needed for probe positioning, the decreased confidence in automatic detection, and the very short effective examination duration not sufficient to allow the detection of several micro-embolisms. The Holter system is a new generation of TCD systems developed in a way to overcome these drawbacks. Proposed solutions involve new enhancements such as the automatic positioning of the ultrasonic probe and the possibility of long-term recordings with the micro-emboli detection process being performed offline through a computer.

Moreover, although the algorithms implemented in Transcranial Doppler systems are well adapted for embolus detection, these algorithms do not allow a robust detection of the weak micro-embolus.

In this work, through offline detection, we have developed several signal processing tools and methods able to accurately detect weak micro-embolic signals. These methods were tested on real Doppler signals. Statistical measures, comprising the detection rate, the false alarm rate, and the relative intensity increase, were principally employed to evaluate the performance of the different detectors.

Keywords : Cerebrovascular Accidents; Micro-Embolus; Transcranial Doppler; Holter TCD; Signal Processing



Contents

Abstract	5
List of Figures	15
List of Tables	18
List of Acronyms	20
General Introduction	23
I Basic Conceptions	25
1 The study of embolism	27
1.1 Introduction	27
1.2 CerebroVascular Accidents and the Embolus	27
1.3 Statement of the problem and objectives	30
1.4 Conclusion	32
2 The Detection of Embolism	33
2.1 Introduction	33
2.2 The Transcranial Doppler ultrasound system	34
2.3 The Holter TCD system	34
2.4 Micro-embolus detection by TCD	36
2.5 The micro-embolus intensity increase relative to the moving blood	36
2.6 The Reference Off-line standard detection signal processing unit	38
2.6.1 Unit A: Doppler signal extraction, STFT and instantaneous energy calculation	39
2.6.2 Unit B: The gold standard of detection	43

2.6.3	Unit C: Artefact Rejection	43
2.6.4	Unit D: Standard micro-embolic detection	44
2.7	Conclusion	45
II	High Intensity Transient Signals Detection	47
3	A Micro-embolic Energy Detector based on Energy Fluctuations	49
3.1	Introduction	49
3.2	Micro-embolic detection based on energy fluctuations	49
3.3	Results	54
3.3.1	Training phase for the different thresholds	54
3.3.2	Demonstrating the homogeneity of our database	56
3.3.3	Comparison of the best testing phase results for the three detectors	56
3.4	The relative intensity increase of the smallest detectable micro-embolus	60
3.5	Conclusion	61
4	Coupling of a Negative Energy Fluctuations-Based Detector with Sub-band Decomposition: A Highly Performing Embolus Detection Technique	63
4.1	Introduction	63
4.2	The Micro-Embolic Short Time Fourier Transform Sub-band Detection Unit	64
4.3	Results	71
4.3.1	Sub-band detection with constant empirical thresholds	72
4.3.2	Sub-band detection with constant statistical thresholds	74
4.3.3	Sub-band detection with negative energy fluctuations-based time-varying threshold	75
4.3.4	Results of the testing phase for the different sub-band detectors	77
4.4	The relative intensity increase of the smallest detectable micro-embolus	78
4.4.1	Sub-band detection compared to whole band detection	80
4.5	Sub-band Decomposition achieved through Wavelet Packet Decomposition	85
4.5.1	The wavelet packet decomposition calculation	85
4.5.2	Results	88
4.6	Conclusion	90
5	Detection of Doppler Micro-Embolic Signals using High Order Statistics	93
5.1	Introduction	93
5.2	The reference offline skewness and kurtosis-based micro-embolic detection	94
5.3	Results	96
5.3.1	Training phase results	96
5.3.2	Testing phase results	97

5.4	Particular H-shaped peaks	98
5.5	The relative intensity increase of the smallest detectable micro-embolus	99
5.6	Conclusion	100
6	A Signal Processing Hierarchical Method for Artefact Rejection	103
6.1	Introduction	103
6.2	Pre-considerations	103
6.3	Rejecting Bidirectional Artefacts	105
6.3.1	Showers of Artefacts	107
6.3.2	Automatic Holter probe displacement Artefacts	109
6.4	Rejecting Unidirectional Artefacts	111
6.5	Results	111
6.6	Conclusion	113
7	Conclusions, limitations and outlook	115
7.1	Conclusions	115
7.2	Limitations	116
7.3	Outlook	116
	Bibliography	124
	Appendix	128

List of Figures

1.1	An illustration of an embolus in the carotid arteries blocking blood flow to a part of the brain and thus causing damage to brain tissues (National Heart, Lung and Blood Institute).	29
2.1	Holter Transcranial Doppler System (TCD-X, Atys Medical, Soucieu en Jarrest, France)	35
2.2	The background Doppler signal is estimated to be the trend represented by the smoothed version (in red) of the Doppler signal (in blue).	38
2.3	A typical embolus detection system including standard detection with constant thresholds. Unit A includes extracting 5s digital Doppler signal sequences from the SD card extracted from the Holter system, then calculating the STFT and the instantaneous energy from STFT estimators. Unit B includes establishing the gold standard of detection. Unit C includes the artefact rejection phase. Unit D represents the detection achieved using standard methods.	40
2.4	Spectrogram: A time-frequency representation obtained from Short Time Fourier Transform calculation. An embolic signature appears at the $t_0=1.05$ seconds.	43
3.1	Application of our detection technique based on negative energy fluctuations. a) The energy signal is represented as sum of two parts; one superior (cyan) and one inferior (green) to the smoothing curve (red). b) The smoothing curve is subtracted from the energy part inferior to it resulting in negative energy fluctuations (green). A negative time-varying envelope $E_{neg}(t)$ is then constructed (dark green). c) The smoothing curve is subtracted from the energy part superior to it resulting in positive energy fluctuations (cyan). The negative time varying envelope is opposed and applied as $-(E_{neg}(t))$ (blue).	52
3.2	The procedure of the new detection system proposed. After STFT and energy calculation, the energy signal is de-trended, and energy fluctuations are obtained. The micro-embolic energy detector is based on the negative part of the energy fluctuations, from which a time-varying threshold is constructed.	53
3.3	Detection and False Alarm rates obtained when constant empirical thresholds with values ranging between 3 dB and 9 dB, above the maximal background energy (defined in section 2.5) of the Doppler signal when no embolus is present (Ringelstein et al., 1998), are applied in the training phase. The best results are obtained with threshold setting of 5 dB with 67 % detection rate and 42 % false alarm rate.	55

3.4 Detection and False Alarm rates obtained when statistical constant thresholds $\lambda = \mu + m\sigma$ are applied with m values ranging between 3 and 6 in the training phase. The best training phase setting is obtained for $\lambda = \mu + 4.5\sigma$ with 70 % detection rate and 39 % false alarm rate. 55

3.5 Detection and False Alarm rates obtained when time-varying thresholds $\lambda(t) = \mu(t) + m\sigma(t)$ are applied in the training phase with m values ranging between 3 and 7. The best training phase setting is obtained for $\lambda(t) = \mu(t) + 6.5\sigma(t)$ with 90 % detection rate and 16 % false alarm rate. 55

3.6 Detection and False Alarm rates obtained when constant empirical thresholds with values ranging between 3 dB and 9 dB, are applied in the a) Training and b) Testing phases respectively. a) The best threshold setting is obtained with 5 dB. b) The best testing results are obtained with threshold of 5 dB with 66 % detection rate and 43 % false alarm rate. The results in a) and b) reflect the homogeneity of our database. 56

3.7 Detection and False Alarm rates obtained when statistical thresholds $\lambda = \mu + m\sigma$ are applied with m values ranging between 3 and 6 in the a) Training and b) Testing phases respectively. a) The best training phase setting is obtained with $\lambda = \mu + 4.5\sigma$. b) The best testing results are obtained with $\lambda = \mu + 4.5\sigma$ with 69 % detection rate and 41 % false alarm rate. The results in a) and b) reflect the homogeneity of our database. 57

3.8 Detection and False Alarm rates obtained when time-varying thresholds $\lambda(t) = \mu(t) + m\sigma(t)$ are applied with m values ranging between 3 and 7 in the a) Training and b) Testing phases respectively. a) The best training phase setting is obtained for $\lambda(t) = \mu(t) + 6.5\sigma(t)$. b) The best testing results are obtained for $\lambda(t) = \mu(t) + 6.5\sigma(t)$ with 89 % detection rate and 14 % false alarm rate. The results in a) and b) reflect the homogeneity of our database. 58

3.9 Comparison of the percentage detection and false alarm rate results for the energy detector based on negative energy fluctuations, standard detector with empirical threshold and detector with statistical threshold. The negative energy fluctuations-based detector reduces the FAR compared to the standard values and the values obtained with statistical thresholds. The detection rate achieved by the new detection system is increased compared to that achieved by standard detection and detection based on statistical thresholds. 59

3.10 Embolus Intensity Increases relative to background blood energy for a sample of 175 chosen embolic events. The smallest detectable embolus by detection with constant empirical threshold is as low as 5.8 dB. The smallest detectable embolus by detection with constant statistical threshold is as low as 4.1 dB. The smallest detectable embolus by the energy detector based on negative energy fluctuations is as low as 0.8 dB 61

4.1 An illustration of an embolus traveling in a blood vessel. The trajectory of blood flow is defined by a parabolic curve. The embolus travels on a single speed line in the vessel. 63

LIST OF FIGURES

4.2 Reducing the sample volume where the embolus is present to sample areas. Only RBCs traveling at the same speed line as the micro-embolus (same sample area) will be considered instead of considering all RBCs present in the whole sample volume. 64

4.3 Decomposition of the whole Doppler frequency spectrum into n ideal sub-bands through n ideal rectangular filters. 65

4.4 Sub-band Decomposition-based embolus detection system. After acquiring the Doppler signal, Short Time Fourier Transform is calculated for 5 second digital sequences. In Part 1, sub-band decomposition through a bank of n ideal frequency filters is applied. In Part 2, the instantaneous energy is estimated in each sub-band. Next in Part 3, the detection binary test is performed where the energy is compared to a detection threshold and the counter is triggered at energies exceeding the threshold. Lastly, in Part 4, all detections from each sub-band are merged and automatically counted. 67

4.5 An illustration of a 5 second extracted signal segment decomposed into 4 sub-bands. The decomposition is performed through a bank of four identical-width rectangular functions. 68

4.6 Sub-band detection process with negative energy fluctuations-based detector. Due to space complications we represent the detection process in sub-band 2 only. However, the same embolus detection process is applied in each sub-band. 69

4.7 a) An illustration of 2 micro-emboli that appear in two different sub-bands. The first micro-embolus appears in sub-bands one and three at the exact same position (1.217 s) and the second micro-embolus appears in the first and second sub-band at the same exact position (7.046 s). In both cases, when the micro-embolus is first detected in a sub-band, the time interval ± 0.025 s around the peak is applied on the following sub-bands to prevent the micro-embolus from being recorded again. This assures that the same micro-embolus is recorded only once in the final decision. b) An illustration of a micro-embolus that appears three times in three different sub-bands but at slightly different time positions. When the micro-embolus is first detected in the second sub-band, a time interval ± 0.025 s around the peak is applied on the following sub-bands to prevent the micro-embolus from being recorded again. This assures that the same micro-embolus is recorded only once in the final decision. 71

4.8 A comparison of the testing phase result of the 3 different sub-band detectors; those coupled with constant empirical thresholds, those with constant statistical thresholds and those with time-varying thresholds. 78

4.9 Embolus Intensity Increases relative to background blood energy for a sample of 175 chosen embolic events. The smallest detectable embolus by the sub-band detector coupled with empirical threshold is as low as 2.6 dB. The smallest detectable embolus by the sub-band detector coupled with statistical threshold is as low as 2.3 dB. The smallest detectable embolus by the sub-band detector coupled with the negative energy fluctuations based time-varying threshold is as low as 0.55 dB. 79

4.10	Comparison of the Detection Rate and False Alarm Rate for whole band detector and 4 sub-band detector with constant empirical thresholds.	80
4.11	Comparison of the Detection Rate and False Alarm Rate for whole band detector and 4 sub-band detector with constant statistical thresholds.	81
4.12	Comparison of the Detection Rate and False Alarm Rate for whole band detector and 4 sub-band detector with negative energy fluctuations-based time-varying threshold.	82
4.13	Comparison of the mean relative intensity increase for the 50 embolic signals calculated in both the whole band and the 4-sub-band.	83
4.14	a) A micro-embolus signature cannot be detected in the whole band Doppler signal upon setting a suitable constant empirical threshold. b) By applying sub-band decomposition and setting the suitable empirical threshold in each sub-band, the same micro-embolus signature is well detected in the first sub-band.	84
4.15	A 3rd order Wavelet Packet Tree. j denotes the decomposition level. At the 3rd decomposition, 8 different sub-band signals are obtained each denoted by a node and is correlated with an index (3,0 for example). LP denotes low pass filtering and HP high pass filtering. The third level signal $W_{3,0}$ to $W_{3,7}$ represent the frequency content of the original signal $x(t)$ within the band $0 - f_s/16$, $f_s/16 - f_s/8$, $f_s/8 - 3f_s/16$, $3f_s/16 - f_s/4$, $5f_s/16 - 3f_s/8$, $3f_s/8 - 7f_s/16$, and $7f_s/16 - f_s/2$ respectively, where f_s is the sampling frequency of the signal $x(t)$	86
4.16	An illustration of a 5 second extracted signal segment decomposed into 4 sub-bands by the wavelet packet decomposition.	87
4.17	A comparison of the testing phase result of the 3 different wavelet packet sub-band detectors; those coupled with constant empirical thresholds, those with constant statistical thresholds and those with time-varying thresholds.	90
5.1	A skewness and kurtosis based embolus detection system.	94
5.2	a) The Doppler energy signal. An empirical threshold is applied to obtain the micro-embolic standard detection discussed in chapter 3. b) Skewness signal calculated from the windowed energy signal. A statistical threshold is applied to complete the micro-embolic detection. The mean value of the skewness signal is 0.7 c) Kurtosis signal calculated from the windowed energy signal. A statistical threshold is applied to complete the micro-embolic detection. The mean value of the kurtosis signal is 3.2. Moreover, we choose in b) and c) three time positions: $t_1 = 0.72$ s during which an embolus is present, and $t_2 = 4.7$ s and $t_3 = 8.8$ s when no embolus is present. We detect in the case of absence of embolus: $S(t_2) \approx S(t_3) \approx 0.7$ and $K(t_2) \approx K(t_3) \approx 3.2$ while in the presence of embolus: $S(t_1) = 2.8 \neq S(t_3) \approx 0.7$ and $K(t_1) = 11 \neq K(t_3) \approx 3.2$	96
5.3	Detection and false alarm rate results for the skewness and kurtosis based detection. The results of the standard detection proposed in chapter 3 is also presented as a reference.	97
5.4	A demonstration of H-shaped peaks corresponding to micro-embolic detections.	98

LIST OF FIGURES

5.5	Embolus Intensity Increases relative to background blood energy for a sample of 175 chosen embolic events. The smallest detectable embolus by the detector based on skewness calculations is as low as 1.6 dB and that detected by the detector based on kurtosis calculations is also 1.6 dB.	100
6.1	Extracted part form Figure 2.3 in chapter 3 to show the artefact rejection phase position in our complete detection system.	104
6.2	A representation of the forward flow and reverse flow spectrograms of a 5 second signal segment containing 5 artefacts. Note that in many cases artefacts show a straight line running through all the vertical spectrum.	105
6.3	A representation of the forward flow and reverse flow energy signals calculated from the spectrograms in Figure 6.2.	106
6.4	A representation of the forward flow energy signal of Figure 6.3 after the artefact rejection procedure.	107
6.5	A representation of a shower of artefacts.	108
6.6	A representation of the forward and reverse flow energy signals of the spectrograms in Figure 6.5. By subtracting the reverse signal from the forward signal, the artefact showers are eliminated and the forward signal that had been embedded in the artefacts is retrieved.	109
6.7	A representation of an artefacts resulting from the automatic Holter probe displacement	110
6.8	A representation of the signature of an artefact resulting from probe displacement in the reverse and forward flow energy signals. Both flow signals are halted when the probe is in displacement. This artefact is rejected using the method of section 6.3.	110
6.9	A spectrogram representation showing a unidirectional forward artefact pointed out in red in the upper spectrogram.	112
6.10	A box plot showing the rise rates and fall rates of embolic and artefact signals. Embolic signal rise rates range between 0.015 s and 0.05 s while the fall rates range between 0.02 s and 0.03 s. Artefact signal rise rates range between 0.002 s and 0.01 s while the fall rates range between 0.002 s and 0.015 s.	113

List of Tables

2.1	A comparison between three sets of STFT parameters tested on 15 signals, a 64-point Hamming window equivalent in time to 0.015 seconds with an overlap of 65 %, a 128-point Hamming window equivalent in time to 0.03 seconds with a 80 % overlap, and a 128-point Hamming window equivalent in time to 0.03 seconds with a 98 % overlap. The evaluated parameters are the number of embolic detections recorded on the spectrogram and the energy of the detected embolus relative to the energy at the peak systole. The best results are obtaining by a 0.015 seconds Hamming window and a 65 % overlap.	42
4.1	Results (Detection Rate and False Alarm Rate) for 2 sub-band decomposition with a 4 dB constant empirical threshold used in each sub-band.	72
4.2	Results (Detection Rate and False Alarm Rate) for 4 sub-band decomposition with a 4 dB constant empirical threshold used in each sub-band.	73
4.3	Results (Detection Rate and False Alarm Rate) for 8 sub-band decomposition with a 3 dB constant empirical threshold used in each sub-band.	73
4.4	Results (Detection Rate and False Alarm Rate) for 2 sub-band decomposition with a $\lambda = \mu + 5\sigma$ constant statistical threshold used in each sub-band.	74
4.5	Results (Detection Rate and False Alarm Rate) for 4 sub-band decomposition with a $\lambda = \mu + 4.5\sigma$ constant statistical threshold used in each sub-band.	74
4.6	Results (Detection Rate and False Alarm Rate) for 8 sub-band decomposition with a $\lambda = \mu + 4\sigma$ constant statistical threshold used in each sub-band.	75
4.7	Results (Detection Rate and False Alarm Rate) for 2 sub-band decomposition with a $\lambda(t) = \mu(t) + 6\sigma(t)$ time-varying threshold used in each sub-band.	76
4.8	Results (Detection Rate and False Alarm Rate) for 4 sub-band decomposition with $\lambda(t) = \mu(t) + 5.5\sigma(t)$ time-varying threshold used in each sub-band.	76
4.9	Results (Detection Rate and False Alarm Rate) for 8 sub-band decomposition with a $\lambda(t) = \mu(t) + 3\sigma(t)$ time-varying threshold used in each sub-band.	77
4.10	Results (Detection Rate and False Alarm Rate) for 4 sub-band wavelet packet decomposition with a 6 dB constant empirical threshold used in each sub-band.	88
4.11	Results (Detection Rate and False Alarm Rate) for 4 sub-band wavelet packet decomposition with a $\lambda = \mu + 5\sigma$ constant statistical threshold used in each sub-band.	89

4.12	Results (Detection Rate and False Alarm Rate) for 4 sub-band wavelet packet decomposition with $\lambda(t) = \mu(t) + 6\sigma(t)$ time-varying threshold used in each sub-band.	89
5.1	Training phase results of the optimal thresholds that best maximize the detection rate and minimize the false alarm rate for the skewness and kurtosis based detectors.	97
1	The calculated diameters for the smallest detected micro-emboli	129

List of Acronyms

CVA CerebroVascular Accident

CWT Continuous Wavelet Transform

DWT Discrete Wavelet Transform

EBR Embolus to Blood Ratio

ECG Electrocardiogram

FrFT Fractional Fourier Transform

HIV Human Immunodeficiency Virus

HITS High Intensity Transient Signals

HOS High Order Statistics

IE Instantaneous Energy

RBC Red Blood Cells

RII Relative Intensity Increase

STFT Short Time Fourier Transform

TIA Transient Ischemic attack

WBC White Blood Cells

WFT Windowed Fourier Transform

WT Wavelet Transform

WPD Wavelet Packet Decomposition

General Introduction

Motivation

More than twenty years ago, monitoring cerebrovascular pathologies has aroused as a great interest in the medical society. In particular, monitoring of patients with embolic complications has become an ongoing permanent preoccupation in various hospital and clinical settings, mainly because the presence of cerebral emboli is responsible for various cerebrovascular accidents (strokes). Cerebral emboli could be one of many substances foreign to the bloodstream, such as an inappropriately formed blood clot, an aggregation of red blood cells, gas bubble, etc. which is able to block cerebral blood vessels or vessels supplying the brain with blood.

While the presence of large cerebral emboli leads to immediate stroke, the presence of small migrating micro-emboli is a precursor of the coming large embolus with high stroke effects. Therefore, detection of these small micro-emboli has gained a worldwide importance, particularly due to the advances of transcranial Doppler ultrasound conducted during the last 20 years. Early micro-embolic detection is believed to reduce stroke risks and help increase patient safety (Ringelstein et al., 1998).

Many research activities have been lead in perspective of finding methods of detecting micro-emboli through the transcranial Doppler (TCD) signal. Although remarkable achievements have been made, several hindering points remain. First, the TCD systems of measurement still pose various limitations including the considerably long time needed for probe positioning, the decreased confidence in automatic detection and the very short effective examination duration, not sufficient to allow the detection of several asymptomatic micro-embolisms. Second, the algorithms implemented in the TCD systems, although are very well adapted for the detection of large emboli, they do not allow the correct and robust detection of the small weak micro-emboli.

This Ph.D. deals with the problems of detecting weak micro-emboli and presents different offline signal processing algorithms for robustly detecting them from Doppler signals obtained using a new TCD system which overcomes the limitations of traditional TCDs.

Organization of the Manuscript

This dissertation presents both theoretical and numerical investigations of embolus and micro-embolus detection. It is divided into three major parts as follows:

- **Part I:** This part introduces basic conceptions concerning cerebrovascular accidents, cerebral embolism and the micro-embolus detection process. A brief introduction is provided including an overview of the background (chapter 1), and the instrument of detection used as well as the different detection considerations (chapter 2). Chapter 2 also introduces the standard methods of detection.
- **Part II:** This part contains the different proposed methods of embolus detection. In chapter 3 we present a new detection method based on energy fluctuations. The main idea is to remove the cardiac rhythm trend from the Doppler energy and obtain energy fluctuations where the micro-embolus can be detected from the positive energy fluctuations.

After proving that micro-embolic signatures occur only in the positive fluctuations, an instantaneous time-varying threshold is constructed from the negative fluctuations. This threshold, would next be applied on the positive energy fluctuations. Micro-embolic signals, in the positive fluctuations, would appear as signatures exceeding this threshold. In chapter 4 detection based on sub-band decomposition is introduced. The whole Doppler spectral band is decomposed into several bands. Through this decomposition, the bandwidth in which detection is applied is reduced. This in turn allows reducing the background red blood cells in the inspected bandwidth. Consequently, decomposing the whole Doppler frequency band will amplify the contrast between the micro-embolic signature and the background signal in each decomposed channel. The detectability of the micro-embolus signature in the background signal is increased. In chapter 5 detection based on high order statistics is presented. Knowing that the occurrence of a microembolus superimposed on the Doppler energy signal imposes changes in the distribution of this signal, we propose to use the skewness and kurtosis as new tools for micro-embolus detection. During embolus-free periods, the Doppler energy signals distribution is fixed and its skewness and kurtosis are never altered. They do not show any variations. However, in the presence of a microembolus superimposed on the energy signal, the skewness and kurtosis signals are altered and the embolus is attributed with a peak whose peakedness level is higher than all the other points of the signal. Chapter 6 deals with the different artefact rejection techniques. Artefacts are divided into unidirectional ones and other bidirectional. Both types are canceled from the energy signal verifying that the latter signal is artefact-free before application of detection techniques. Finally, chapter 7 provides a general summary of all techniques, as well as the conclusion and perspectives in order to sum up the whole dissertation and open the space for further contributions and works.

Main Contributions

- **Chapter 3:** The contribution of this chapter is proposing an innovative idea of applying the micro-embolus detection process on the energy signal fluctuations. The originality comes out when compared to standard techniques where detection is always performed on the energy signal. Moreover, the negative energy fluctuations were proven to be embolus-free and a time varying threshold was constructed from these fluctuations. Therefore, the detection was based on time varying thresholds rather than traditionally using constant thresholds.
- **Chapter 4:** In this chapter, the contribution is proposing an authentic approach based on the joint use of several separate hypotheses that were considered alone up till now. Whole band detection is replaced by sub-band detection either through decomposing the short time Fourier transform spectrum into equally spaced frequency sub-bands or through wavelet packet decomposition. Furthermore, this sub-band detection was coupled with constant thresholds of detection and innovatively with the time-varying threshold constructed in chapter 3.
- **Chapter 5:** To our best knowledge, we have presented in this chapter the first signal processing micro-embolus detection system based on high order statistics.

- **Chapter 6:** In this chapter we have proposed signal processing algorithms for artefact rejection. This alone is indeed a noticeable point since in many detection systems artefact rejection is never taken into consideration. We have also dealt with both types of artefact, bidirectional and unidirectional artefacts where the latter were in many previous studies considered as non-existing.

List of Publications

International Journal papers

- Maroun Geryes, Sebastien Ménigot, Walid Hassan, Ali Mcheick, Jamal Charara, and Jean-Marc Girault, *Detection of Doppler Micro-Embolic Signals using High Order Statistics*, Computational and Mathematical Methods in Medicine
- Sebastien Ménigot, Maroun Geryes, Ali Mcheick and Jean-Marc Girault, *Microemboli Detection through Synchronous Spectrogram*, Submitted to Computational and Mathematical Methods in Medicine, Manuscript number: 4367985, Submission Date: 20/07/2016
- Maroun Geryes, Sebastien Ménigot, Ali Mcheick, Mohammad Nasserline, Jamal Charara and Jean-Marc Girault, *Enhanced weak Doppler Micro-Embolic Signal Detection using Energy Fluctuations*, Submitted to IEEE Journal of Biomedical and Health Informatics, Submission Date: 09/12/2016

Conference papers

- Maroun Geryes, Sebastien Ménigot, Walid Hassan, Marilys Almar, Benoit Guibert, Corinne Gautier, Jamal Charara and Jean-Marc Girault, *A New Energy Detector of Micro-Emboli Using A Time-Varying Threshold*, The Third International Conference on Advances in Biomedical Engineering (ICABME 2015), Beirut, Lebanon, September 16-18, 2015
- Maroun Geryes, Sebastien Ménigot, Walid Hassan, Ali Mcheick, Marilys Almar, Benoit Guibert, Corinne Gautier, Jamal Charara and Jean-Marc Girault, *A Micro-Embolic Energy Detector based on Subband Decomposition*, The Third Middle East Conference on Biomedical Engineering (MECBME 2016), Beirut, Lebanon, October 6-7, 2016

Part I

Basic Conceptions

Chapter 1

The study of embolism

1.1 Introduction

In 1982, Rune Aaslid introduced the Transcranial Doppler ultrasound technique (Aaslid et al., 1982). The technique has since found huge acceptance as an indispensable tool for the evaluation of cerebral hemodynamics in a wide variety of clinical settings.

In 1987 and later in 1990, Padayachee et al. (1987) and Spencer et al. (1990) reported an innovative use of the Transcranial Doppler. In their work, Padayachee and Spencer described the application of TCD for the detection of middle cerebral artery emboli during cardiopulmonary bypass and carotid endarterectomy, respectively. Consequent investigations of this new approach proved the ability of TCD in accurately detecting emboli and threw the doors wide open for numerous researches and studies on the embolus.

Early studies on the embolus were dedicated to monitor the embolus and estimate its interactions with the Transcranial Doppler waves. As embolus monitoring proved to have a potential role for the identification of patients with an increased stroke risk, the detection of embolus became the major concern and it has superseded all other studies that were introduced to explore the embolus' physical nature, characterize them, estimate their size, etc.

The methodology for detection of embolus has made considerable progress over the past twenty years. One of the earliest works were those of Hennerici (1994). Other significant studies were those proposed in Moehring et al. (1995), Aydin and Markus (1999), Cullinane et al. (2000), Girault et al. (2000), Fan et al. (2001a), Evans (2003), Aydin et al. (2004), Markus et al. (2010), and Serbes et al. (2014).

In the sections to come, we will give a complete description of embolic strokes and the embolus. We will also introduce the problematic and objectives of this dissertation.

1.2 CerebroVascular Accidents and the Embolus

A CerebroVascular Accident (CVA), also known by the medical term of stroke, occurs when blood supply to the brain or part of it is reduced or interrupted in any manner. This deprives the brain of oxygen and nutrients which leads to the damage or death of the brain cells deprived of oxygen and nourishment. Death of these cells, and thus the brain, will in turn lead to dysfunc-

tion of the brain tissues and then loss of body functions controlled by the brain or the affected part of the brain.

Stroke is a medical emergency, which needs immediate medical attention and an untreated stroke for long-enough, will cause permanent brain damage and death. Strokes are the second cause of mortality and morbidity worldwide after Cancer [(Organization, 2000) up till (WHO, 2010) and (WHO, 2014)]. Some stroke facts include:

- Stroke are responsible for almost 130,000 deaths per year in the United States that's one out of every 20 deaths, 32,000 in France and 2199 in Lebanon, that's 10 % of all deaths.
- Every year more than 795,000 people in the United States and more than 100,000 people in France have a stroke.

Strokes are considered of two categories, either those caused by a breakage or bursting of a blood vessel known as hemorrhagic strokes or those caused by blockage of a cerebral artery known as ischemic strokes. In a hemorrhagic stroke (or cerebral hemorrhage) a torn or ruptured artery in the brain will cause blood to spill out. This in turn will lead to part of the brain being deprived of blood and oxygen. The cells of this brain part will die. Hemorrhagic strokes represent 20 % of all strokes and often result from high blood pressure and over-treatment with anticoagulants. Intracerebral and subarachnoid are the two types of hemorrhagic strokes. Around 80 % of strokes are ischemic. Ischemic strokes are those occurring when the arteries to the brain become narrowed or blocked, causing severe interruption in blood flow. Two types of ischemic strokes can be distinguished:

- Thrombotic stroke. Thrombotic stroke occurs when a blood clot known as a thrombus forms locally in one of the arteries that supply blood to the brain. Two types of thrombosis can cause stroke; thrombi forming in large vessels including the internal carotid artery, vertebral artery and Circle of Willis, and thrombi forming in small vessels including the smaller arteries inside the brain such as the middle cerebral artery, the branches of the Circle of Willis, etc.
- Embolic stroke. Embolic stroke occurs when one of the arteries supplying blood to the brain is blocked by an embolus.

Embolic strokes constitute up to 14 % of all strokes (Murtagh and Smalling, 2006). Embolic strokes are the result of cerebral embolism, an arterial embolism occurring in the brain. Cerebral embolism is the blockage of major blood flow in a cerebral artery.

Other types of embolism include air, pulmonary, arterial and venous embolisms, and thromboembolisms. In general, embolism is a blocking of a blood vessel by a material foreign to the bloodstream constituents. These materials or particles are the emboli (Patterson Jr et al., 1972). Emboli move away from the place where they are formed through the bloodstream to other parts of the body. During their movement through the blood vessels, the emboli are likely to come to a passage they cannot fit through. They lodge there, backing up and stopping the flow of blood behind them. Emboli can travel in veins, which carry blood deprived of oxygen back to the heart and lungs to get re-oxygenated, as well as arteries, which carry blood rich in oxygen from the heart to the various tissue cells in the body. Emboli can block large or medium sized arteries and veins as well as small sections or branches of arteries and veins. The embolus could be one

1.2. CEREBROVASCULAR ACCIDENTS AND THE EMBOLUS

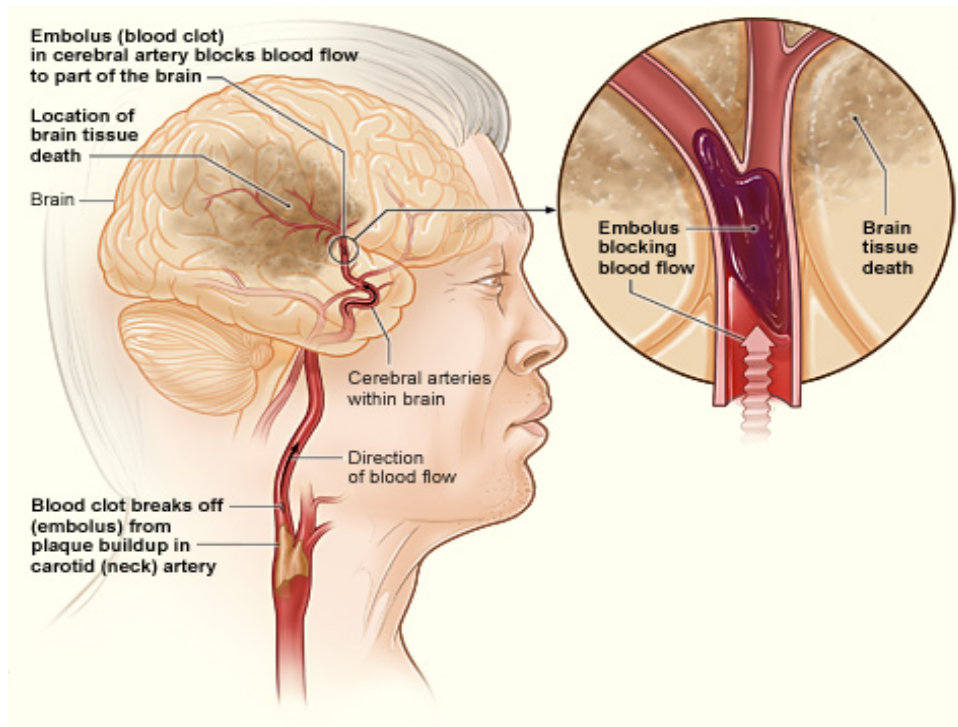


Figure 1.1: An illustration of an embolus in the carotid arteries blocking blood flow to a part of the brain and thus causing damage to brain tissues (National Heart, Lung and Blood Institute).

of many substances foreign to the bloodstream and traveling within it, including aggregation of red blood cells, blood clot formed inappropriately by platelets and fibrin in the blood, gas bubble, fat globule or bone marrow globule, cholesterol crystals, atheromatous plaque or any other strange body carried by blood flow. The most common cause of embolus formation is the malfunctioning of the heart including conditions as atrial fibrillation, atrial flutter, mitral valve disease and cardiac tumors. Blood abnormalities, developed before birth or acquired from certain diseases and medications, are also a frequent cause of embolus formation. Immobilization is also an important factor in embolus formation. Insufficient mobility puts a strain on the circulatory system and the circulation of blood, and long inactivity increases the risk for blood clot formation. In addition, emboli are very frequently seen during and after surgical operations such as cardiac surgeries carotid artery dissection, and carotid endarterectomy. Gaseous emboli are also formed in patients with mechanical artificial heart valves. Other less common causes include Human Immunodeficiency Virus (HIV), trauma to the legs, severe aortic arch atheromateous changes, obesity, pregnancy and some types of cancer.

Turning back to cerebral embolism, a large percentage of these embolisms happen due to emboli traveling through the carotid arteries or even building up in them. The carotid artery is the artery responsible for supplying the brain with oxygen-rich blood. Its pulse can be felt on both sides of the neck directly under the jaw. Embolism in the carotid arteries hugely limits blood passage to the brain arteries and can even totally block the carotid arteries thus suppressing all blood flow. The presence of emboli in carotid arteries were verified many years ago such as by Siebler et al. (1993), Markus et al. (1995) and van Zuilen et al. (1995). A demonstration of an embolus passing through the carotid arteries thus limiting blood flow and causing damage to a part of the brain cells is shown in Figure 1.1.

1.3 Statement of the problem and objectives

CVA is a life-threatening condition. Taking into consideration that cerebral embolism presents a serious risk leading to CVAs, the diagnosis of cerebral embolism becomes a must and a worldwide health and safety concern.¹

Practically, diagnosing embolism involves three main phases: detection and counting of emboli, describing embolus composition and estimating embolus size. Ideally, researchers in the embolus domain would like to be able to detect all emboli and to characterize their size and composition (particularly solid or gaseous). While considerable progress has been achieved in understanding the physical and clinical nature of emboli, even the superficially simple task of detecting emboli still poses great challenges. Also, the detection and counting of emboli remains the fundamental step after which all applications would take place. Logically, characterization of emboli and estimating their size would never be possible without detecting the embolus first.

Up till now, numerous research works and projects have been lead in perspective of detecting emboli in the most accurate and robust manner. The detection has passed by several ups and downs. Some methods proved to be suitable for embolus detection in certain conditions, others were accepted to be suitable in various circumstances and others were accepted and then proven to be inefficient or even wrong.

Indeed, while embolus detection has reached a highly acceptable level of performance and a sufficient level of understanding among the scientific and medical societies a critical point remains debatable! It concerns the detection of small weak micro-emboli which up till now has not been completely sorted out.

In fact, micro-emboli cannot stop the blood flow in the main arteries of an organ but can hinder micro-flow around these arteries which could later lead to the same complications caused by large emboli. Indeed, physicians and clinicians worldwide are now firmly convinced that the detection of small micro-emboli is a precursor of the coming large embolus with hazardous stroke risks and that the migration of small micro-emboli heralds the arrival of the bigger dangerous emboli.

Therefore, the detection of small micro-emboli would equip the medical and clinical team with an important instrument for selecting patients who could undergo therapy. It would provide better treatment plans, more effective targeting of therapy and patient management and follow up. Thus as a result early detection of micro-emboli would allow avoiding the occurrence of CVAs and reducing the risk on patients.

However the detection of small micro-emboli remains a very common hindering drawback in many research works based for embolus detection. Moehring and Klepper (1994) introduced one of the earliest fundamental concepts concerning the Doppler ultrasound signals backscattered by emboli flowing in the blood and established several parameters for the detection of emboli. Four years later, the consensus on micro-embolus detection by TCD took place (Ringelstein et al., 1998), during which the technical background and physics of embolus detection were clearly defined. In both of these studies the particular characteristics of weak micro-emboli was not discussed. A considerable improvement in the detection of weak

¹We should note that in the sections to follow, we will be using the term embolus alone rather than cerebral embolus for simplicity while keeping in mind that the whole dissertation concerns cerebral embolism.

micro-embolic signals was achieved by Markus et al. (1999) and Markus and Reid (1999). As the micro-embolic event is of narrow band nature, Markus et al. (1999) and Markus and Reid (1999) proposed to detect this event by using a band pass filter encompassing the spectral signature of the micro-embolic event. By using such a band pass filter on the energy or power, the intensity of the micro-embolic event increased thus improving the detection capability of the detector. However the price to pay was that the frequency of the micro-embolic signal had to be known before the filtering step in an automated detection paradigm. This was rarely possible. Moreover, when applied online by Cullinane et al. (2000) and Cullinane et al. (2002), respectively the latter frequency filtering methods showed poor performance in the detection of low energy micro-embolic signals although great performances in terms of sensitivity and specificity were obtained for high embolic signals. Another achievement in the detection of micro-emboli was proposed by Girault et al. (2000). Methods based on detection of sudden changes were introduced. Non-parametric detection methods mainly the Fourier, Wigner Ville and wavelet approaches were compared to parametric auto-regressive methods. The new parametric methods were proven to be highly performant and efficient in the detection of small micro-emboli. However, the methods were tested on synthetic simulated Doppler signals. The offline detection presented by Fan et al. (2001b) had excellent detection results for emboli having intensities higher than the background blood flow. However, the detection of weak embolic signals below the background level was never taken into consideration. The same can be said for the online detection proposed by Marvasti et al. (2004) where the detection rates for low energy micro-embolic signals were arguably inadequate. A study based on the discrete wavelet transform (DWT) was introduced by Aydin et al. (2004). In this study the authors analysed some threshold-based parameters useful for describing and detecting micro-embolic signals. The DWT increased detection system sensitivity and specificity specially for the detection of small micro-emboli. Nonetheless, a major deficiency of the DWT-based technique was the reduced frequency resolution at low frequency scales, in which micro-embolic signals are mostly found. Chung et al. (2005) investigated the effect of the choice of the decibel threshold on the detection of embolic and micro-embolic signals. A threshold providing reliable detection of micro-emboli should be as low as 2 dB. Two robust micro-embolic detectors were established in Girault et al. (2010) and Girault and Zhao (2014). In the first a new detector based on conditional variance (GARCH model) was introduced. The detector outperformed conventional energy detectors in detecting weak micro-emboli. However, this technique depended on only one statistical tool which was the false alarm rate and did not take into account the detection rates correlated with the achieved false alarm rates, and also it was tested on few micro-embolic signals. In the second study Girault and Zhao (2014), an original synchronous detector, synchronized with the cardiac cycle, was introduced. It uses the pseudo-cyclostationarity properties of the blood Doppler signal. Compared to standard energy detectors, the synchronous detector improved the detection rate of weak micro-emboli. However, the difficulty related to this technique was that it might sometimes fail for certain patients with high cardiac rhythm variations. The study done by Gençer et al. (2013) applied embolic detection via Fractional Fourier Transform. The results showed that discriminating features generated by Fractional Fourier Transform help easier analysis and detection of embolic signals. Despite of its simplicity, this method was not proven as reliable for the detection of the smallest micro-emboli. Several experimental methods were put into application, such as in (Markus et al., 2010), (Silbert et al., 2014) and (Piorkowski et al., 2015). They revealed interesting results but were not coupled with processing techniques in order to prove the reliability of the micro-embolic

detection systems applied.

On another hand, commercially used detection systems have been based on automatic short time Fourier transform techniques employing constant thresholds of detection, which we will discuss later in the next chapter. Such detectors' performance in the detection of low intensity micro-emboli is hugely unsatisfactory, although they perform well for relatively large emboli. Truly, in many cases, the clinicians detect, in an audible or visual manner, the passage of micro-emboli in the blood sample volume while the system detector remains mute and detects nothing. The inability of these detectors to detect smallest micro-emboli have raised numerous questions on using this kind of systems in clinical routine.

Therefore, the ultimate objective of this dissertation is the implementation of a new signal processing micro-embolus detection system that could detect the smallest possible micro-emboli² in a robust manner. The dissertation, alongside newly proposed methods, contains an implementation of the standard detection methods that are present in most of the commercially-used detection systems.

1.4 Conclusion

In this chapter, we have given a detailed description of CVAs and cerebral embolism. In this context, we shed light on the importance of detecting cerebral emboli, specially small micro-emboli, as a preventive step to reduce the risk of CVAs. We also provided the problematic of our work as well as the objectives we aim to complete.

In the upcoming chapter, we will invade the technical background behind micro-embolus detection.

²The minimum size below which an embolus would be considered as a small micro-emboli does not have a worldwide employed definition. Based on information from the literature background (Moehring et al., 1995), (Russell, 1995), (Evans, 2003), (Martin et al., 2009) and on calculations we have done and presented in appendix A of this dissertation, a solid micro-emboli would have a diameter below 100 μm .

Chapter 2

The Detection of Embolism

2.1 Introduction

Sudden intensity increases occurring in the Transcranial Doppler (TCD) signal are interpreted as cerebral micro-embolic signals. Practically, these increases can be described as sudden 'chirps', or 'moans' (Ackerstaff et al., 1995). Strong evidence has been given that these intensity increases are produced by small embolic particles passing through the blood sample volume.

The Transcranial Doppler is now the most used system for detecting cerebral emboli. When detecting embolic signatures, various technical factors must be considered in terms of adjusting TCD settings and signal analysis. The basic principle of the TCD technique is that when an embolus is radiated by an ultrasound it backscatters more power than the volume of the blood it occupies. Therefore, careful monitoring of the Doppler signal power backscattered by the blood constituents and occupants present in the sample volume provides a strong mean of detection.

Although the characteristics of embolic signals in the TCD signal have been well defined, the task of detecting embolic and specifically weak micro-embolic signals still poses a challenge. Numerous worldwide used commercial TCD systems possess many restrictions for the accurate detection of embolic signals in different conditions. Therefore, new systems are being introduced nowadays compensating for many disadvantages of standard TCDs. These systems pave the way for complex detection methods to be proposed. A system that has been recently developed and implemented in this dissertation work is the Holter system by Atys Medical, France.

Another challenging issue before a complete accurate detection, is the differentiation of true embolic signals from similar artefact signals appearing in the TCD signal and which may negatively mislead the detection system. Therefore, artefact rejection is a decisive step in any detection technique.

In the next sections, we will be discussing the TCD ultrasound system and we will introduce the new TCD Holter system. Moreover, we discuss the TCD detection of embolic signals and we introduce the relative intensity increase of micro-embolic signals, a main parameter in micro-embolus detection. We also present the pre-settings used in the different implementations of this dissertation. This chapter also includes a detailed description of the implementation of the standard detection methods.

2.2 The Transcranial Doppler ultrasound system

First introduced in 1982 by Aaslid et al. (1982), the TCD is the leading system in the detection of embolic signals. The TCD measures the velocity of blood flow in the brain's blood vessels and also the relative changes in the flow. Transcranial Doppler diagnoses are based on the detection of altered blood flow velocity, absence of blood flow, or changes in the spectral waveform. The Doppler effect forms a basis in the TCD system. The TCD has been the most commonly used system. It is non-invasive, non-ionizing, easy to use, inexpensive, portable and safe technique, which renders it as a convenient equipment for detection of circulating emboli.

The TCD is a pulsed wave Doppler system, where a single transducer alternates wave transmission and reception¹. A train of ultrasound pulses of duration T and frequency f_0 usually between 2 and 4 MHz is emitted towards the sample volume which is operator-controlled. The ultrasound pulses propagate through the tissues and blood for a time d_0 until it is backscattered by the the different moving particles and returns back to the transducer over the same time interval d_0 but with a time shift τ (due to the movement of the particles) at a shifted frequency $f_0 + f_d$, where f_d is the Doppler frequency given as:

$$f_d = 2f_0 \frac{v \cos \theta}{c} \quad (2.1)$$

where c is the speed of sound, and v is the speed of the moving particle in the directions θ and relative to the propagation of the ultrasound wave.

The total transit time to and from the sample volume is $2d_0$. This process is alternately repeated through many transmit-receive cycles each second. The signal received at the transducer is demodulated. It is multiplied by the carrier frequency before being low-pass filtered to eliminate the high frequency components and high-pass filtered to eliminate the effect of the movement of the vessel walls.

2.3 The Holter TCD system

The TCD system used in this study is the Transcranial Holter manufactured by a French firm, ATYS MEDICAL, in Soucieu en Jarrest, France. The Holter is shown in Figure 2.1.

¹Specific TCD considerations:

Basically, the TCD technique consists of insonating the basal portions of the cerebral arteries through different 'windows' found at different locations in the skull. Since the bones of the skull block the transmission of ultrasound, an important step is to localize a cranial 'window' for the ultrasound beam to penetrate without getting excessively dampened. There are three main windows for accessing the intracranial arteries:

- The Transcranial or Transtemporal window located between the angle of the eye and the pinna of the ear. This window is the main route for insonating the middle, anterior and posterior cerebral arteries and the terminal internal carotid artery.
- The Transorbital window allows insonating, through the eye, the ophthalmic artery and the siphon of the internal carotid artery.
- Transforaminal or Sub-Occipital window found between the atlas and the base of the skull and allows the insonation of the basilar artery and the intracranial segment of the vertebral arteries.

2.3. THE HOLTER TCD SYSTEM

The Holter version holds solutions to traditional TCD limitations. The proposed solutions involve new enhancements such as the automatic positioning of the ultrasonic probe and the possibility of long-term recordings with the micro-emboli detection process being performed offline through a computer. In fact the various advantages include:

- Allows prolonged patient monitoring (higher than 5 hours) and thus offers more legitimacy for micro-embolus detection.
- Equipped with a robotized probe.
- The patient is no longer attached to a TCD and does not need to be laying on a bed, but rather can be monitored under naturalistic conditions and can even move, talk, etc. thanks to the lightweight and comfortable probe.
- The automatic probe helps find the best TCD signal and tracks it automatically during the whole recording.
- An auto-search algorithm restores vessel insonation should the signal quality fall.



Figure 2.1: Holter Transcranial Doppler System (TCD-X, Atys Medical, Soucieu en Jarrest, France)

It has been pointed out that the Holter generation allows offline embolus detection. The offline detection refers to the fact that the detection is not performed directly on the patients. Unlike online detection where the patients are monitored and the signals are directly saved and analyzed, in offline detection procedure a large set of recordings (a database) is collected from different patients and then the detection is performed on a separate machine. This offline detection allows developing more complex systems of detection. However, this offline detection is applicable under preferable circumstances that the micro-embolus is asymptomatic. Indeed, two types of carotid artery stenosis patients can be discriminated; those with symptomatic emboli and those with asymptomatic emboli. In the case of symptomatic emboli, emboli

detection provides the necessary information required to make a clinical decision. For symptomatic patients with severe carotid artery embolism, the best treatment is operation. In the case of asymptomatic patients or patients with lesser degrees of carotid artery embolism, the asymptomatic emboli are markers of increased stroke risk. The asymptomatic micro-embolus makes the offline detection possible while in turn the offline detection allows follow up of these asymptomatic micro-emboli. Therefore, the possibility of long term recordings by the Holter is important since the prevalence of asymptomatic micro-emboli is relatively low and thus detecting their signatures requires a sufficiently long examination duration.

2.4 Micro-embolus detection by TCD

Embolus signatures are detected in the TCD as High Intensity Transient Signals (HITS) superimposed on the blood Doppler signal. They are characterized in the TCD by several aspects [(Ackerstaff et al., 1995), (Spencer, 1992), (Georgiadis et al., 1994), (Evans et al., 1997), (Ringelstein et al., 1998)] as follows:

- Their amplitude exceeds the background blood signal by at least 3 dB although micro-embolic signals could have amplitudes largely below 3 dB. This means that the amplitude of micro-emboli is less than 3 dB.
- The embolic signal duration lasts less than 300 ms.
- They are unidirectional within the Doppler velocity spectrum.
- They occur randomly in the cardiac cycle.
- They produce a sound like a 'moan' or 'chirp' on the audio signal.

2.5 The micro-embolus intensity increase relative to the moving blood

A very important indicator in the detection and characterization of emboli stated in the previous section, is the relative intensity increase of the embolus which defines the relationship between the backscattered power from emboli and that from the blood. It indicates how strong an embolic signal is, relative to the background Doppler signal. It is calculated as the ratio of the energy backscattered from the embolus to that of the moving blood surrounding it.

The first definition of the embolus relative intensity increase was given by Moehring and Klepper (1994) and Moehring et al. (1995) as the Embolus to Blood Ratio (EBR). Since then, the EBR has been extensively used to assess embolus detectability. Later, during the meeting of the international consensus group on microembolus Detection (Ringelstein et al., 1998), the embolus relative intensity increase was set as a basic parameter affecting the detection of micro-embolic signals.

The amount of blood in the Doppler sample volume, the velocity of the traveling embolus, as well as its size and composition all affect its relative intensity increase. The embolus relative

2.5. THE MICRO-EMBOLUS INTENSITY INCREASE RELATIVE TO THE MOVING BLOOD

intensity increase (RII) can be measured in different ways. A very common way of measurement is given by the following equation:

$$RII = 10 \log_{10} \left(\frac{P_{E+B}}{P_B} \right). \quad (2.2)$$

P_{E+B} is the backscattered power or energy measured when an embolus and the blood are present in the Doppler sample volume. P_B is the backscattered power or energy measured from blood alone in the sample volume (embolus-free periods). The measured quantity is in decibels (dB).

It is important to realize that different settings can be used to measure the relative intensity increase of an embolus. Mainly, these settings are related to the manner of defining and estimating the background Doppler signal with which the embolus is compared. For instance, the background signal can be measured by the mean value over variable time periods and frequency ranges [(Droste and Ringelstein, 1998) and (Mess and Hennerici, 2001)]. It can be also calculated as the intensity at the location similar to that of the detected embolus in the preceding cardiac cycle or the mean intensity through a defined number of embolus-free frames. The background could also be simply estimated as the mean of the power or energy of the part of the signal without embolus [(Darbellay et al., 2004)].

For this reason, when calculating the embolus relative intensity increase, the definitions of the embolus intensity and the background intensity estimation should be clearly stated and the different specifications should be reported before the results are given. In our study, the backscattered energy in the presence of an embolus is calculated as the peak energy of the embolus detected in the Doppler signal [(Droste and Ringelstein, 1998), (Ringelstein et al., 1998), (Mess and Hennerici, 2001), and (Darbellay et al., 2004)]. As for the background signal intensity measurement, we choose to estimate it using the trend of the Doppler signal. This trend, representing the blood flow signal, is considered to be embolus-free. In order to estimate the trend of the Doppler signal we calculated a smoothed version representing the low frequency component of the Doppler signal related to the cardiac rhythm (of 1 Hz). This smooth curve can be depicted in Figure 2.2.

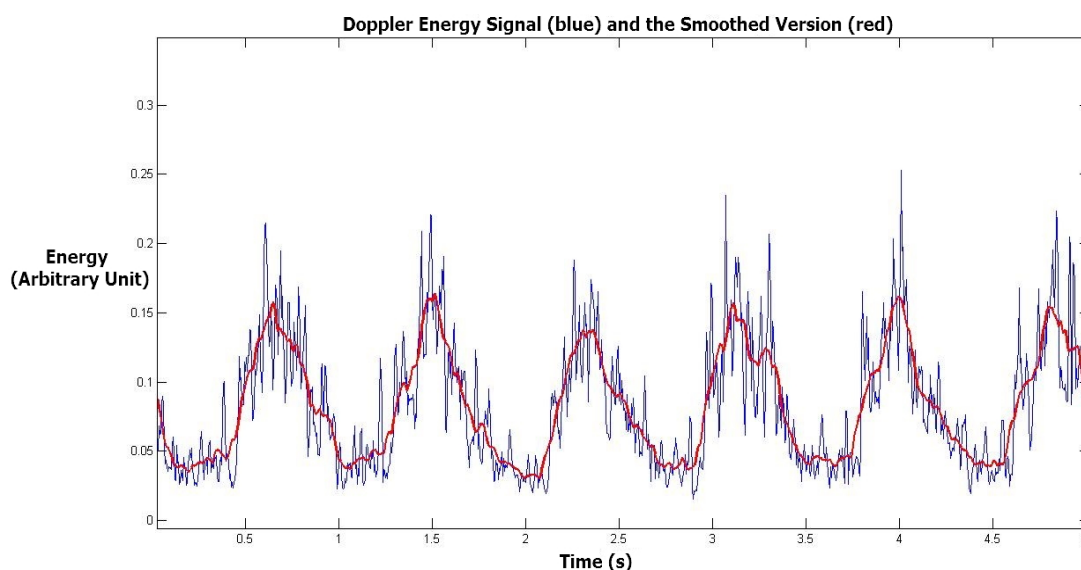


Figure 2.2: The background Doppler signal is estimated to be the trend represented by the smoothed version (in red) of the Doppler signal (in blue).

2.6 The Reference Off-line standard detection signal processing unit

The different implementations we will be proposing in this dissertation are based on 25 clinical recordings. The recordings were carried out at the 'Centre Hospitalier Régional Universitaire' (CHRU) de Lille (2 Avenue Oscar Lambret, 59000 Lille, France). Written informed consent was obtained from all patients before their enrollment in the monitoring process. The written consent forms were investigated and approved by the Hospital of Lille.

By means of a transducer, an ultrasonic wave with a frequency of 1.5 MHz is transmitted to the middle cerebral artery of patients with asymptomatic carotid stenosis. A pulse repetition frequency (PRF) of 6.4 kHz is used with an ultrasound power of 50 mW/cm^{-2} .

During post-treatment, the TCD recordings were converted into audio-wave files (quantification over 16 bits and sampling frequency of 4 kHz). These recordings are then analyzed and treated with our algorithms which are developed using the numerical calculation software Matlab (Mathworks, Natick, MA, USA).

From a signal processing detection point of view, the most common commercial automatic micro-embolic detection systems are based on the energy calculated from the classical short time Fourier transform. Constant thresholds, fixed empirically by the user, are widely used. We will introduce this standard detection. Alongside, we will also propose a statistical constant threshold.

The typical standard off-line signal processing unit is decomposed into 4 units as shown in Figure 2.3:

- Unit A, allocated for loading the wave file, 5 second signal segmentation, Short Time Fourier Transform (STFT) calculation and instantaneous energy calculation from the

STFT;

- Unit B, allocated for establishing the audible and visual Gold standard of detection;
- Unit C, allocated for artefact rejection;
- Unit D, allocated for standard energy detection using constant thresholds of detection;

2.6.1 Unit A: Doppler signal extraction, STFT and instantaneous energy calculation

The different systems that we want to test, depicted in Figure 2.3, share a common structure. From the SD card plugged out from the Holter system and plugged into the personal computer, the Doppler signal is picked up and put in memory. From this Doppler digital signal, the STFT is calculated, first to display the spectrogram and second to estimate instantaneously the Doppler energy. Calculations of the STFT and the instantaneous energy are carried out repetitively on 5 second segments extracted from the Doppler signal. This value is fixed to 5 seconds because it corresponds to the time duration on the spectrogram plotted on commercial devices. It allows a good visualization of different events that may occur.

The most familiar of methods employed by commercial TCD ultrasound systems are based on the STFT. The STFT is an adapted form of the Fourier transform that analyzes only a small segment of the signal at a time; a technique called windowing of the signal or also Windowed Fourier Transform (WFT). Transforming data into the frequency domain results in loss of time information. By applying the Fourier transform of a signal, it is impossible to identify when a particular event takes place. For stationary signals this drawback is not important. However, Doppler signals contain numerous non-stationary characteristics specially when an embolic signature characterized by an abrupt change is present. Fourier analysis is not suited to detect these characteristics. The STFT was thus proposed to correct this deficiency. The STFT maps a signal into a two-dimensional function of time and frequency. This representation is known as the spectrogram. A spectrogram is shown in Figure 2.4.

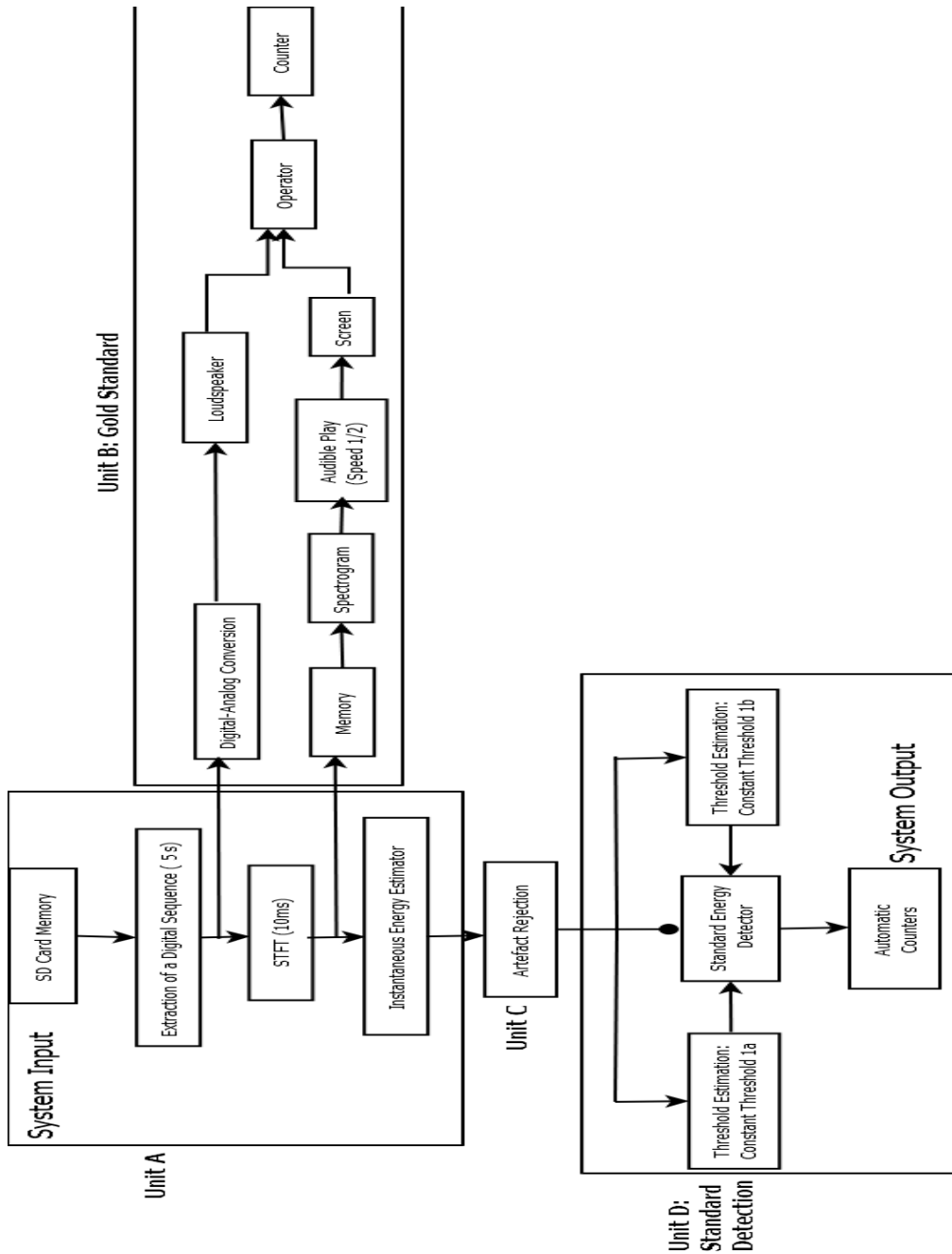


Figure 2.3: A typical embolus detection system including standard detection with constant thresholds. Unit A includes extracting 5s digital Doppler signal sequences from the SD card extracted from the Holter system, then calculating the STFT and the instantaneous energy from STFT estimators. Unit B includes establishing the gold standard of detection. Unit C includes the artefact rejection phase. Unit D represents the detection achieved using standard methods.

2.6. THE REFERENCE OFF-LINE STANDARD DETECTION SIGNAL PROCESSING UNIT

The STFT frequency estimator with a sliding window can be written as:

$$S(t, f) = \left| \int x(\tau) w^*(t - \tau) \exp^{-j2\pi f t} d\tau \right|^2 \quad (2.3)$$

where $x(t)$ is the analyzed Doppler signal, $w(t)$ is a sliding window and $*$ stands for complex conjugation.

When using the STFT to process embolic signals, it is of great importance that the STFT parameters are optimized. The three processing parameters are:

- Window size or length of the analysis window: the most influential parameter that determines the trade-off between frequency resolution and time resolution and has a direct effect on the time-frequency limitation.
- Window type: an important parameter in optimizing the frequency resolution and reducing spectral leakage.
- Overlap ratio: in the STFT technique the data segments are processed sequentially by sliding the window less than the size of the data segment. This leads to an overlap between the windows. Moreover, the windowing function applied is very liable to eliminating events at the edges of the data segment being processed. Therefore, a short embolic signal happening at the edges of the processed segment may be eliminated or missed. The solution is to adequately set the overlap ratio in a way to overcome the latter issue.

Despite the fact that setting the parameters significantly affects the embolus detection system based on STFT calculations, little work on the effect of the different parameters has been reported.

A fundamental study was reported by Aydin and Markus (2000). They evaluated the effect of varying the three parameters on embolic signal temporal and frequency resolutions, time of embolic signal onset and on the power of the embolus at the frequency with maximum power relative to the average power of the background intensity. The window types studied were the Boxcar, Bartlet, Hamming, Hanning, Blackman and Gaussian. The window sizes varied between 16-point and 512-point windows. The overlaps evaluated were 0 %, 25 %, 50 %, 75 %, 80 % and 98.4 %. The results reported that the best time and frequency resolution and the highest embolic power were achieved with a Hamming or Hanning windows. A medium sized window (64-point or 128-point) is the most appropriate, since a short window results in a good time resolution and a poor frequency resolution while a long window gives the best frequency resolution but poor time resolution. Moreover, the embolic signal power is low for windows shorter than 64 points, however it increases as the window size increases but only to a window size of 128 points and then decreases for higher windows. Finally, the most suitable overlaps were 65 % for a 64-point window and 80 % for a 128-point window, which prevents missing embolic signals occurring at the edges.

Based on the the study of Aydin and Markus (2000) and after a preliminary stage of experimental optimization of the STFT parameters, the STFT in this study is performed using a 64 point Hamming window equivalent in time to 0.015 seconds with an overlap of 65 %.

Three sets of parameters are tested, a 64-point Hamming window equivalent in time to 0.015 seconds with an overlap of 65 %, a 128-point Hamming window equivalent in time

to 0.03 seconds with a 80 % overlap, and another 128-point Hamming window with a 98 % overlap. Two measurements to evaluate the three sets are used. The first is the number of embolic detections recorded on the spectrogram based on what was stated by Aydin and Markus (2000) that an inadequate degree of optimal parameter setting may result in embolic signals being missed on the spectral display. Therefore we counted the number of embolic signals visually detected on the spectrogram as an indication for the best set of parameters. The second evaluation is a measure of the difference between the energy amplitude of the embolus and the energy amplitude of the corresponding peak systole as an indication of embolic signal power. If the difference is low this indicates that the embolus peak is closer to the systolic peak and this refers that the set of parameters to which this difference corresponds enables high embolic power. The results are obtained from 15 signals extracted from the 25 dataset signals. The results are presented in Table 2.1.

Table 2.1: A comparison between three sets of STFT parameters tested on 15 signals, a 64-point Hamming window equivalent in time to 0.015 seconds with an overlap of 65 %, a 128-point Hamming window equivalent in time to 0.03 seconds with a 80 % overlap, and a 128-point Hamming window equivalent in time to 0.03 seconds with a 98 % overlap. The evaluated parameters are the number of embolic detections recorded on the spectrogram and the energy of the detected embolus relative to the energy at the peak systole. The best results are obtaining by a 0.015 seconds Hamming window and a 65 % overlap.

Set of parameters tested	Number of embolic detections on the spectrogram	Mean embolus energy relative to peak systole energy (dB)
Hamming window, 0.015 seconds, 65 % overlap	86	5.8
Hamming window, 0.03 seconds, 80 % overlap	68	7.27
Hamming window, 0.03 seconds, 98 % overlap	72	6.56

Next comes the instantaneous energy calculation. Indeed, two kinds of energy estimators can be used to assess the instantaneous energy of Doppler signals: those based on time estimators and those based on spectral or frequency estimators. The two types are short-term estimators and the calculation is carried out using a sliding window $w(t)$.

The temporal energy estimator with a sliding window can be formally written as:

$$E(t) = \int |x(\tau)w^*(t - \tau)|^2 d\tau \quad (2.4)$$

However, in this chapter we focus on spectral estimators included in commercial TCD systems which include methods based on STFT.

The instantaneous energy at a fixed time t_0 can be obtained from frequency estimators in equation (2.3) by:

$$E(t_0) = \int_{-\infty}^{+\infty} S(t_0, f)df. \quad (2.5)$$

2.6.2 Unit B: The gold standard of detection

After the clinical exam, an analogous conversion is performed on the Doppler digital signal and then the Doppler signal is sent to a loudspeaker. From the audible Doppler signal and from the spectrogram displayed on a screen, we detect and count manually the number of micro-embolic events in order to constitute our gold standard of detection. Micro-embolic signals are identified on the basis of their characteristic sound and from accurate visual inspection of the spectrogram by three blinded expert observers of our laboratory. Then the identified micro-emboli are subject to inter agreement between the three experts. Finally, the positions in time of agreed-on micro-emboli are noted. This gold standard is used to assess the results of the different detectors used and evaluate their performances. As an example, an embolic signature at the time position 1.05 seconds can be visually detected in Figure 2.4.

Genuinely, listening to the audio files by the three experts is made at both the normal speed and a second time at half the normal speed, and even at slower speeds in demanding cases where emboli occurring are hard to distinguish. The latter processes allow detecting several micro-emboli that were previously inaudible at normal speeds. In fact, this particular listening mode allows to overcome the well-known temporal and frequency masking effects in audio files.

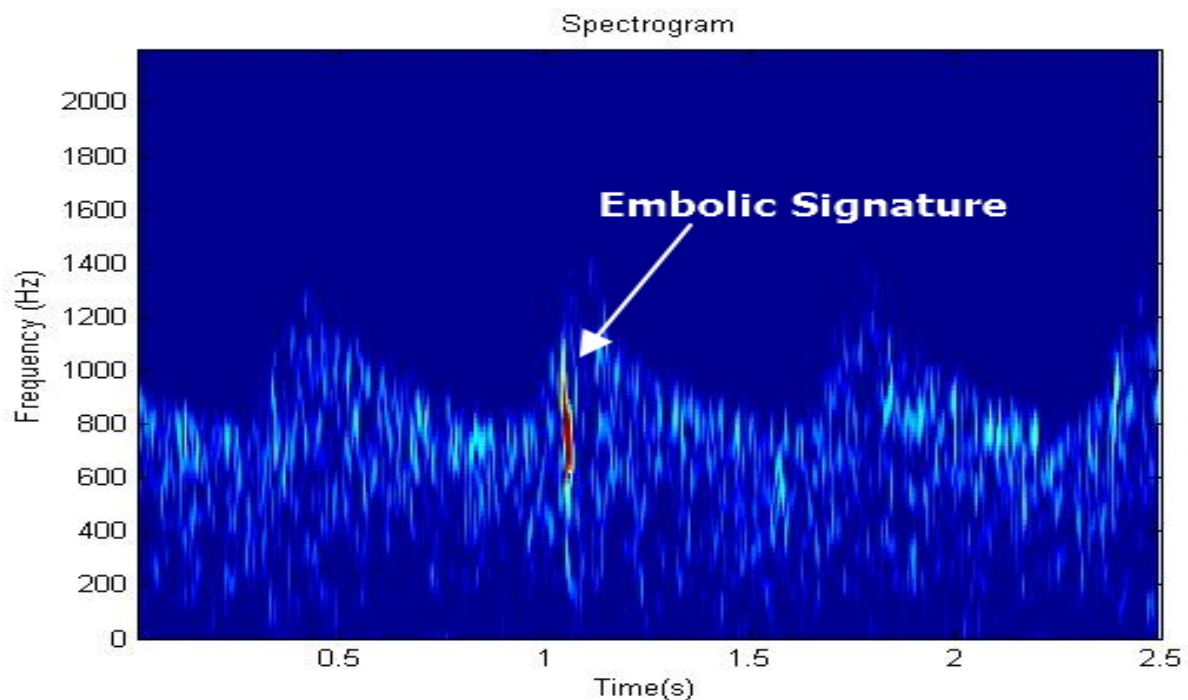


Figure 2.4: Spectrogram: A time-frequency representation obtained from Short Time Fourier Transform calculation. An embolic signature appears at the $t_0=1.05$ seconds.

2.6.3 Unit C: Artefact Rejection

Since embolic particles, during their passage in the blood, evoke a transient intensity increase of the Doppler signal they are popularly referred to as 'High Intensity Transient Signals' (HITS).

At a certain point, some clinicians and researchers had opposed the intensity increases appearing in the Doppler signal to be termed as 'embolic signals' before the true nature of these intensity increases is identified. Otherwise, the 'embolic signal' terminology would be misleading. This can be justified by the presence of signals that are similar to embolic signals and also have the characteristics of being HITS. These are artefact signals.

Artefacts are majorly caused by Doppler probe tapping or displacement. They are also caused by tissue movement imposed by head movement, speech, snoring, sniffing, yawning, coughing, talking, etc.

A main distinctive feature between artefacts and emboli is that artefacts are bidirectional within the Doppler flow spectrum, they exhibit a forward and reverse flow, while emboli are unidirectional exhibiting a forward flow only. This assumption has been widely used [(Spencer et al., 1990), (Markus et al., 1993), (Ringelstein et al., 1998), (Aydin et al., 2004), (Choi et al., 2010), (Serbes et al., 2014)]. However, a study done by Biard et al. (2003), proved that artefacts in some conditions could be exclusively unidirectional in the forward flow.

Moreover, another discrimination factor is that artefacts often have lower Doppler frequencies (< 250 Hz) than emboli (> 600 Hz).

Since probe displacement is a common source of artefacts, the automatic probe used in the Holter TCD system results in an increase in the number of signal artefacts. Moreover, due to the long recording time, the patient is more likely to cause artefacts due to movements and normal actions that are difficult to control. Therefore, by using the Holter, artefact rejection becomes a critical and fundamental step.

The artefact rejection phase included in this unit will be separately described in details in chapter 6.

2.6.4 Unit D: Standard micro-embolic detection

Based on the energy, micro-embolic signals are detected by a binary test used in various methods of detection.

$$E(t) \underset{H_0}{\overset{H_1}{\gtrless}} \lambda. \quad (2.6)$$

If the instantaneous energy $E(t)$ is greater than the detection threshold, then the detector is triggered and an embolus is detected (hypothesis H_1), otherwise no embolus is detected (hypothesis H_0) and the detector remains mute. The choice of the detection threshold, in equation 2.6, is a very crucial step for the identification of embolic signals and in the whole detection process. In standard methods, λ is constant. Two constant thresholds in this study have been used denoted as Threshold 1a and Threshold 1b in Figure 2.3. The first threshold, Threshold 1a, is commonly used in commercial systems. This constant threshold is empirical; i.e. it is fixed empirically by the user for the entire examination. It is patient-, operator-, and device-dependent. This threshold is set above the maximal background energy of the Doppler signal when no embolus is present (Ringelstein et al., 1998). Generally, for manual detection, the threshold is set 3 dB above this energy. For automatic detection, it is usually set between 3 to 9 dB above the background energy and depends on the TCD system calibration (Ringelstein et al., 1998). Since the setting of this threshold is not the same for different examinations,

2.7. CONCLUSION

comparisons between various applied methods are hard to achieve.

Another strategy for applying constant thresholds for embolus detection have been made possible by our research group (Girault, 2013). The team searched for a constant threshold that could be calculated from the energy data. Therefore, unlike empirical thresholds, the operator would avoid making a choice of the threshold value which might often lead to either an overly high threshold that makes the detection of small events impossible or an overly low threshold that detects unnecessary false events.

After proving that the energetic information follows Gaussian law (Girault, 2013), a constant statistical threshold (Threshold 1b in Figure 2.3) was established from the instantaneous energy in the following manner:

$$\lambda = \mu + m\sigma \quad (2.7)$$

μ is the mean of the instantaneous energy, σ is the standard deviation and m is a forgetting factor that ensures adaptability of the threshold throughout the examination. This threshold depends on a pre-setting preparation phase. Since the energy is made up of a great number of sample points, a threshold $\lambda = \mu + 3\sigma$ corresponding to 99.97 % of the values in the Gaussian function, is not well adapted. The threshold λ must be at least higher than $\mu + 3\sigma$. Mainly, optimal values of m range between 3 and 5.

2.7 Conclusion

In this chapter, we have introduced the instrument of micro-embolus detection along with the new enhanced Holter modality we will be using. We have also presented the main specifications of embolus detection by TCD. Moreover, we presented the reference off-line standard detection procedure. In the next part of this dissertation we will introduce the different micro-embolic detectors we have developed.

Part II

High Intensity Transient Signals Detection

Chapter 3

A Micro-embolic Energy Detector based on Energy Fluctuations

3.1 Introduction

The standard detection presented in the previous part is not sufficiently accurate and robust for the detection of small weak micro-emboli. In this chapter, we propose an original paradigm of detectors based on energy fluctuations rather than on the energy signal, and we develop a time-varying threshold rather than using constant thresholds. The latter proposed detection will be compared to the standard detections discussed in part I.

We will show in the course of the chapter several hypothesis that render the new proposed detector as a strong tool for the detection of the smallest micro-emboli. The results will also prove that the performance of the new proposed detector is superior to existing standard detectors. This work was published as a proceeding at the IEEE 'Third International Conference on Advances in Biomedical Engineering'. It is also currently submitted to the 'Journal of Biomedical and Health Informatics'.

3.2 Micro-embolic detection based on energy fluctuations

Although the instantaneous energy is time-varying as shown in Figure 3.1, in standard methods this energy is compared to a constant threshold. This is a main reason behind the poor performances of energy based detectors with constant thresholds. This has stimulated our team to achieve the detection process with a novel approach. The procedure detection diagram is represented in Figure 3.2 (We note that the processing steps from the Doppler signal extraction to the energy calculation are repeated similarly to the standard detection of part I).

The new method we propose, is based on the fact that emboli appear in the energy signal's positive fluctuations (Figure 3.1 b)) part only. Thus by constructing a time-varying threshold from the negative energy fluctuations (Figure 3.1 c)) and then applying it on the positive fluctuations, the technique would be perfect in displaying the smallest suspicious embolic events occurring in the positive fluctuations.

First of all, lets consider the blood energy Doppler signal and suppose it is composed of

two time-varying components:

$$E_{Blood}(t) = E_{LF}(t) + E_{HF}(t) \quad (3.1)$$

The low frequency time-varying component $E_{LF}(t)$, of 1st order statistics, is related to the cardiac rhythm which is a pulse component of about 1 Hz. The high frequency time-varying component $E_{HF}(t)$, of 2nd order statistics, is related to the random fluctuations due to the random positions of billions of red blood cells travelling into the blood flow. This component is heteroskedastic (Girault et al., 2010) since the variance is not constant. In a previous work (Girault, 2013), it was shown that this random component is governed by a Gaussian law of symmetric probability density. Note the similarity of this model reporter in (3.1) and the one based on the non-stationary Wold's theorem (Bierens, 2012) where it decomposes in two components:

$$E_{Blood}(t) = E_d(t) + E_s(t) \quad (3.2)$$

where $E_d(t)$ is a time varying deterministic component and $E_s(t)$ is a time-varying stochastic component.

Subsequently, lets consider the total Doppler energy signal and suppose that it is composed of two components:

$$E_{total}(t) = E_{Blood}(t) + E_{HITS}(t) \quad (3.3)$$

where $E_{Blood}(t)$ is defined in (3.1) and where $E_{HITS}(t)$ is a high intensity transient signal (HITS) describing the micro-embolic Doppler signature. The micro-embolic Doppler signal is an energetic component that is strictly positive. HITS are unknown deterministic signals whose shape is related to the instrumentation and the geometry of the probe. Their amplitude and position are unknown.

The new method that we propose consists primarily in removing the cyclic cardiac low frequency component from the blood energy signal. In most approaches this is done by using a narrow band filter or a high pass filter. In the present study, it is done first by evaluating the trend $E_{LF}(t)$ through a smoothing step and then by subtracting it from $E_{blood}(t)$. This is represented in Figure 3.1 a). The Doppler energy signal is represented as sum of two parts; one superior (in cyan) and one inferior (in green) to the smooth curve (in red). In other words one representing the upper variations in the distribution of the energy signal from its trend over time and one representing the lower variations.

When the smooth curve is subtracted from the energy, the remaining fluctuation $\gamma(t)$ can be decomposed into a positive fluctuation $\gamma_{pos}(t)$ and a negative fluctuation $\gamma_{neg}(t)$:

$$\gamma(t) = \gamma_{pos}(t) + \gamma_{neg}(t) \quad (3.4)$$

where $\gamma_{neg}(t) = \gamma(t) < 0$ (represented in Figure 3.1 b) in green) and $\gamma_{pos}(t) = \gamma(t) > 0$ (represented in Figure 3.1 c) in cyan)

Moreover, the probability density of this energy, following a Gaussian distribution (Girault, 2013) is also a summation of the probability densities from the positive and negative parts of the energy.

$$P_\gamma(t) = P_{pos}(t) + P_{neg}(t) \quad (3.5)$$

As the Gaussian probability density is even, it comes:

$$P_{\gamma_{pos}} = P_{\gamma_{neg}} \quad (3.6)$$

$P_{\gamma_{pos}} = P_{\gamma} \cdot \theta(\gamma)$ where $\theta(\gamma)$ is the Heaviside function and where $P_{\gamma_{neg}} = P_{\gamma} - P_{\gamma_{pos}} = P_{\gamma} \cdot \theta(-\gamma)$

Hence, the positive part of the energy represents the same fluctuations as the negative part but corrupted with High Intensity Transient Signals (HITS), that are outside the Gaussian statistics. In other words, the positive part of the energy is symmetric to the negative one except when HITS occur. Thus, by using the symmetrical property of the probability density of the Gaussian fluctuation, it is possible to calculate a time varying threshold based only from the negative amplitude of the fluctuation and then apply it on the positive part to eliminate the high frequency information and detect the strictly positive micro-embolic HITS.

Consequently, the micro-embolic signals can be detected by the binary test in equation 2.6 where it is now written as:

$$\gamma(t) \underset{H_0}{\overset{H_1}{\geq}} \lambda(t) \quad (3.7)$$

If the instantaneous energy fluctuation $\gamma(t)$ is greater than the detection threshold, then an embolus is detected (hypothesis H_1), otherwise no embolus is detected (hypothesis H_0).

Knowing that the Doppler signal is quasi-cyclostationary, the quasi-periodically time varying threshold $\lambda(t)$ is proposed as an envelope calculated from the negative energy fluctuations (Fig. 3.1 b)):

$$\lambda(t) = \mu(t) + m\sigma(t). \quad (3.8)$$

where $\mu(t)$ is the "instantaneous" mean and $\sigma(t)$ the "instantaneous" standard deviation given by equation 3.9. The parameter m results from an optimization training process that increases the detection rate and reduces the false alarm rate (see section 3.3).

$$\sigma(t) = k | -\gamma_{neg}(t) + jHT[\gamma_{neg}(t)]|. \quad (3.9)$$

with $HT[.]$ the Hilbert transform.

This envelope is then transferred and applied onto the positive energy fluctuations (Fig. 3.1 c)) where the detection process in equation (3.7) is performed. When the signal in the positive energy fluctuation is higher than the time-varying threshold, the automatic detector is triggered and the peak is recorded.

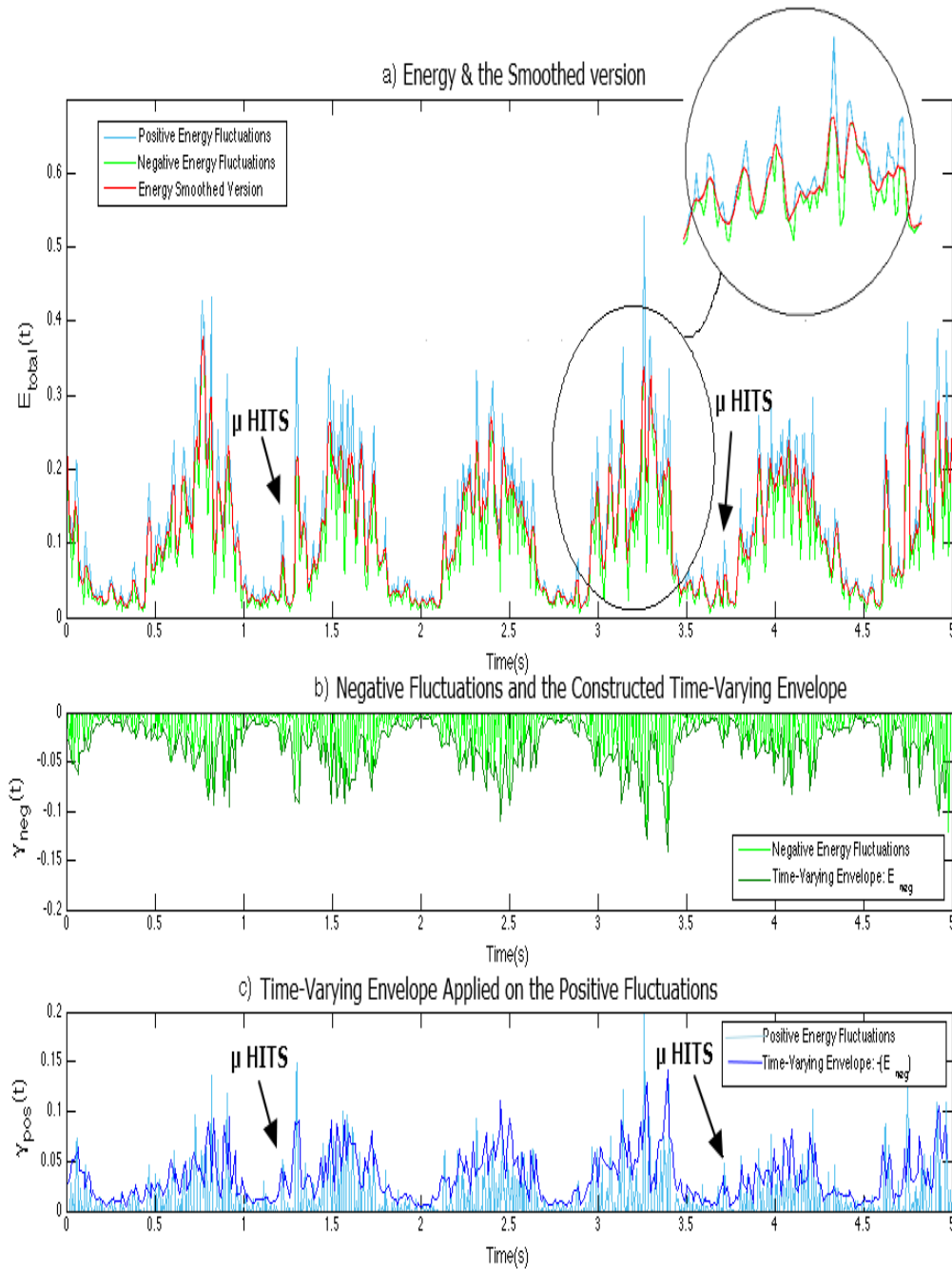


Figure 3.1: Application of our detection technique based on negative energy fluctuations. a) The energy signal is represented as sum of two parts; one superior (cyan) and one inferior (green) to the smoothing curve (red). b) The smoothing curve is subtracted from the energy part inferior to it resulting in negative energy fluctuations (green). A negative time-varying envelope $E_{neg}(t)$ is then constructed (dark green). c) The smoothing curve is subtracted from the energy part superior to it resulting in positive energy fluctuations (cyan). The negative time varying envelope is opposed and applied as $-(E_{neg}(t))$ (blue).

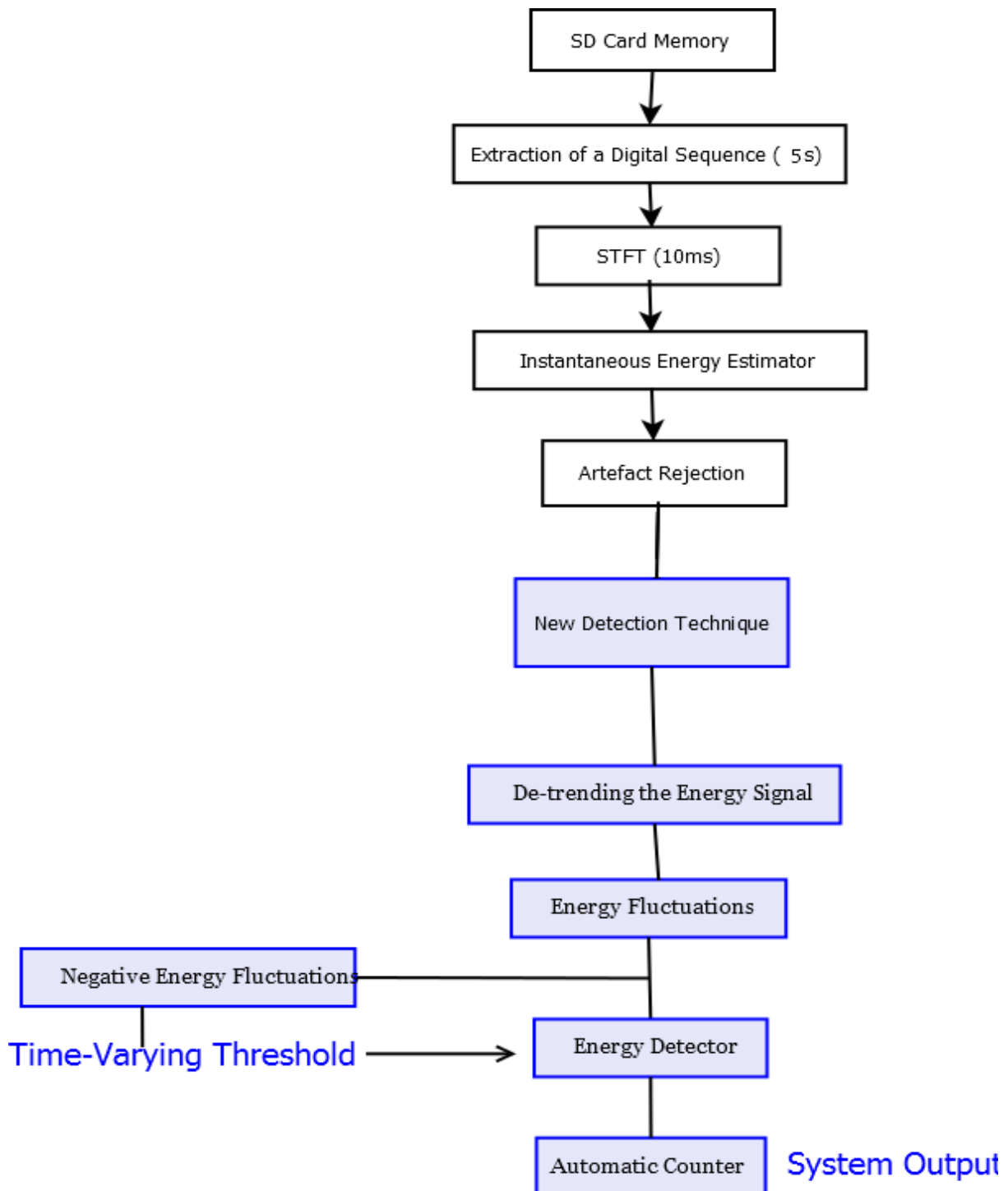


Figure 3.2: The procedure of the new detection system proposed. After STFT and energy calculation, the energy signal is de-trended, and energy fluctuations are obtained. The micro-embolic energy detector is based on the negative part of the energy fluctuations, from which a time-varying threshold is constructed.

3.3 Results

Our database, composed of 25 signals, is divided into two categories. The first category includes 10 signals dedicated to achieve the training phase. The training phase allows adjusting the best values through maximizing the detection rate and minimizing the false alarm rate. The second category comprised 15 signals on which the experimentation methods are tested and results are obtained.

In this part, we present the results obtained during the training and the testing phases for the standard detectors presented in part I and the new proposed detector. First, we determine the optimal training phase settings. Second, we prove the homogeneity of our dataset. Finally, we compare the optimal testing phase results of the standard and new detectors and we evaluate the performance of the new detector.

To evaluate the results of the different detectors, we compare these results to the gold standard of detection established initially. The basic statistical tools calculated for our evaluation are:

1. Detection Rate (DR) or Sensitivity calculated as the number of true positive detections / the number of gold standard detections. True positive detection refers to the detection of an embolus recorded in the gold standard.
2. False Alarm Rate (FAR) calculated as the number of false positive detections / the total number of detections. False positive detection refers to the detection of an embolus not recorded in the gold standard or in other words an embolus which has not crossed the sample volume. The false alarm rate is also written as $(1 - \text{specificity})$.

3.3.1 Training phase for the different thresholds

Since setting the empirical threshold is achieved by an operator, micro-embolic detection could vary between one operator and another. In this study, and to overcome this drawback, an automatic threshold-searching is proposed based on the training phase. Values ranging between 3 dB and 9 dB are tested. The results for the different threshold values applied are shown in Figure 3.3. The best threshold setting is obtained for a value of 5 dB which best maximizes the percentage detection and minimizes the false alarm rate.

We also propose to find the optimal value of m for the statistical constant threshold $\lambda = \mu + m\sigma$ through the training phase. Values of m ranging between 3 and 6 are tested. The results for the different threshold values applied are shown in Figure 3.4. The best threshold setting is obtained for a value of $m = 4.5$ which best maximizes the percentage detection and minimizes the false alarm rate. Thus, $\lambda = \mu + 4.5\sigma$ must be used.

We also propose to find the optimal value of m for the time-varying threshold $\lambda(t) = \mu(t) + m\sigma(t)$ through the training phase. Values of m ranging between 3 and 7 are tested. The results for the different threshold values applied are shown in Figure 3.5. The best threshold setting is obtained for a value of $m = 6.5$ which best maximizes the percentage detection and minimizes the false alarm rate. Thus, $\lambda(t) = \mu(t) + 6.5\sigma(t)$ must be applied.

3.3. RESULTS

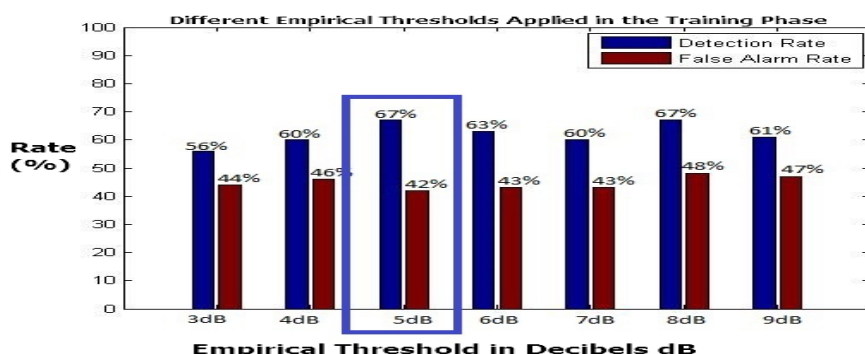


Figure 3.3: Detection and False Alarm rates obtained when constant empirical thresholds with values ranging between 3 dB and 9 dB, above the maximal background energy (defined in section 2.5) of the Doppler signal when no embolus is present (Ringelstein et al., 1998), are applied in the training phase. The best results are obtained with threshold setting of 5 dB with 67 % detection rate and 42 % false alarm rate.

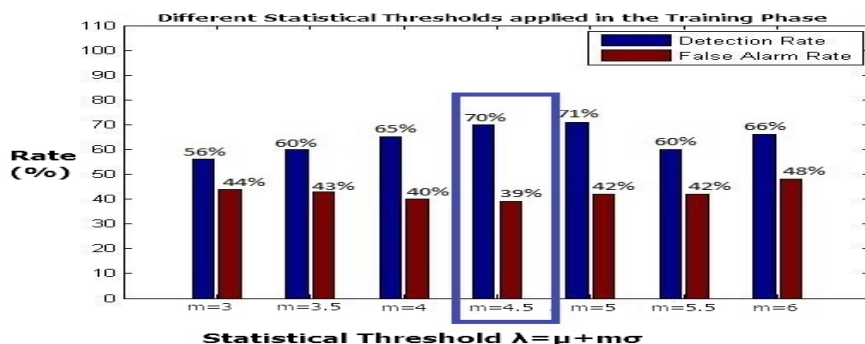


Figure 3.4: Detection and False Alarm rates obtained when statistical constant thresholds $\lambda = \mu + m\sigma$ are applied with m values ranging between 3 and 6 in the training phase. The best training phase setting is obtained for $\lambda = \mu + 4.5\sigma$ with 70 % detection rate and 39 % false alarm rate.

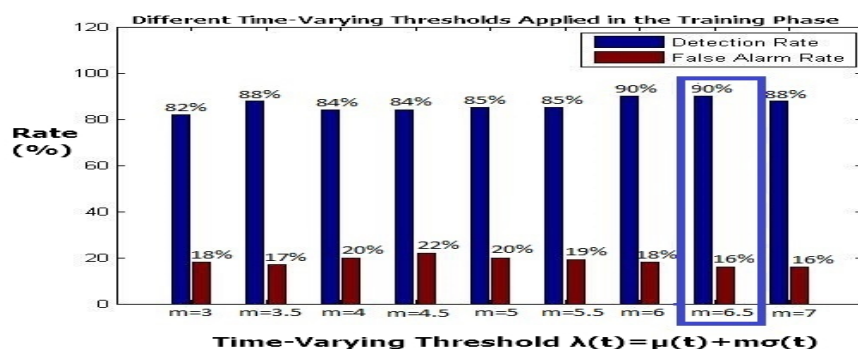


Figure 3.5: Detection and False Alarm rates obtained when time-varying thresholds $\lambda(t) = \mu(t) + m\sigma(t)$ are applied in the training phase with m values ranging between 3 and 7. The best training phase setting is obtained for $\lambda(t) = \mu(t) + 6.5\sigma(t)$ with 90 % detection rate and 16 % false alarm rate.

3.3.2 Demonstrating the homogeneity of our database

Homogeneity is a solid indicator that the statistical properties of one part of an overall database are the same as any other part. Proving the homogeneity of our database is an important step which verifies the feasibility of using the different threshold settings established in the training phase onto the testing phase.

To prove the homogeneity of our database, we apply the same empirical, statistical and time-varying thresholds values that were applied on the training phase onto the set of signals compromising our testing phase. Figures 3.6, 3.7, and 3.8 show the results obtained when the same thresholds are applied in the training and testing phases.

By comparing the results in Figure 3.6a) to Figure 3.6b), in Figure 3.7a) to Figure 3.7b), and Figure 3.8a) to Figure 3.8b), it is clear that the results in both training and testing phases are very similar. This proves the homogeneity of our chosen dataset.

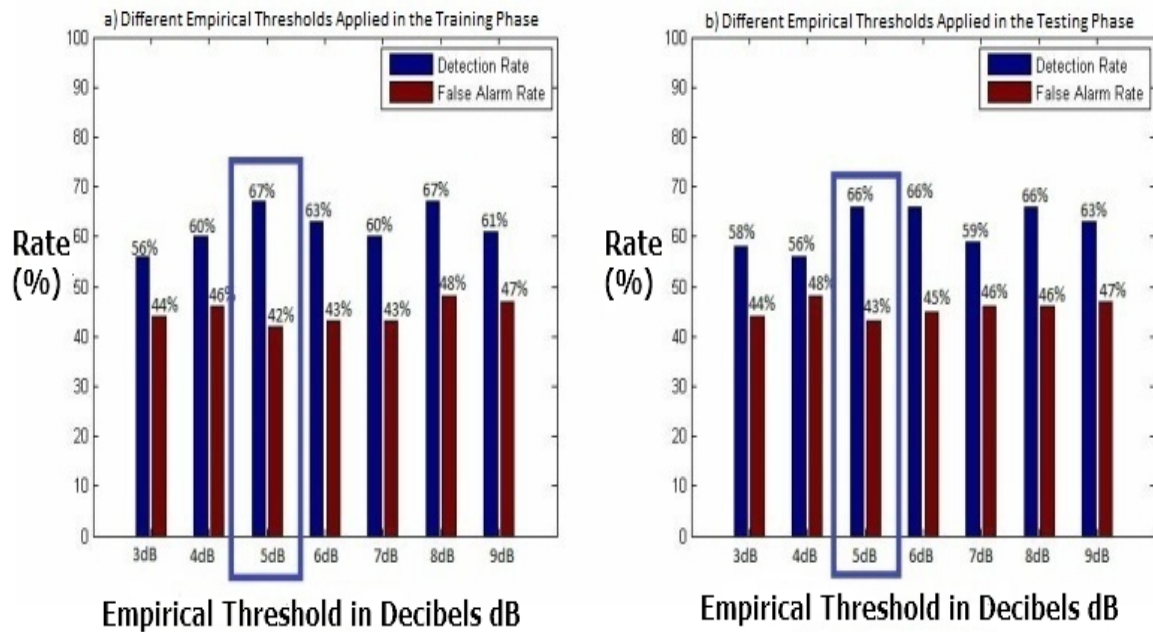


Figure 3.6: Detection and False Alarm rates obtained when constant empirical thresholds with values ranging between 3 dB and 9 dB, are applied in the a) Training and b) Testing phases respectively. a) The best threshold setting is obtained with 5 dB. b) The best testing results are obtained with threshold of 5 dB with 66 % detection rate and 43 % false alarm rate. The results in a) and b) reflect the homogeneity of our database.

3.3.3 Comparison of the best testing phase results for the three detectors

Finally, in order to assess the performance of our new detector, we shall compare the best testing phase results obtained with those of the constant threshold detection methods. Figure 3.9 summarizes the best testing phase results for the three energy detectors. For the standard

3.3. RESULTS

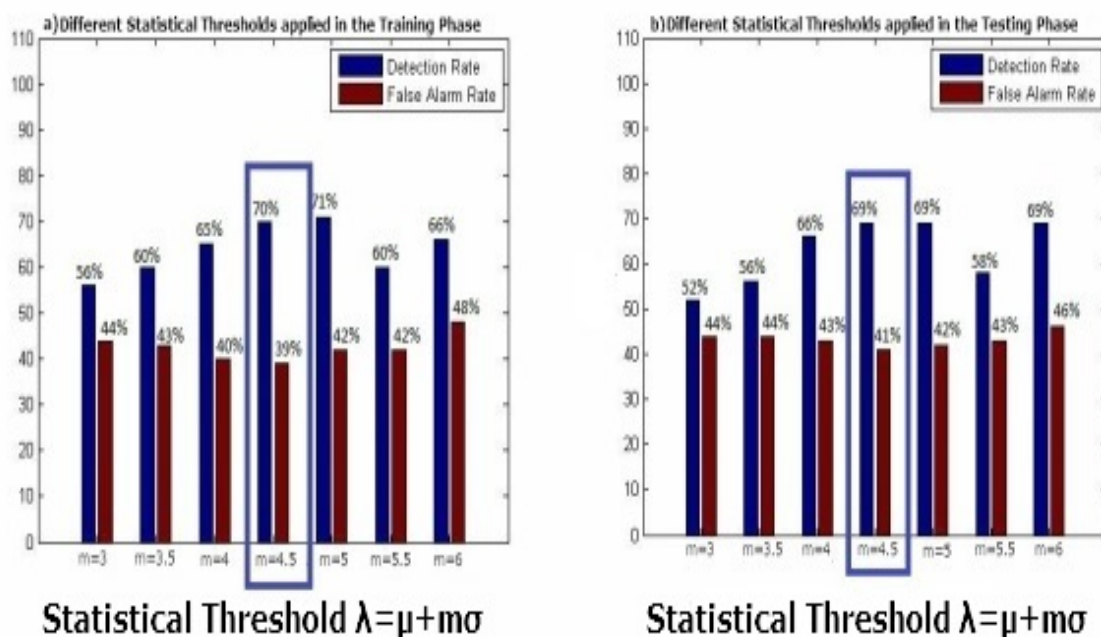


Figure 3.7: Detection and False Alarm rates obtained when statistical thresholds $\lambda = \mu + m\sigma$ are applied with m values ranging between 3 and 6 in the a) Training and b) Testing phases respectively. a) The best training phase setting is obtained with $\lambda = \mu + 4.5\sigma$. b) The best testing results are obtained with $\lambda = \mu + 4.5\sigma$ with 69 % detection rate and 41 % false alarm rate. The results in a) and b) reflect the homogeneity of our database.

energy detector with empirical threshold, the FAR is 43 %, and the DR is 66 %. For the energy detector with statistical threshold, the FAR is 41 %, and the DR is 69 %. For the energy detector based on negative energy fluctuations with a time varying threshold, the FAR is 14 % and the DR is 89 %.

The results presented, show that our new detector is able to reduce the FAR by more than half of the standard value and the values obtained with statistical thresholds. The detection rate achieved by our new detection system is increased by 20 % compared to that achieved by standard detection and detection based on statistical thresholds. Thus, the superiority of the new negative energy fluctuations-based detector compared to standard detectors based on constant thresholds is conspicuous.

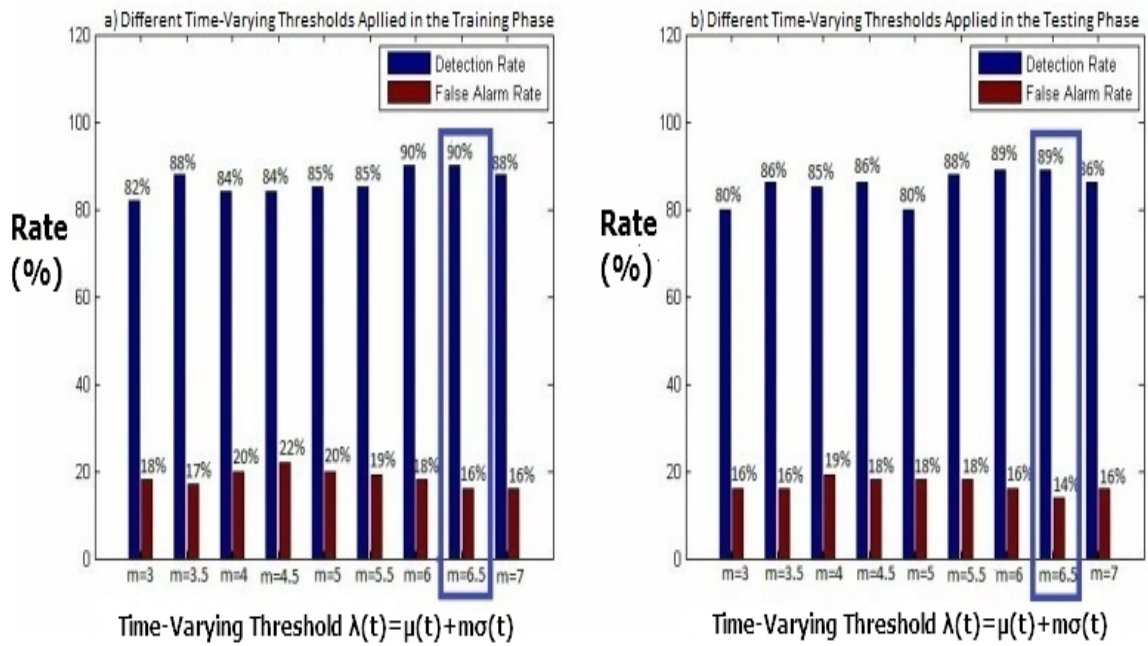


Figure 3.8: Detection and False Alarm rates obtained when time-varying thresholds $\lambda(t) = \mu(t) + m\sigma(t)$ are applied with m values ranging between 3 and 7 in the a) Training and b) Testing phases respectively. a) The best training phase setting is obtained for $\lambda(t) = \mu(t) + 6.5\sigma(t)$. b) The best testing results are obtained for $\lambda(t) = \mu(t) + 6.5\sigma(t)$ with 89 % detection rate and 14 % false alarm rate. The results in a) and b) reflect the homogeneity of our database.

3.3. RESULTS

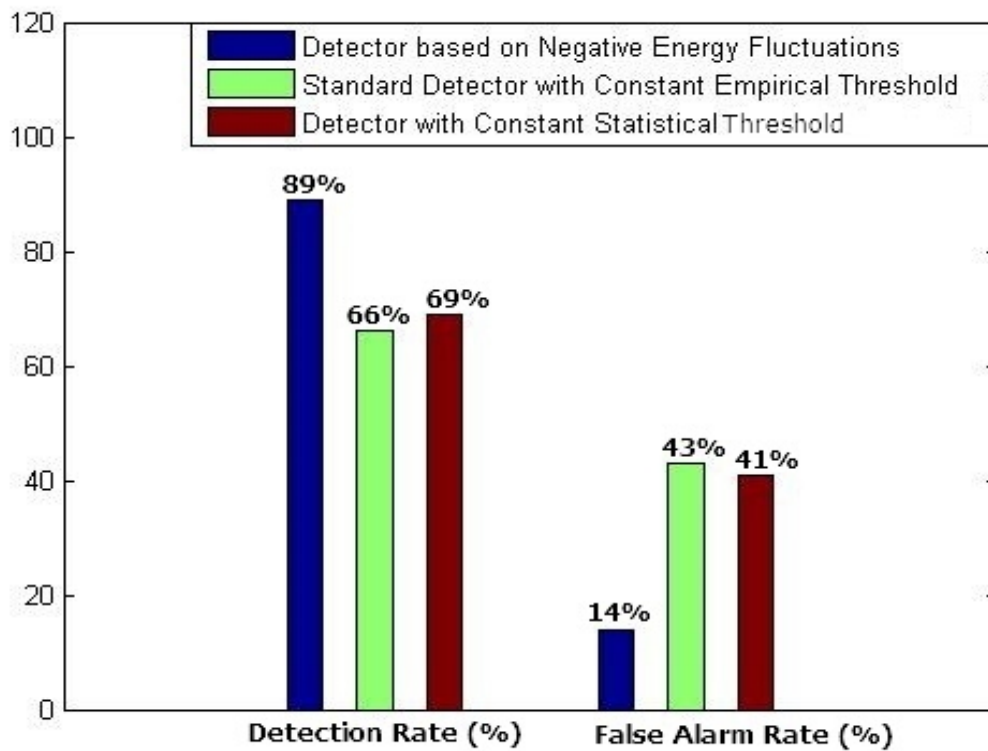


Figure 3.9: Comparison of the percentage detection and false alarm rate results for the energy detector based on negative energy fluctuations, standard detector with empirical threshold and detector with statistical threshold. The negative energy fluctuations-based detector reduces the FAR compared to the standard values and the values obtained with statistical thresholds. The detection rate achieved by the new detection system is increased compared to that achieved by standard detection and detection based on statistical thresholds.

3.4 The relative intensity increase of the smallest detectable micro-embolus

In an aim to discover the characteristic embolus relative intensity increase that the different detectors are capable of detecting we choose a sample of 175 embolic events having intensity increases below 15 dB. For each detector we evaluate the embolic events that it is capable of detecting and we discover out of these detections the embolus with the smallest relative intensity increase. The results are presented in Figures 3.10.

As can be depicted in Figure 3.10, the detection using constant empirical thresholds is able to detect all emboli having intensity increases above 5.8 dB. However, embolic events whose intensity increase is below 5.8 dB are never detected. The detection based on statistical constant thresholds is able to detect all emboli having intensity increases above 4.1 dB. The negative energy fluctuations-based energy detector is able to detect micro-embolic signatures with relative intensity increases as low as 0.8 dB.

We can deduce from the latter results that the negative energy fluctuations based detector is able to detect the smallest embolic signatures.

To be noted that the micro-embolic size corresponding to these relative intensity increase values are provided in the appendix.

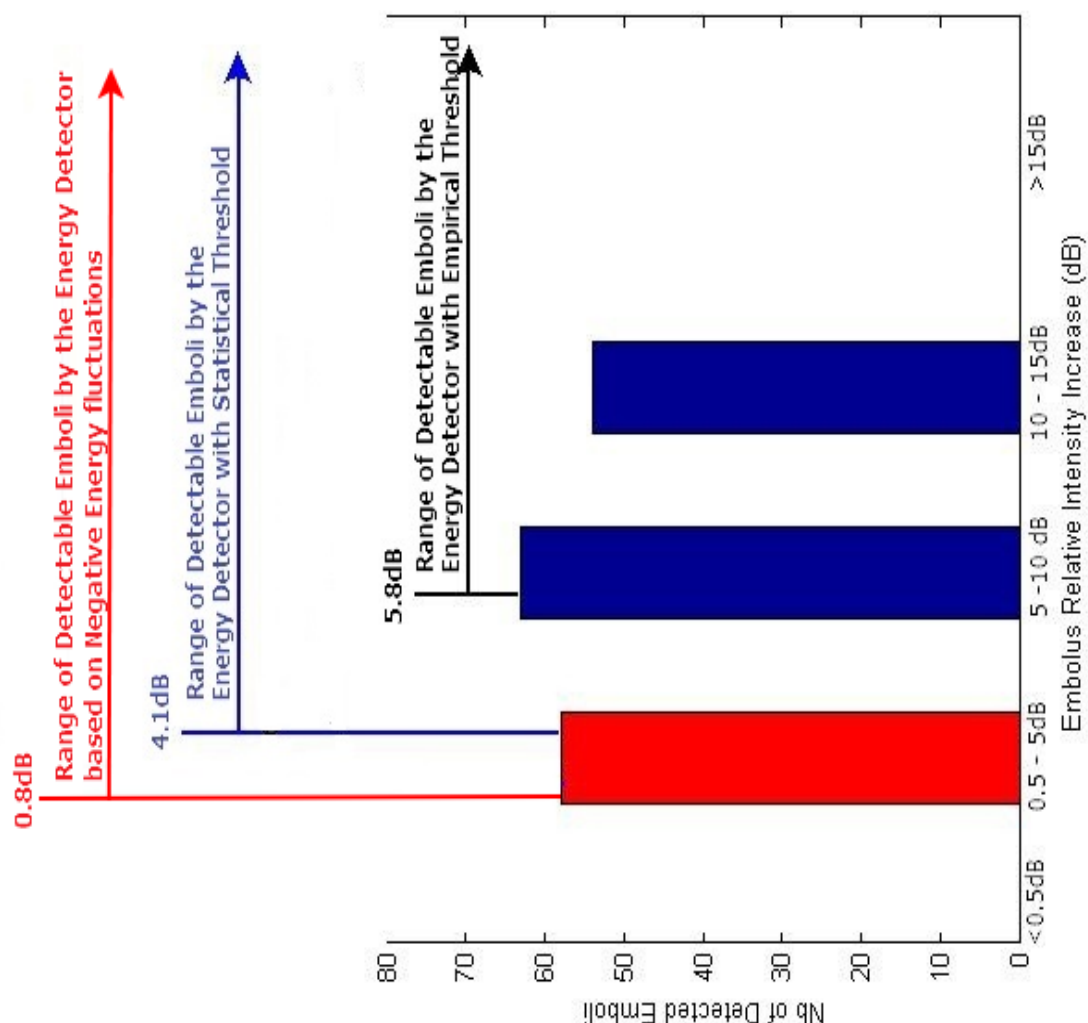


Figure 3.10: Embolus Intensity Increases relative to background blood energy for a sample of 175 chosen embolic events. The smallest detectable embolus by detection with constant empirical threshold is as low as 5.8 dB. The smallest detectable embolus by detection with constant statistical threshold is as low as 4.1 dB. The smallest detectable embolus by the energy detector based on negative energy fluctuations is as low as 0.8 dB

3.5 Conclusion

In this chapter, a micro-embolic energy detector built from energy fluctuations, is proposed as a method to overcome major limitations of standard energy detectors. The performance of standard energy detectors in detecting weak micro-embolisms is poor. This problem is effectively eliminated by the detection procedure we propose which mainly consists in constructing an instantaneous time varying envelope from the negative energy fluctuations. Based on energy fluctuation properties of the Doppler signal, the new method is able to detect the smallest

micro-emboli that may occur during the cardiac cycle.

By stating that micro-embolic signatures occur only in the positive part of the energy signal fluctuations, the innovative idea is to construct an instantaneous threshold from the negative part of these fluctuations while hypothesizing that the instantaneous energy follows Gaussian statistical distribution. This threshold, would next be applied on the positive energy fluctuations. Micro-embolic signals, in the positive fluctuations, would appear as signatures exceeding this threshold.

Results upon application on real signals show that it can offer significant improvements compared to standard methods using empirical thresholds, the most popular methods commercially available, and standard detection methods using Gaussian statistical constant thresholds. The results are based on adjusted settings that tend to minimize the false alarm rate while maximizing the detection rate. Improvements include increasing the percentage of detection from 66 % and 69 % for standard detectors using empirical and statistical thresholds, respectively, to around 89 %. Also, the false alarm rate is reduced from 43 % and 41 % for standard detectors using empirical and statistical thresholds, respectively, to around 14 %. Moreover, the new detection technique allows the detection of micro-emboli having relative intensity increase as low as 0.8 dB compared to as low as 5.8 dB and 4.1 dB for the detectors with empirical and statistical threshold, respectively . Consequently, we affirm that a detector based from negative energy fluctuations would be more reliable and vigorous than standard techniques and well adapted for the precise detection of the smallest micro-emboli.

In the next chapter, we will couple this new detection method with sub-band decomposition which is another strong tool for significantly improving the detection of micro-emboli.

Chapter 4

Coupling of a Negative Energy Fluctuations-Based Detector with Sub-band Decomposition: A Highly Performing Embolus Detection Technique

4.1 Introduction

In the artery, the micro-embolus particularly travels on a single speed line as shown in Figure 4.1. Compared to the wide band Doppler blood flow signal, the Doppler micro-embolic signal can be considered as narrow band. The energy in this narrow band reflects the energy backscattered by the traveling micro-embolus as well as the energy backscattered by all Red Blood Cells (RBC) traveling on the same velocity line as the micro-embolus.

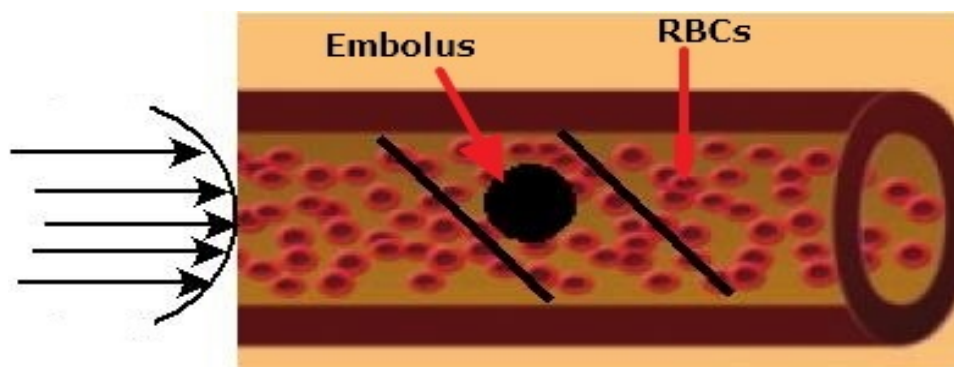


Figure 4.1: An illustration of an embolus traveling in a blood vessel. The trajectory of blood flow is defined by a parabolic curve. The embolus travels on a single speed line in the vessel.

Indeed, reducing the frequency band, definitely leads to reducing the number of RBC contributing in the background Doppler signal. Only RBCs traveling at the same speed as the micro-embolus will be considered instead of considering all RBCs present in the region of interest. This is shown in Figure 4.2.

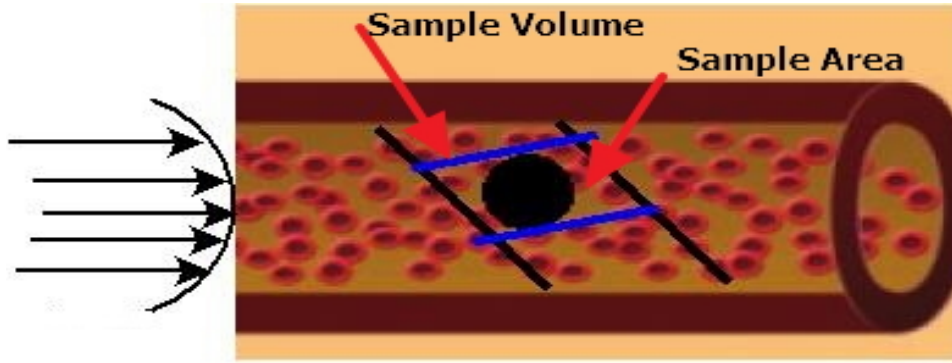


Figure 4.2: Reducing the sample volume where the embolus is present to sample areas. Only RBCs traveling at the same speed line as the micro-embolus (same sample area) will be considered instead of considering all RBCs present in the whole sample volume.

The latter process can be achieved through sub-band decomposition which allows decomposing the whole Doppler spectral band into several bands. Through this decomposition, we reduce the bandwidth in which detection is applied. This in turn allows reducing the background Red Blood Cells in the inspected bandwidth. Consequently, decomposing the whole Doppler frequency band will amplify the contrast between the micro-embolic signature and the background signal in each decomposed channel.

Based on this hypothesis, several studies introduced the use of sub-band decomposition to improve micro-embolus detectability. The first of these methods was that introduced by Markus et al. (1999) where a bank of narrow band filters with the same width were used. Later, Aydin et al. (2004) introduced sub-band decomposition through the discrete wavelet transform, before the wavelet packet decomposition was used for sub-band division by Girault (2013). By using these different kinds of filters, the difficulty mainly lies in the choice of the constant threshold in each sub-band and on the merging of the detection since a micro-emboli can appear in several consecutive sub-bands.

Therefore, we tend to introduce in this chapter sub-band decomposition as a strong tool for enhancing micro-embolus detection while enhancing the detection in each sub-band through optimizing the constant thresholds used and later by using the time-varying threshold introduced in chapter 3. We also propose a novel algorithm that ensures robust merging between the detections from the different sub-bands. This work was published as a proceeding at the IEEE 'Third Middle East Conference on Biomedical Engineering'.

4.2 The Micro-Embolic Short Time Fourier Transform Sub-band Detection Unit

The sub-band detection unit is made up of the same phases presented in chapter 3, but the detection process is simultaneously carried out in each sub-band. The spectral band is divided into several narrow sub-bands and the detection is operated independently in each sub-band. The overall sub-band detection unit can be viewed in Figure 4.4. Initially, after loading the wave-file, STFT calculation (by equation 2.3) is performed on repetitive 5 second segments of the extracted Doppler signal. This is shown in the first 3 blocks in Figure 4.4.

4.2. THE MICRO-EMBOLIC SHORT TIME FOURIER TRANSFORM SUB-BAND DETECTION UNIT

Sub-band decomposition is then applied to decompose the STFT whole band into n ideal sub-bands through a bank of n ideal rectangular frequency filters. This decomposition is depicted in Figure 4.3 and represents Part 1 of Figure 4.4. The decomposition through rectangular filters is defined by the following equation:

$$S_f \times \text{rect}_B \left(\frac{f - kB/2}{B} \right) \quad (4.1)$$

with $B=fs/8$ and k is odd

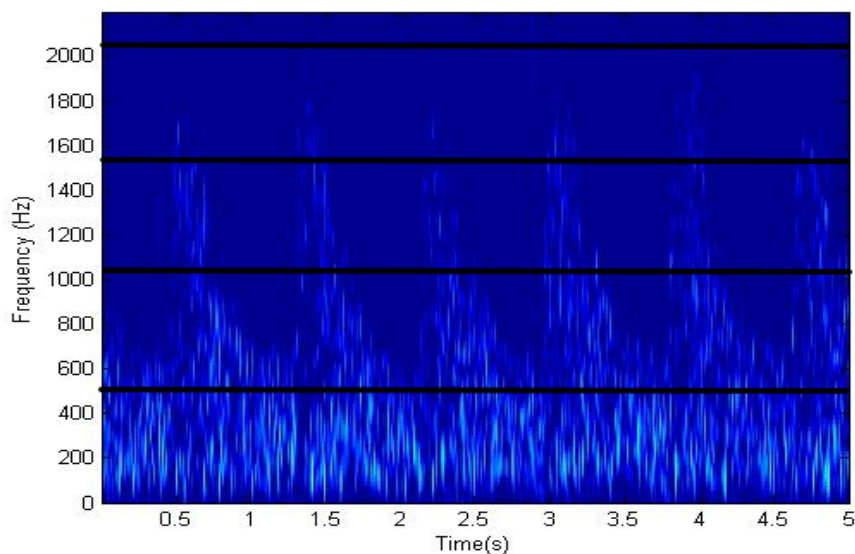


Figure 4.3: Decomposition of the whole Doppler frequency spectrum into n ideal sub-bands through n ideal rectangular filters.

Then energy calculation (by equation 2.5) is performed in each sub-band. The new energy detector is composed of n detectors associated to n Doppler frequency sub-bands. The process can be viewed in Part 2 of the detection unit in Figure 4.4. Also, in Figure 4.5 we display a signal (5 second extracted segment) that has been decomposed into four sub-bands.

In the next step, presented in Part 3 of the detection unit in Figure 4.4, the micro-embolic signal detection is achieved by comparing the sub-band energy to a threshold. The binary test is presented in equation 4.2. E_n is the instantaneous energy calculated in the n^{th} sub-band. λ_n is the threshold of sub-band n . The subscript n denotes that the binary test is carried out in the sub-band n . In the first hypothesis (H_0), the energy is lower than the detection threshold and thus no detection is reported. In the other case (H_1), the energy exceeds the threshold and thus an embolic event is recorded.

$$E_n(t) \begin{cases} < \lambda_n, \text{Hypothesis } H_0, \\ > \lambda_n, \text{Hypothesis } H_1. \end{cases} \quad (4.2)$$

The threshold λ could be any of the thresholds we already presented in the previous chapter, the constant empirical threshold, the constant statistical threshold and the negative energy

fluctuations-based time-varying threshold. In Figure 4.6 we show how the negative energy fluctuations-based time-varying threshold (previously presented in chapter 3 in Figure 3.1) is applied in sub-band detection. Although this process is repeatedly applied in each sub-band, due to space complications we are not able to show it for each of the 4 sub-bands in one figure. It is only shown for sub-band 2 as an example.

After sub-band decomposition, the Doppler signal $x(t)$ can be expressed as follows:

$$x(t) = \sum_{n=1}^{N_{sb}} x_n(t) \quad (4.3)$$

where N_{sb} is the total number of channels (sub-bands) and $x_n(t)$ is the signal in the n^{th} sub-band.

Also, the total instantaneous energy over the whole spectral band can be obtained by summing the contribution of all channels:

$$E(t) = \sum_{n=1}^{N_{sb}} E_n(t). \quad (4.4)$$

4.2. THE MICRO-EMBOLIC SHORT TIME FOURIER TRANSFORM SUB-BAND DETECTION UNIT

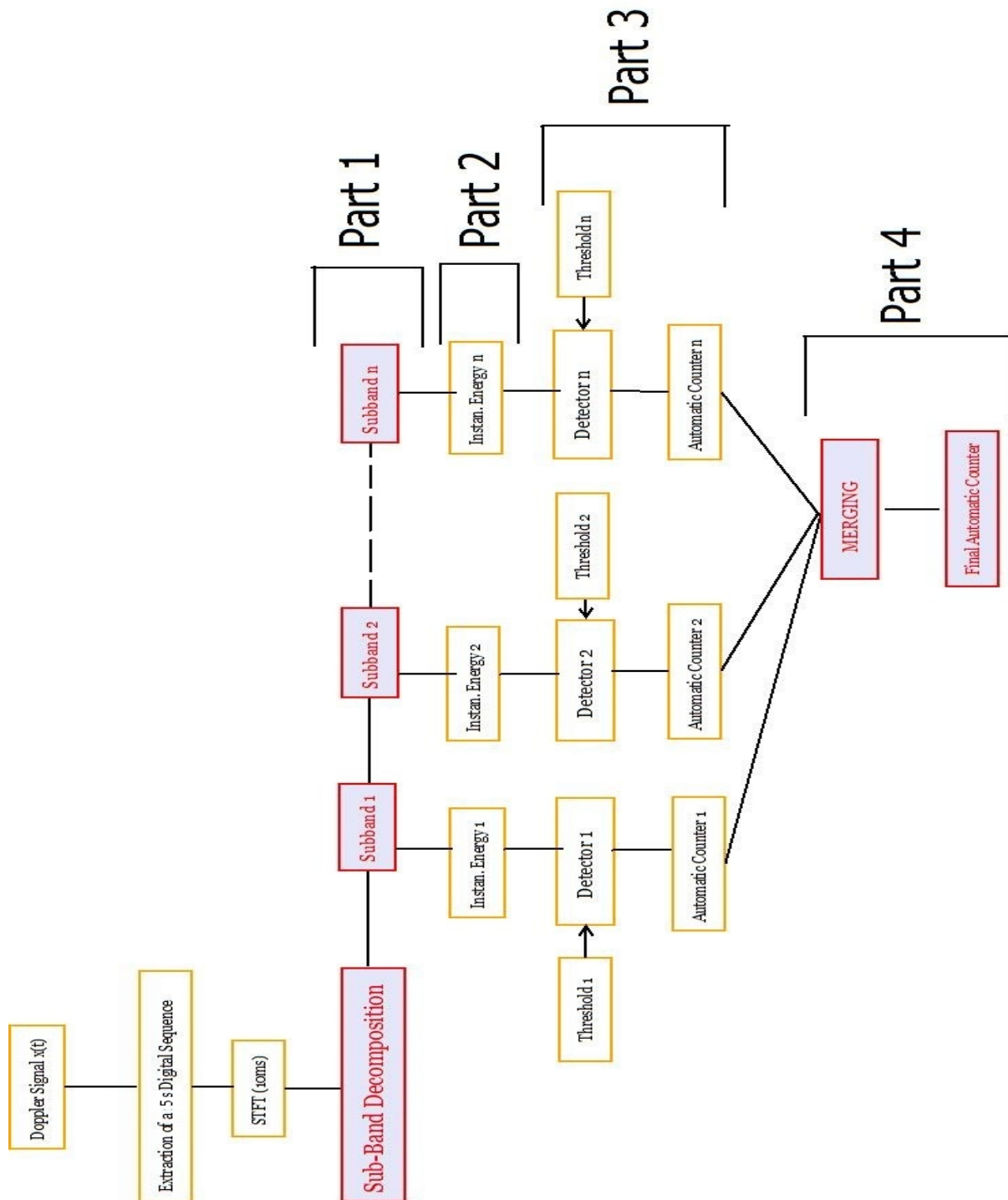


Figure 4.4: Sub-band Decomposition-based embolus detection system. After acquiring the Doppler signal, Short Time Fourier Transform is calculated for 5 second digital sequences. In Part 1, sub-band decomposition through a bank of n ideal frequency filters is applied. In Part 2, the instantaneous energy is estimated in each sub-band. Next in Part 3, the detection binary test is performed where the energy is compared to a detection threshold and the counter is triggered at energies exceeding the threshold. Lastly, in Part 4, all detections from each sub-band are merged and automatically counted.

CHAPTER 4. COUPLING OF A NEGATIVE ENERGY FLUCTUATIONS-BASED
DETECTOR WITH SUB-BAND DECOMPOSITION: A HIGHLY PERFORMING
EMBOLUS DETECTION TECHNIQUE

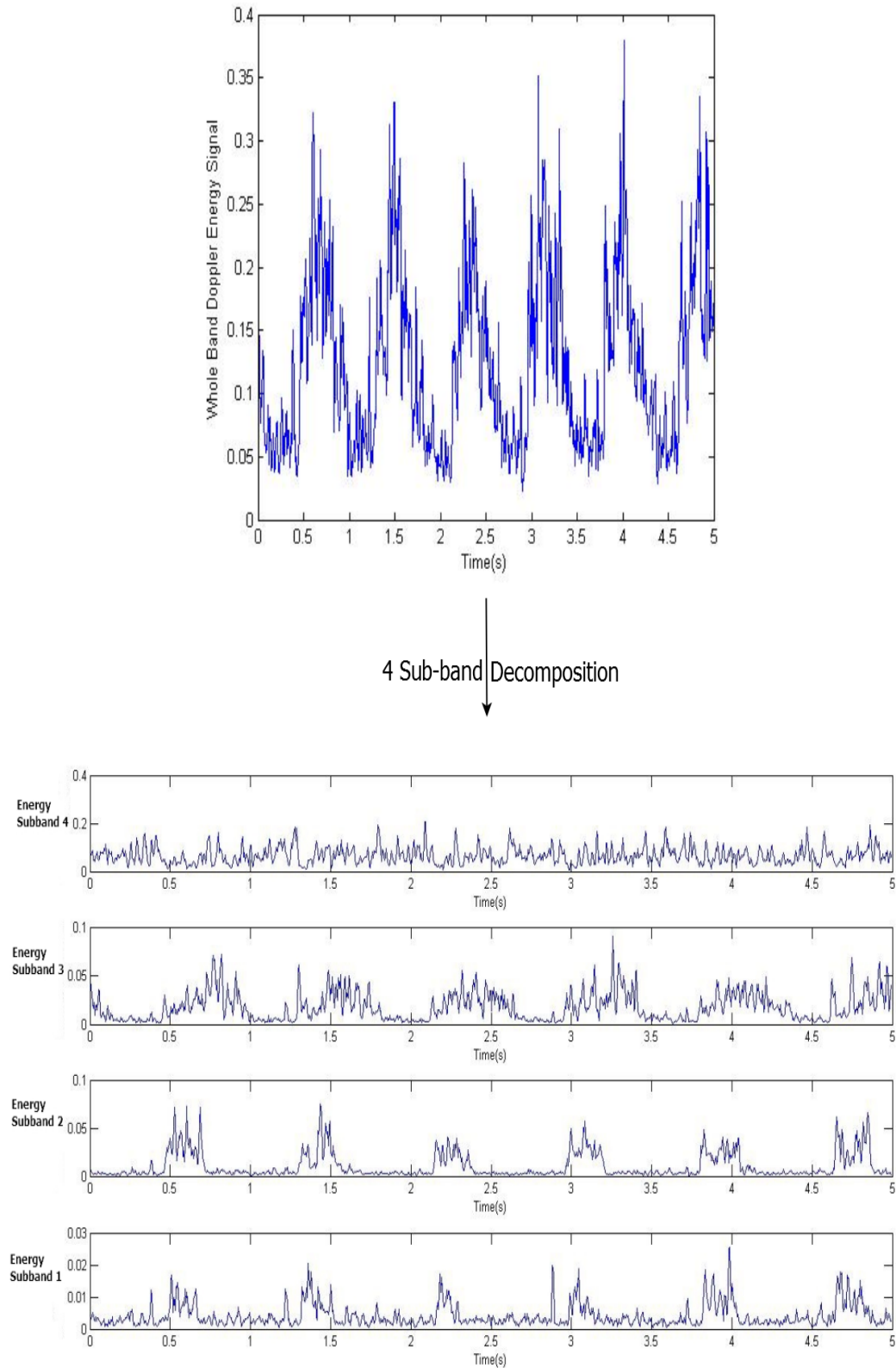


Figure 4.5: An illustration of a 5 second extracted signal segment decomposed into 4 sub-bands. The decomposition is performed through a bank of four identical-width rectangular functions.

4.2. THE MICRO-EMBOLIC SHORT TIME FOURIER TRANSFORM SUB-BAND DETECTION UNIT

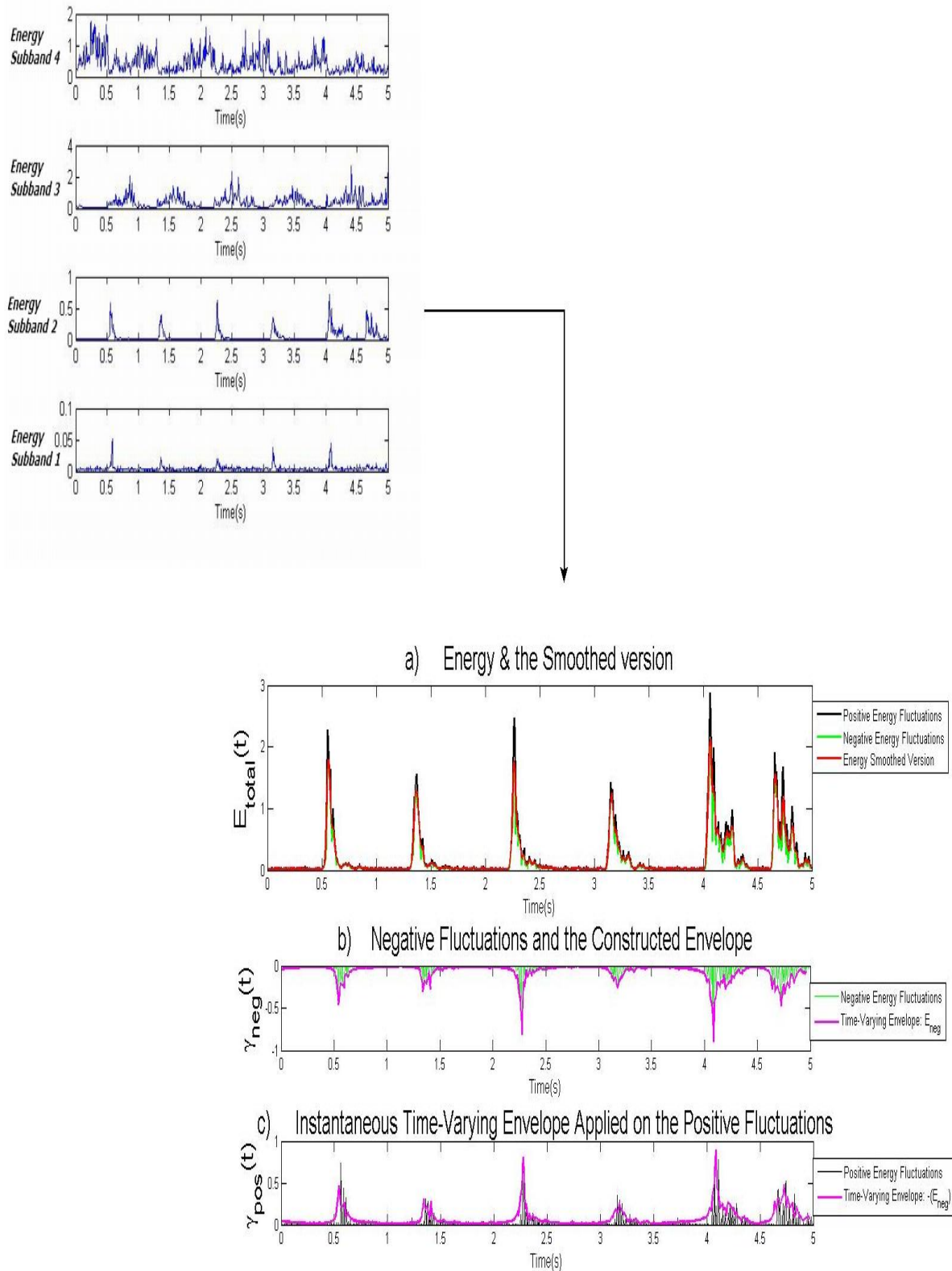


Figure 4.6: Sub-band detection process with negative energy fluctuations-based detector. Due to space complications we represent the detection process in sub-band 2 only. However, the same embolus detection process is applied in each sub-band.

The final stage (Part 4 in Fig. 4.4) in the sub-band detection process before counting the final detections, is merging of all detections achieved in each sub-band. An important point here is to accompany the merging with a test that continuously verifies that the micro-embolic signature detected in sub-band n is not detected at the same instant or at the same time interval in all the preceding and following sub-bands. In other terms, the latter test assures that the same embolus detected in more than one sub-band is counted only once in the final detection. The time interval we apply ranges $\pm 0.025s$ around the detected micro-embolus peak. This is because the positions of micro-emboli detected in different sub-bands are not always exactly the same and may slightly vary from one sub-band to another as can be seen in Figure 4.7. After an experimental procedure we applied on same emboli detected in more than one sub-band the maximum difference in sub-band positions is 0.025 s. Figure 4.7 shows three cases. In the first two cases presented in Figure 4.7 a) 2 micro-emboli appear in two different sub-bands at the exact same position and in the second case in Figure 4.7 b) the same micro-embolus appears in three different sub-bands in a time difference of 0.01 s between the micro-embolus detected in the second and third sub-band and 0.02 s between that detected in the second and fourth sub-band. The time interval we apply assures the micro-embolus is recorded only once in the final detection.

4.3. RESULTS

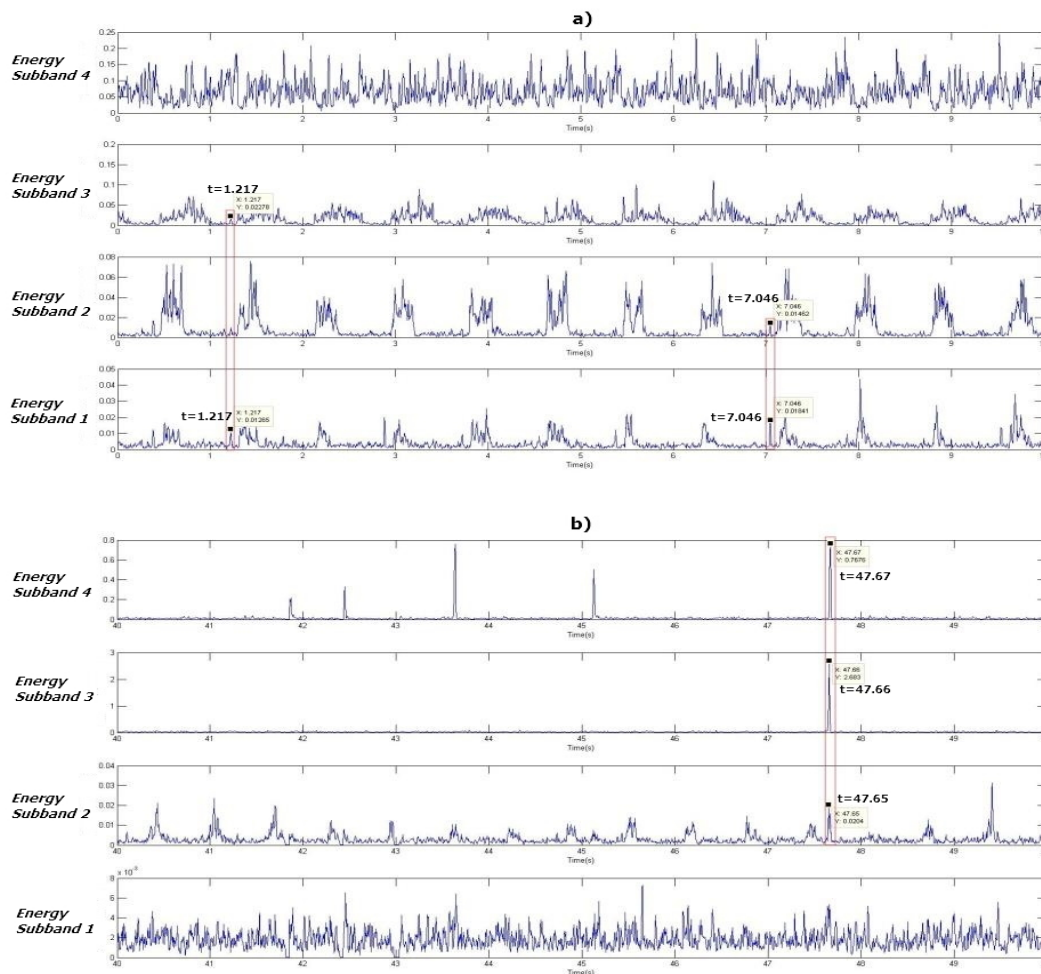


Figure 4.7: a) An illustration of 2 micro-emboli that appear in two different sub-bands. The first micro-embolus appears in sub-bands one and three at the exact same position (1.217 s) and the second micro-embolus appears in the first and second sub-band at the same exact position (7.046 s). In both cases, when the micro-embolus is first detected in a sub-band, the time interval ± 0.025 s around the peak is applied on the following sub-bands to prevent the micro-embolus from being recorded again. This assures that the same micro-embolus is recorded only once in the final decision. b) An illustration of a micro-embolus that appears three times in three different sub-bands but at slightly different time positions. When the micro-embolus is first detected in the second sub-band, a time interval ± 0.025 s around the peak is applied on the following sub-bands to prevent the micro-embolus from being recorded again. This assures that the same micro-embolus is recorded only once in the final decision.

4.3 Results

As in the previous chapter, the database, composed of 25 signals, is divided into two categories. The first category includes 10 signals dedicated to achieve the training phase. The training phase allows adjusting the best threshold values in each sub-band as well as the optimal number

of sub-bands to be used through maximizing the detection rate and minimizing the false alarm rate. The second category comprised 15 signals on which the experimentation methods are tested and results are obtained.

The results are divided into five parts. In the first three parts we present the results of the training phase for sub-band detection with constant empirical thresholds, sub-band detection with constant statistical thresholds and sub-band detection with the use of the negative energy fluctuations-based time-varying threshold. In the fourth part, we present the testing phase results for the three sub-band detectors. In the last part, we compare sub-band detection to whole band detection.

4.3.1 Sub-band detection with constant empirical thresholds

In this section, we present the results when sub-band detection is performed with constant empirical thresholds employed in each sub-band.

First, we apply a training phase to determine the optimal thresholds to be used in each sub-band. 2, 4 and 8 sub-bands are tested. Thresholds ranging between 3 dB and 9 dB are simultaneously tested in each sub-band and the best set of thresholds is determined according to the detection rates and false alarm rates achieved. Due to the large number of decibel thresholds tested we will present only the best results obtained.

For 2 sub-bands used the best results obtained are those when a 4 dB empirical threshold is used in each sub-band. The results are presented in Table 4.1. The detection rate achieved is 65 % and the false alarm rate is 43 %.

Table 4.1: Results (Detection Rate and False Alarm Rate) for 2 sub-band decomposition with a 4 dB constant empirical threshold used in each sub-band.

2 Sub-band Decomposition	Best Empirical Threshold (dB)	Detection Rate (%)	False Alarm Rate (%)
First Sub-band	4 dB	-	-
Second Sub-band	4 dB	-	-
Final Detection	-	65 %	43 %

For 4 sub-bands used the best results obtained are those when a 4 dB empirical threshold is used in each sub-band. The results are presented in Table 4.2. The detection rate achieved is 79 % and the false alarm rate is 41 %.

4.3. RESULTS

Table 4.2: Results (Detection Rate and False Alarm Rate) for 4 sub-band decomposition with a 4 dB constant empirical threshold used in each sub-band.

4 Sub-band Decomposition	Best Empirical Threshold (dB)	Detection Rate (%)	False Alarm Rate (%)
First Sub-band	4 dB	-	-
Second Sub-band	4 dB	-	-
Third Sub-band	4 dB	-	-
Fourth Sub-band	4 dB	-	-
Final Detection	-	79 %	41 %

For 8 sub-bands used the best results obtained are those when a 3 dB empirical threshold is used in each sub-band. The results are presented in Table 4.3. The detection rate achieved is 80 % and the false alarm rate is 45 %.

Finally, by comparing the detection rates and false alarm rates obtained by testing 2,4 and 8 sub-bands in the training phase, we can state that 4 sub-bands provide the best trade-off between the different rates. By looking at the results in Table 4.1, 4.2, and 4.3, compared to 2 sub-bands, 4 sub-bands allow a better DR and a lower FAR. Compared to 8 sub-bands, 4 sub-bands allow a close DR and a lower FAR with a logically less computational time (or processing speed).

Therefore, after the training phase result we tend to use in the testing phase a 4 sub-band detector with a 4 dB constant empirical threshold in each sub-band. The results of this testing phase are presented in Figure 4.8 in section 4.3.4.

Table 4.3: Results (Detection Rate and False Alarm Rate) for 8 sub-band decomposition with a 3 dB constant empirical threshold used in each sub-band.

8 Sub-band Decomposition	Best Empirical Threshold (dB)	Detection Rate (%)	False Alarm Rate (%)
First Sub-band	3 dB	-	-
Second Sub-band	3 dB	-	-
Third Sub-band	3 dB	-	-
Fourth Sub-band	3 dB	-	-
Fifth Sub-band	3 dB	-	-
Sixth Sub-band	3 dB	-	-
Seventh Sub-band	3 dB	-	-
Eighth Sub-band	3 dB	-	-
Final Detection	-	80 %	45 %

4.3.2 Sub-band detection with constant statistical thresholds

In this section, we present the results when sub-band detection is performed with constant statistical thresholds $\lambda = \mu + m\sigma$ used in each sub-band.

First, we apply a training phase to determine the optimal thresholds to be used in each sub-band. 2, 4 and 8 sub-bands are tested. Thresholds ranging between $\lambda = \mu + 3\sigma$ and $\lambda = \mu + 6\sigma$ are simultaneously tested in each sub-band and the best set of thresholds is determined according to the detection rates and false alarm rates achieved. Due to the large number of m values tested we will present only the best results obtained.

For 2 sub-bands used the best results obtained are those when a $\lambda = \mu + 5\sigma$ statistical threshold is used in each sub-band. The results are presented in Table 4.4. The detection rate achieved is 72 % and the false alarm rate is 32 %.

Table 4.4: Results (Detection Rate and False Alarm Rate) for 2 sub-band decomposition with a $\lambda = \mu + 5\sigma$ constant statistical threshold used in each sub-band.

2 Sub-band Decomposition	Best Statistical Threshold	Detection Rate (%)	False Alarm Rate (%)
First Sub-band	$\lambda = \mu + 5\sigma$	-	-
Second Sub-band	$\lambda = \mu + 5\sigma$	-	-
Final Detection	-	72 %	32 %

For 4 sub-bands used the best results obtained are those when a $\lambda = \mu + 4.5\sigma$ statistical threshold is used in each sub-band. The results are presented in Table 4.5. The detection rate achieved is 82 % and the false alarm rate is 28 %.

Table 4.5: Results (Detection Rate and False Alarm Rate) for 4 sub-band decomposition with a $\lambda = \mu + 4.5\sigma$ constant statistical threshold used in each sub-band.

4 Sub-band Decomposition	Best Statistical Threshold	Detection Rate (%)	False Alarm Rate (%)
First Sub-band	$\lambda = \mu + 4.5\sigma$	-	-
Second Sub-band	$\lambda = \mu + 4.5\sigma$	-	-
Third Sub-band	$\lambda = \mu + 4.5\sigma$	-	-
Fourth Sub-band	$\lambda = \mu + 4.5\sigma$	-	-
Final Detection	-	82 %	28 %

For 8 sub-bands used the best results obtained are those when a $\lambda = \mu + 4\sigma$ statistical threshold is used in each sub-band. The results are presented in Table 4.6. The detection rate achieved is 84 % and the false alarm rate is 30 %.

Finally, by comparing the detection rates and false alarm rates obtained by testing 2,4 and 8 sub-bands in the training phase, we can state that 4 sub-bands provide the best trade-off between the different rates. By looking at the results in Table 4.4, 4.5, and 4.6, compared to 2 sub-bands,

4.3. RESULTS

4 sub-bands allow a better DR and a lower FAR. Compared to 8 sub-bands, 4 sub-bands allow a close DR and a lower FAR with a logically less computational time (or processing speed).

Table 4.6: Results (Detection Rate and False Alarm Rate) for 8 sub-band decomposition with a $\lambda = \mu + 4\sigma$ constant statistical threshold used in each sub-band.

8 Sub-band Decomposition	Best Statistical Threshold	Detection Rate (%)	False Alarm Rate (%)
First Sub-band	$\lambda = \mu + 4\sigma$	-	-
Second Sub-band	$\lambda = \mu + 4\sigma$	-	-
Third Sub-band	$\lambda = \mu + 4\sigma$	-	-
Fourth Sub-band	$\lambda = \mu + 4\sigma$	-	-
Fifth Sub-band	$\lambda = \mu + 4\sigma$	-	-
Sixth Sub-band	$\lambda = \mu + 4\sigma$	-	-
Seventh Sub-band	$\lambda = \mu + 4\sigma$	-	-
Eighth Sub-band	$\lambda = \mu + 4\sigma$	-	-
Final Detection	-	84 %	30 %

Therefore, after the training phase result we tend to use in the testing phase a 4 sub-band detector with a $\lambda = \mu + 4.5\sigma$ constant statistical threshold in each sub-band. The results of this testing phase are presented later in Figure 4.8.

4.3.3 Sub-band detection with negative energy fluctuations-based time-varying threshold

In this section, we present the results when sub-band detection is performed under the negative energy fluctuations-based detection technique with a time-varying threshold $\lambda(t) = \mu(t) + m\sigma(t)$ used in each sub-band.

First, we apply a training phase to determine the optimal thresholds to be used in each sub-band. 2, 4 and 8 sub-bands are tested. Thresholds ranging between $\lambda(t) = \mu(t) + 3\sigma(t)$ and $\lambda(t) = \mu(t) + 7\sigma(t)$ are simultaneously tested in each sub-band and the best set of thresholds is determined according to the detection rates and false alarm rates achieved. Due to the large number of m values tested we will present only the best results obtained.

For 2 sub-bands used the best results obtained are those when a $\lambda(t) = \mu(t) + 6\sigma(t)$ threshold is used in each sub-band. The results are presented in Table 4.7. The detection rate achieved is 75 % and the false alarm rate is 24 %.

CHAPTER 4. COUPLING OF A NEGATIVE ENERGY FLUCTUATIONS-BASED
DETECTOR WITH SUB-BAND DECOMPOSITION: A HIGHLY PERFORMING
EMBOLUS DETECTION TECHNIQUE

Table 4.7: Results (Detection Rate and False Alarm Rate) for 2 sub-band decomposition with a $\lambda(t) = \mu(t) + 6\sigma(t)$ time-varying threshold used in each sub-band.

2 Sub-band Decomposition	Best Time-Varying Threshold	Detection Rate (%)	False Alarm Rate (%)
First Sub-band	$\lambda(t) = \mu(t) + 6\sigma(t)$	-	-
Second Sub-band	$\lambda(t) = \mu(t) + 6\sigma(t)$	-	-
Final Detection	-	75 %	24 %

For 4 sub-bands used the best results obtained are those when a $\lambda(t) = \mu(t) + 5.5\sigma(t)$ threshold is used in each sub-band. The results are presented in Table 4.8. The detection rate achieved is 96 % and the false alarm rate is 10 %.

Table 4.8: Results (Detection Rate and False Alarm Rate) for 4 sub-band decomposition with $\lambda(t) = \mu(t) + 5.5\sigma(t)$ time-varying threshold used in each sub-band.

4 Sub-band Decomposition	Best Time-Varying Threshold	Detection Rate (%)	False Alarm Rate (%)
First Sub-band	$\lambda(t) = \mu(t) + 5.5\sigma(t)$	-	-
Second Sub-band	$\lambda(t) = \mu(t) + 5.5\sigma(t)$	-	-
Third Sub-band	$\lambda(t) = \mu(t) + 5.5\sigma(t)$	-	-
Fourth Sub-band	$\lambda(t) = \mu(t) + 5.5\sigma(t)$	-	-
Final Detection	-	96 %	10 %

For 8 sub-bands used the best results obtained are those when a $\lambda(t) = \mu(t) + 3\sigma(t)$ threshold is used in each sub-band. The results are presented in Table 4.9. The detection rate achieved is 98 % and the false alarm rate is 15 %.

Finally, by comparing the detection rates and false alarm rates obtained by testing 2,4 and 8 sub-bands in the training phase, we can state that 4 sub-bands provide the best trade-off between the different rates. By looking at the results in Table 4.7, 4.8, and 4.9, compared to 2 sub-bands, 4 sub-bands allow a better DR and a lower FAR. Compared to 8 sub-bands, 4 sub-bands allow a close DR and a much lower FAR with a logically less computational time (or processing speed).

4.3. RESULTS

Table 4.9: Results (Detection Rate and False Alarm Rate) for 8 sub-band decomposition with a $\lambda(t) = \mu(t) + 3\sigma(t)$ time-varying threshold used in each sub-band.

8 Sub-band Decomposition	Best Time-Varying Threshold	Detection Rate (%)	False Alarm Rate (%)
First Sub-band	$\lambda(t) = \mu(t) + 3\sigma(t)$	-	-
Second Sub-band	$\lambda(t) = \mu(t) + 3\sigma(t)$	-	-
Third Sub-band	$\lambda(t) = \mu(t) + 3\sigma(t)$	-	-
Fourth Sub-band	$\lambda(t) = \mu(t) + 3\sigma(t)$	-	-
Fifth Sub-band	$\lambda(t) = \mu(t) + 3\sigma(t)$	-	-
Sixth Sub-band	$\lambda(t) = \mu(t) + 3\sigma(t)$	-	-
Seventh Sub-band	$\lambda(t) = \mu(t) + 3\sigma(t)$	-	-
Eighth Sub-band	$\lambda(t) = \mu(t) + 3\sigma(t)$	-	-
Final Detection	-	98 %	15 %

Therefore, after the training phase result we tend to use in the testing phase a 4 sub-band detector with a $\lambda(t) = \mu(t) + 5.5\sigma(t)$ negative energy fluctuations-based time-varying threshold in each sub-band. The results of this testing phase are presented in Figure 4.8.

4.3.4 Results of the testing phase for the different sub-band detectors

In Figure 4.8 we present the results of the testing phase of the 4 sub-band detector with a 4 dB constant empirical threshold, the 4 sub-band detector with $\lambda = \mu + 4.5\sigma$ constant statistical threshold and the 4 sub-band detector with negative energy fluctuations-based time-varying threshold $\lambda(t) = \mu(t) + 5.5\sigma(t)$.

For the 4 sub-band detector with constant empirical thresholds, the FAR is 37 %, and the detection rate is 79 %. For the 4 sub-band detector with constant statistical thresholds, the FAR is 24 %, and the detection rate is 81 %. For the 4 sub-band detector with negative energy fluctuations-based time-varying threshold the FAR is 4 % and the detection rate is 97 %.

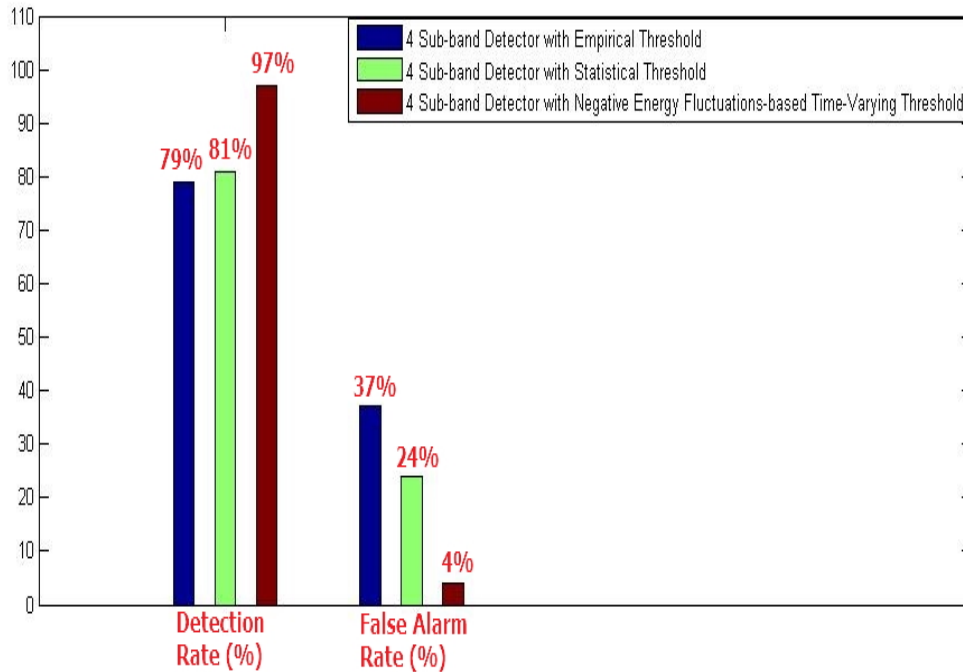


Figure 4.8: A comparison of the testing phase result of the 3 different sub-band detectors; those coupled with constant empirical thresholds, those with constant statistical thresholds and those with time-varying thresholds.

The results presented, show that the 4 sub-band detector with negative energy fluctuations-based time-varying threshold is the most performing among all sub-band detectors. It is able to reduce the FAR by more than half of the values obtained with 4 sub-band detectors with constant thresholds. Moreover, The detection rate achieved is increased by around 20 %. Thus, the superiority of the 4 sub-band detector with negative energy fluctuations-based time-varying threshold compared to the other 4 sub-band detectors is conspicuous.

4.4 The relative intensity increase of the smallest detectable micro-embolus

In an aim to discover the characteristic embolus relative intensity increase that latter presented detectors are capable of detecting we choose a sample of 175 embolic events having intensity increases below 15 dB. For each detector we evaluate the embolic events that it is capable of detecting and we discover out of these detections the embolus with the smallest relative intensity increase. The results are presented in Figure 4.9.

As can be depicted in the figure, the detection using constant empirical thresholds combined with sub-band decomposition stops at embolic signals having intensity increases below 2.6 dB. The detection based on statistical constant thresholds combined with sub-band decomposition stops at embolic signals having intensity increases below 2.3 dB. The negative energy fluctuations-based energy detector coupled with sub-band decomposition is capable of detecting micro-embolic signatures with relative intensity increases as low as 0.55 dB.

4.4. THE RELATIVE INTENSITY INCREASE OF THE SMALLEST DETECTABLE MICRO-EMBOLUS

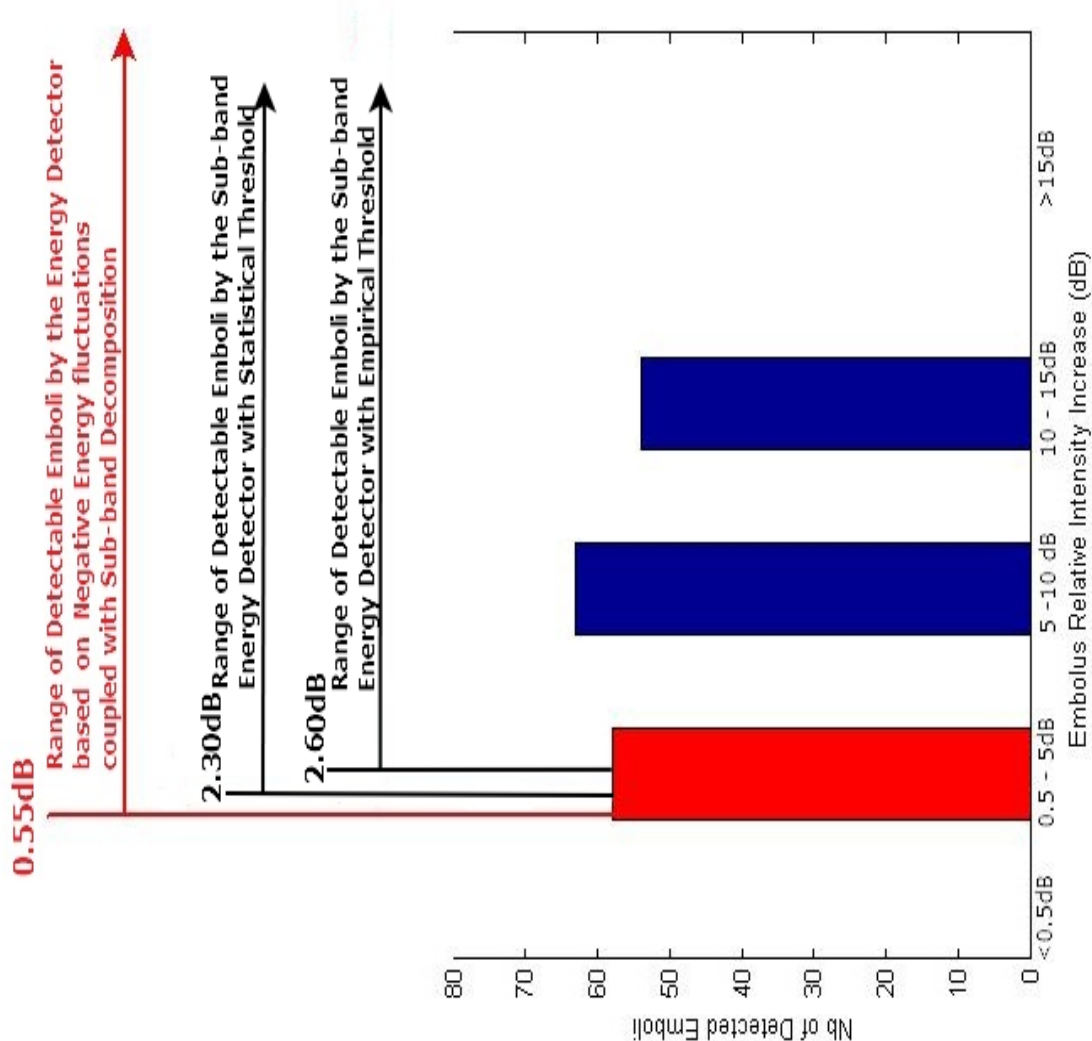


Figure 4.9: Embolus Intensity Increases relative to background blood energy for a sample of 175 chosen embolic events. The smallest detectable embolus by the sub-band detector coupled with empirical threshold is as low as 2.6 dB. The smallest detectable embolus by the sub-band detector coupled with statistical threshold is as low as 2.3 dB. The smallest detectable embolus by the sub-band detector coupled with the negative energy fluctuations based time-varying threshold is as low as 0.55 dB.

We can deduce from the latter results that the negative energy fluctuations based detector coupled with sub-band decomposition is able to detect the smallest embolic signatures with a size of $55.18 \mu\text{m}$ calculated from the 0.55 dB relative intensity increase as presented in appendix A.

Furthermore, by analyzing the results between Figures 3.10 and 4.9 we can realize that sub-band detection, compared to whole band detection, offers the possibility of detecting smaller

embolic signatures when used with any method.

To be noted that the micro-embolic size corresponding to these relative intensity increase values are provided in the appendix.

4.4.1 Sub-band detection compared to whole band detection

Although in the results above we focused on the performances of the various sub-band detectors, we have to recall that a main aim in this study is to propose sub-band decomposition as a strong tool to ameliorate micro-embolus detection compared to the detection performed in the whole Doppler frequency band.

To shed light on this point, we shall compare the results obtained with sub-band detection to that of whole band detection when the different thresholds are used.

First we compare the performance of both whole band and sub-band detectors with constant empirical thresholds used. We note that the whole band detection results were presented in the previous chapter. For simplicity and direct comparison, both results are represented in Figure 4.10. Compared to the whole band detector, the 4 sub-band detector allows increasing the detection rate by more than 13 % and reducing the FAR by more than 6 %.

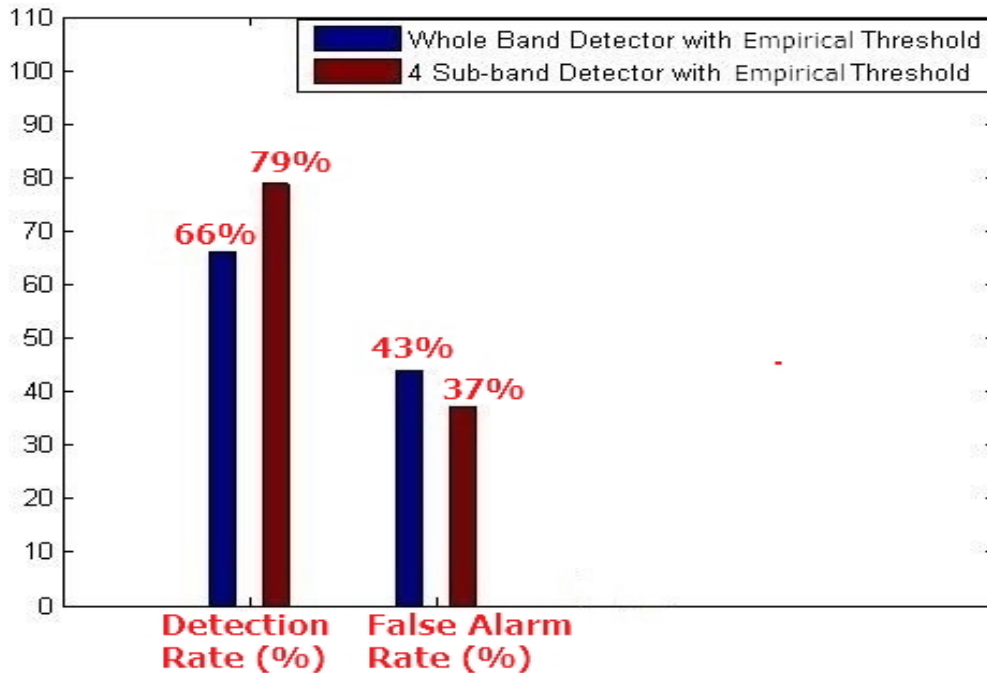


Figure 4.10: Comparison of the Detection Rate and False Alarm Rate for whole band detector and 4 sub-band detector with constant empirical thresholds.

Second we compare the performance of both whole band and sub-band detectors with constant statistical thresholds used. We note that the whole band detection results were presented in the previous chapter. For simplicity and direct comparison, both results are represented in Figure 4.11. Compared to the whole band detector, the 4 sub-band detector allows increasing the detection rate by more than 12 % and reducing the FAR by more than 17 %.

4.4. THE RELATIVE INTENSITY INCREASE OF THE SMALLEST DETECTABLE MICRO-EMBOLUS

Third we compare the performance of both whole band and sub-band detectors with negative energy fluctuations-based time-varying threshold detection used. We note that the whole band detection results were presented in the previous chapter. For simplicity and direct comparison, both results are represented in Figure 4.12. Compared to the whole band detector, the 4 sub-band detector allows increasing the detection rate by more than 8 % and reducing the FAR by more than 10 %.

As expected, in all cases, sub-band detection produces better results than whole band detection.

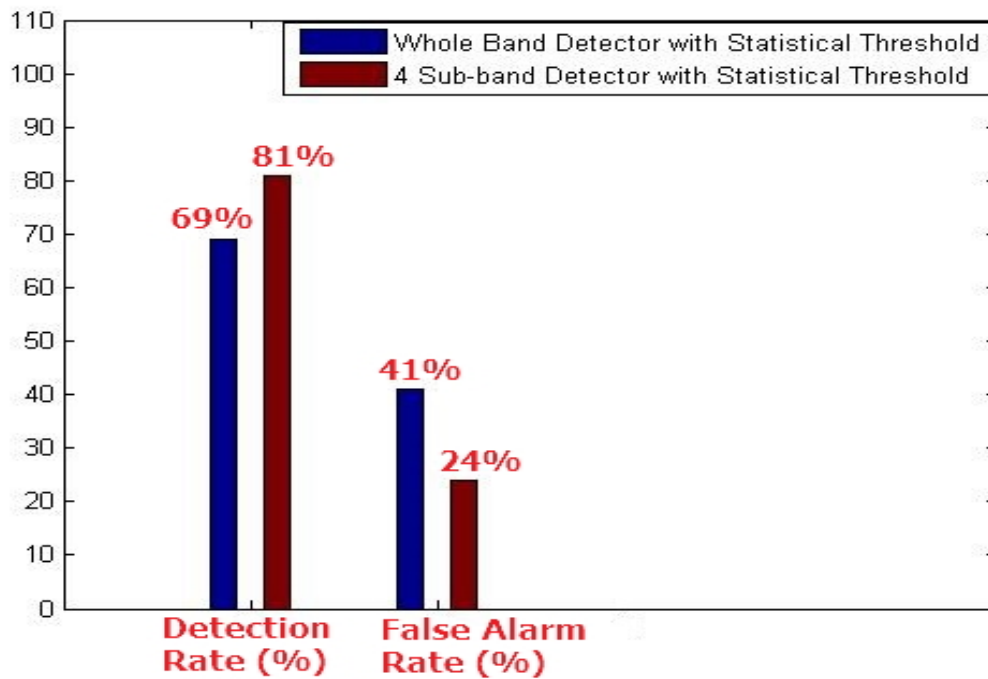


Figure 4.11: Comparison of the Detection Rate and False Alarm Rate for whole band detector and 4 sub-band detector with constant statistical thresholds.

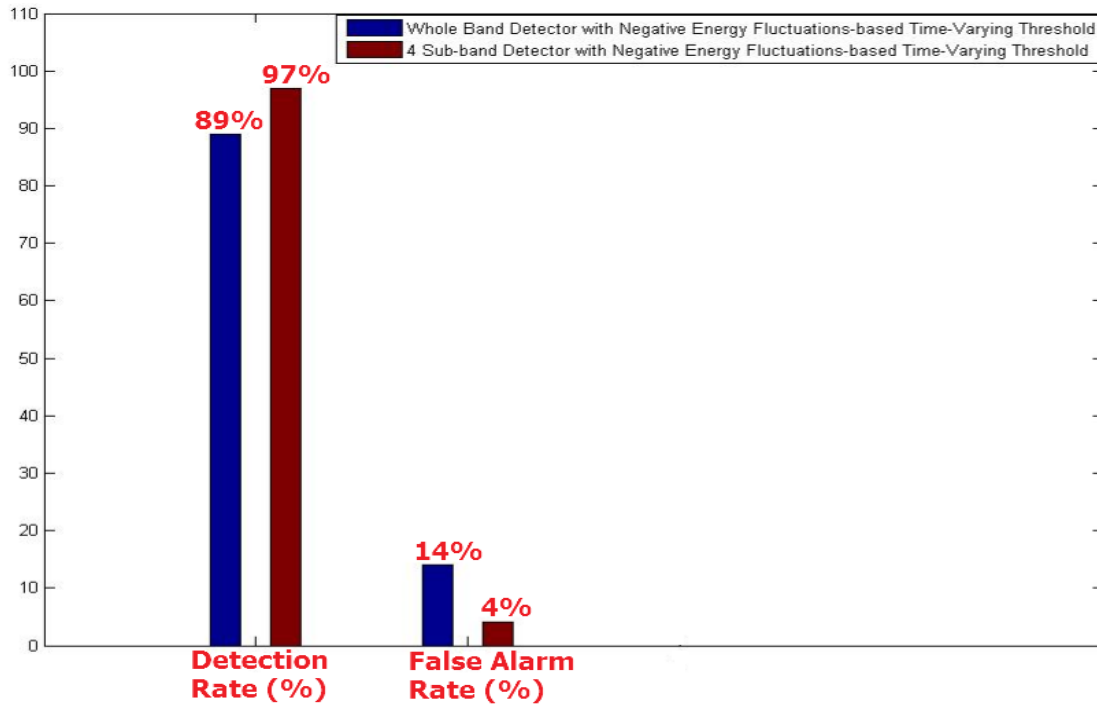


Figure 4.12: Comparison of the Detection Rate and False Alarm Rate for whole band detector and 4 sub-band detector with negative energy fluctuations-based time-varying threshold.

On another hand, as stated in the introduction of this chapter, a main purpose behind introducing sub-band decomposition is reducing the number of red blood cells contributing in the background Doppler signal and thus amplifying the contrast between the micro-embolic signature and the background Doppler signal. One parameter to measure this contrast amplification and prove the latter hypothesis is the embolus relative intensity increase presented in chapter 2.

In the survey we present here, we have chosen a set of 50 embolic events recorded in the gold standard. For each embolic event we calculate the corresponding intensity increase relative to the background signal in both the whole Doppler band and in the 4 sub-band decomposition. The mean relative intensity increase for the 50 embolic events achieved in both types of bands are presented in Figure 4.13. Through this figure, we can verify that by using sub-band decomposition the relative intensity increase of emboli is hugely augmented compared to whole band detection. The increase is more than 6 dB.

4.4. THE RELATIVE INTENSITY INCREASE OF THE SMALLEST DETECTABLE MICRO-EMBOLUS

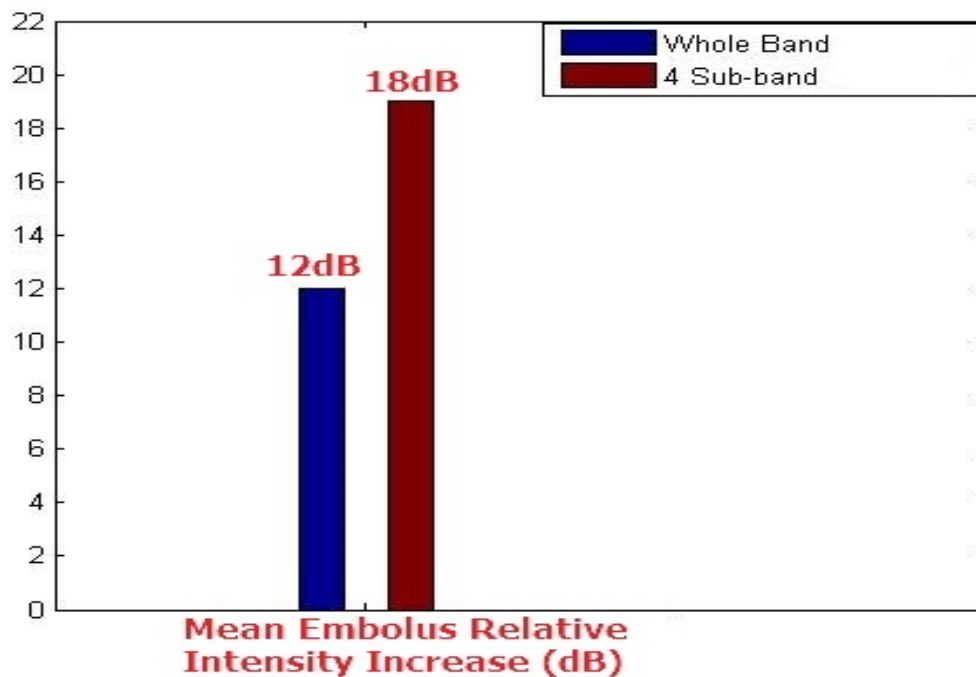


Figure 4.13: Comparison of the mean relative intensity increase for the 50 embolic signals calculated in both the whole band and the 4-sub-band.

As a result of this augmentation induced by sub-band decomposition, the detectability of micro-embolus is boosted. For instance, even when using constant empirical thresholds of detection that were proven unreliable for micro-embolus detection the sub-band decomposition makes detecting some of these micro-emboli possible. An illustration is given in Figure 4.14.

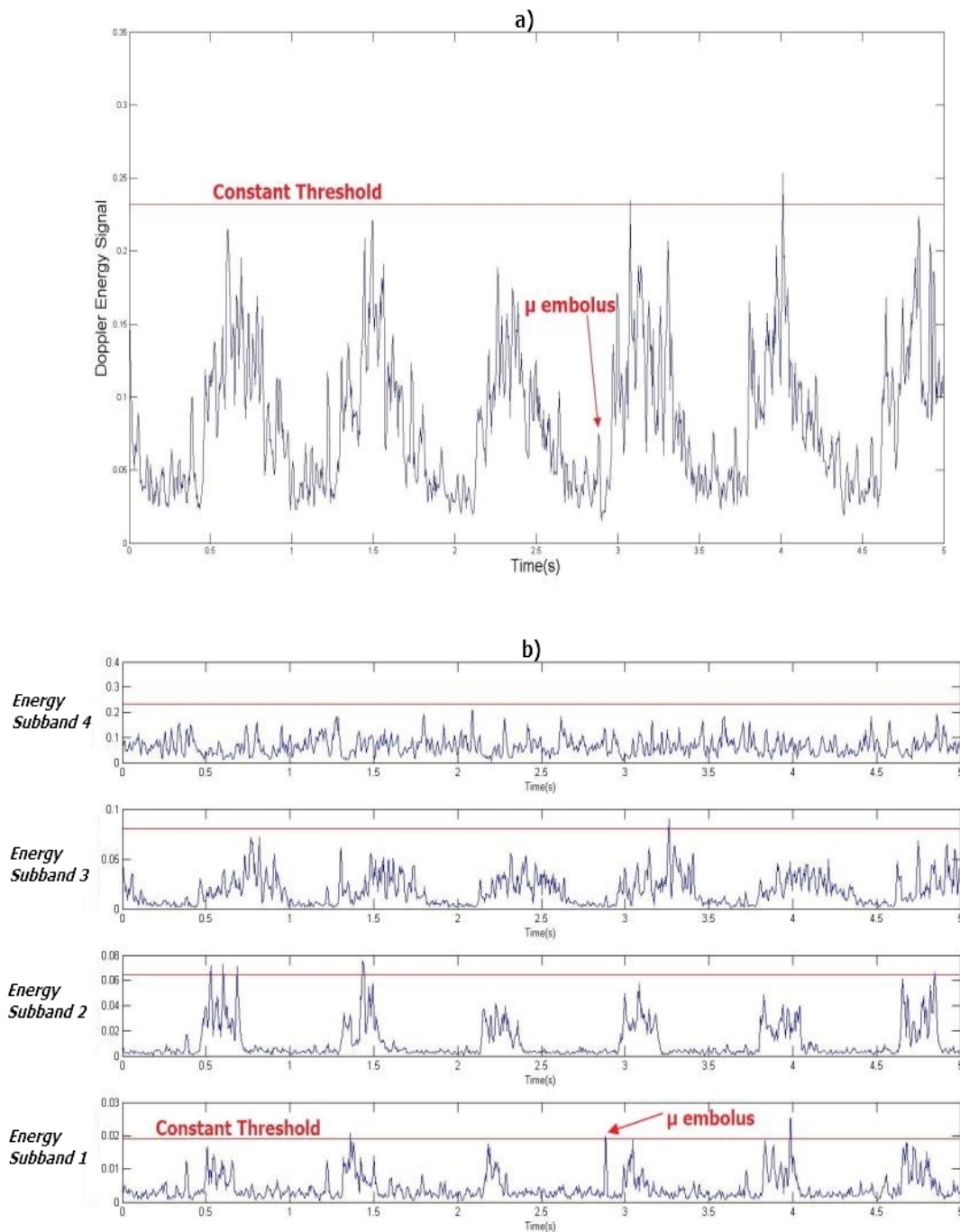


Figure 4.14: a) A micro-embolus signature cannot be detected in the whole band Doppler signal upon setting a suitable constant empirical threshold. b) By applying sub-band decomposition and setting the suitable empirical threshold in each sub-band, the same micro-embolus signature is well detected in the first sub-band.

4.5 Sub-band Decomposition achieved through Wavelet Packet Decomposition

In the previous sections, we have introduced the detection process and the results of the Short Time Fourier Transform sub-band decomposition. In the current section, we will present another method we have tested to apply sub-band decomposition which is the Wavelet Packet Decomposition (WPD).

Long time ago the wavelet transform (WT) was introduced as an alternative for the Fourier transform-based detection methods. A number of researchers reported that the WT performs better than the Fourier transform for analysis and detection of embolic signals (Aydin and Markus, 1999), (Aydin et al., 1999), and (Krongold et al., 1999).

Generally, and not to open a wide discussion of the two techniques, the wavelet transform of a signal is the decomposition of this signal over a set of functions obtained after dilatation and translation of an analyzing wavelet. Unlike Fourier analysis, wavelet analysis does not use a time-frequency region, but rather a time-scale region (scale is $1/\text{frequency}$). While Fourier analysis consists of breaking up a signal into sine waves of various frequencies, wavelet analysis is the breaking up of a signal into shifted and scaled versions of the original or mother wavelet. This mother wavelet belongs to a certain family of wavelets such as the Daubechies, Haar, Meyer and Morlet families.

The wavelet transform is supposed to be very suitable for the detection of emboli because wavelets are similar to the unpredictable embolic signals. They are irregular, asymmetric and not periodic. Moreover, WT produces a variable time-frequency resolution over the time-frequency plane by providing good time resolution at high frequencies and good frequency resolution at low frequencies. In contrast to the STFT which uses a single analysis window, WT allows a windowing technique with variable-sized regions. It allows the use of long time intervals (long windows) where more precise low-frequency information is needed and short windows where high-frequency information is needed.

Continuous wavelet transform [(Krongold et al., 1999), (Aydin and Markus, 1999), (Aydin et al., 1999), (Ng et al., 2008), (Gonçalves et al., 2011), (Ferroudji et al., 2012), (Gonçalves et al., 2013)] discrete wavelet transform [(Aydin et al., 2001), (Aydin et al., 2004), (Aydin, 2007)] the dual tree complex wavelet transform [Serbes et al. (2014), (Serbes et al., 2015)] and the wavelet packet decomposition [(Girault et al., 2007), (Chen and Wang, 2008), (Girault, 2013), (Lueang-on et al., 2013)] were all used for micro-embolus detection. All different types of wavelets proposed in the different studies were proven to be powerful in micro-embolus detection.

In our study here, we proposed the wavelet packet decomposition (WPD) as another significant sub-band decomposition tool to improve micro-embolus detection. The aim behind this is to assess the effect of using wavelets on our set of signals and detectors and also to compare the results of the WPD to the STFT sub-band decomposition for the different detectors.

4.5.1 The wavelet packet decomposition calculation

The wavelet packet decomposition detection procedure is similar to that achieved by STFT sub-band decomposition given in Figure 4.4 with the only difference being the absence of

FFT calculation. Rather, the wavelet packet decomposition decomposes the extracted Doppler sequence into a number of n ideal equal-width sub-bands denoted as nodes in the wavelet packet decomposition tree shown in Figure 4.15. j denotes the decomposition level. At each decomposition level j , the frequency axis is divided into 2^j sub-bands.

To detail the process in Figure 4.15, the WPD decomposes the signal into approximation ($W_{1,0}$) and details ($W_{1,1}$). The approximations are the high-scale, low-frequency components of the signal. The details are the low-scale, high-frequency components. To get the approximation and detail signals, the Doppler signal, $x(t)$ passes through two filters, low pass and high pass, and emerges as two signals. Then down sampling is applied to get from the latter 2 signals, 2 sequences called approximation and detail coefficients having each half the number of samples as $x(t)$. Next, reconstruction is performed (by up sampling and then filtering) on the coefficients in order to gain reconstructed approximations ($W_{1,0}$) and details ($W_{1,1}$). This decomposition can be iterated to obtain a multi-level decomposition (each level denoted by j). Detection of emboli is majorly based on the reconstructed signals.

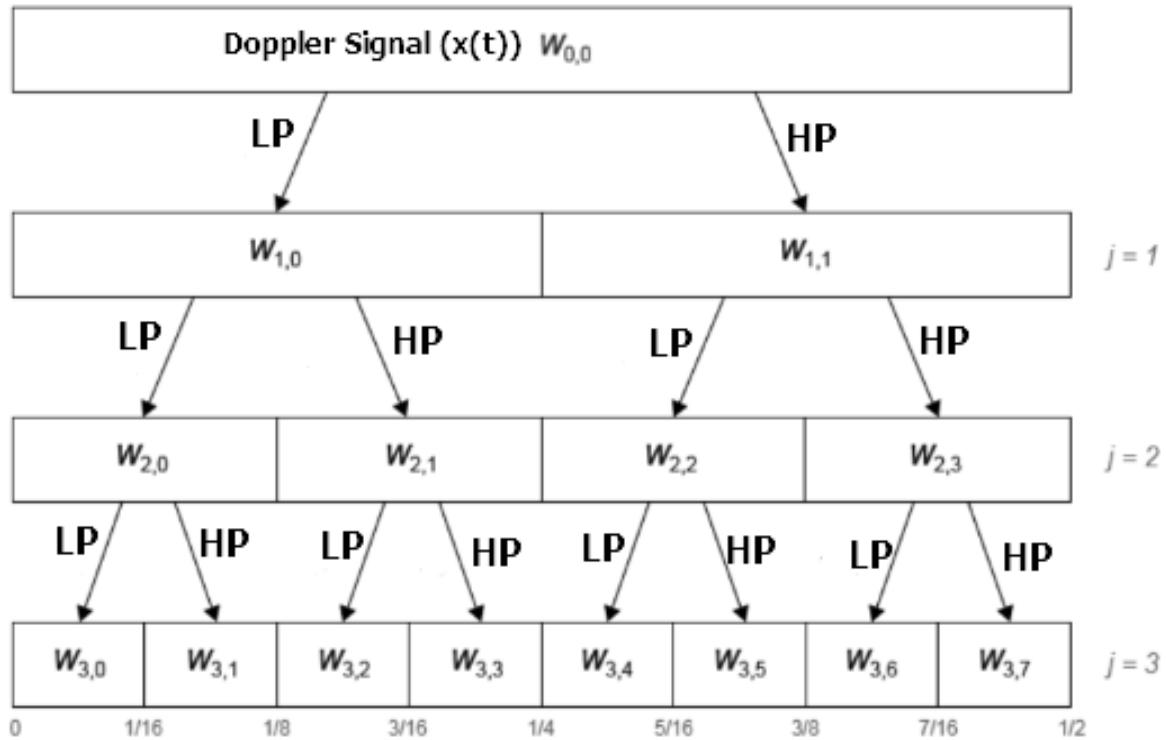


Figure 4.15: A 3rd order Wavelet Packet Tree. j denotes the decomposition level. At the 3rd decomposition, 8 different sub-band signals are obtained each denoted by a node and is correlated with an index (3,0 for example). LP denotes low pass filtering and HP high pass filtering. The third level signal $W_{3,0}$ to $W_{3,7}$ represent the frequency content of the original signal $x(t)$ within the band $0 - f_s/16$, $f_s/16 - f_s/8$, $f_s/8 - 3f_s/16$, $3f_s/16 - f_s/4$, $5f_s/16 - 3f_s/8$, $3f_s/8 - 7f_s/16$, and $7f_s/16 - f_s/2$ respectively, where f_s is the sampling frequency of the signal $x(t)$.

4.5. SUB-BAND DECOMPOSITION ACHIEVED THROUGH WAVELET PACKET DECOMPOSITION

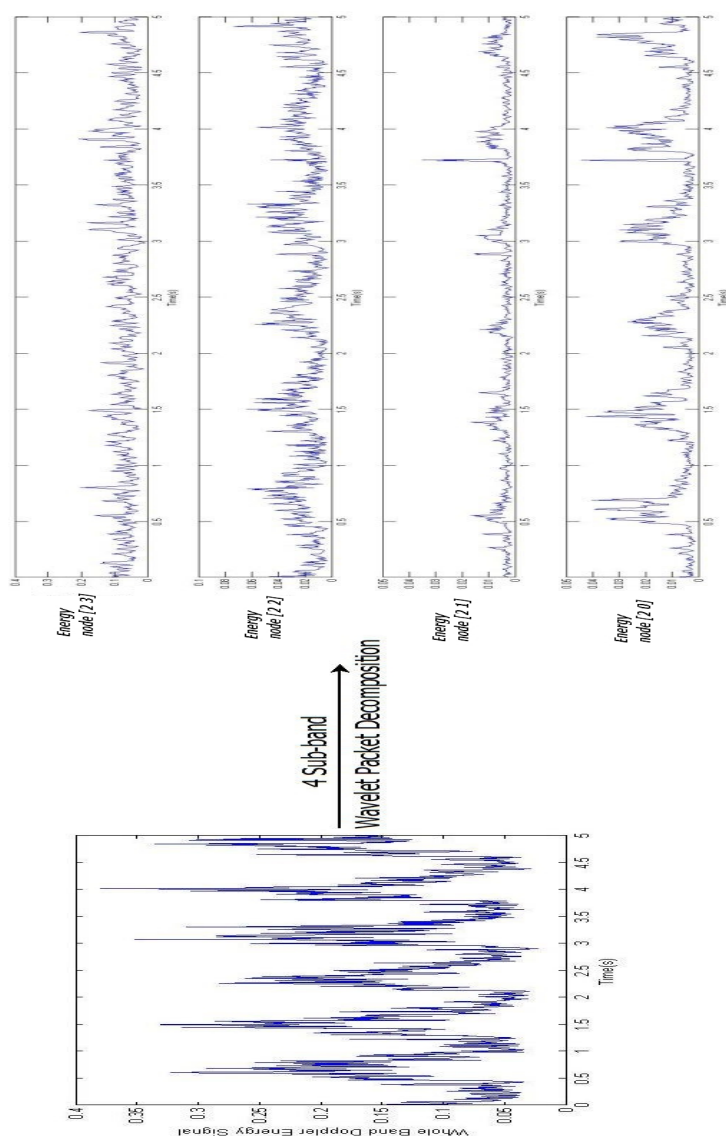


Figure 4.16: An illustration of a 5 second extracted signal segment decomposed into 4 sub-bands by the wavelet packet decomposition.

After wavelet packet decomposition, the energy in each sub-band is calculated through the following equation:

$$E_{j,k}(t) = \left| \int W_{j,k}(\tau) d\tau \right|^2 \quad \forall j \text{ and } k \in [0, 2^{j-1}] \quad (4.5)$$

where k is the position index and j is the decomposition level.

In Figure 4.16, we display the same signal used in Figure 4.5 but decomposed into 4 sub-bands by the wavelet packet decomposition. The energies in each sub-band are denoted by energy in nodes [2 0], [2 1], [2 2] and [2 3].

We note that the wavelet family used is Daubechies 5. In fact, there is no universal wavelet

function that suits all types of signals. One wavelet function giving a good performance for a database may not give the same performance for another database. Therefore, choosing the wavelet function type depends on the degree of knowledge of the signal of interest. On our set of signals, we tested the wavelets that are most extensively used in the literature which are the Daubechies 5 and 8 and also the morlet wavelet. The final choice was to use the Daubechies 5 which yielded good performances.

4.5.2 Results

In order not to repeat the same illustration as in section 4.3 the main results of the WPD detection process will be briefly and directly represented.

Training phase

A study similar to that recorded in sections 4.3.1, 4.3.2 and 4.3.3 was developed to determine the optimal number of sub-bands and optimal threshold settings for the different threshold types used. The optimal results are directly presented below.

For the wavelet packet sub-band detection with constant empirical threshold the best results are those obtained with a 4 sub-band decomposition ($j = 2$) and the threshold is set to $6dB$. The detection rate is 85 % and the false alarm rate is 23 %. The results are presented in Table 4.10.

Table 4.10: Results (Detection Rate and False Alarm Rate) for 4 sub-band wavelet packet decomposition with a 6 dB constant empirical threshold used in each sub-band.

4 Sub-band Decomposition	Best Empirical Threshold (dB)	Detection Rate (%)	False Alarm Rate (%)
First Sub-band	6 dB	-	-
Second Sub-band	6 dB	-	-
Third Sub-band	6 dB	-	-
Fourth Sub-band	6 dB	-	-
Final Detection	-	85 %	23 %

For the wavelet packet sub-band detection with constant statistical threshold the best results are those obtained with a 4 sub-band decomposition and the threshold is set to $\lambda = \mu + 5\sigma$. The detection rate is 85 % and the false alarm rate is 23 %. The results are presented in Table 4.11.

4.5. SUB-BAND DECOMPOSITION ACHIEVED THROUGH WAVELET PACKET DECOMPOSITION

Table 4.11: Results (Detection Rate and False Alarm Rate) for 4 sub-band wavelet packet decomposition with a $\lambda = \mu + 5\sigma$ constant statistical threshold used in each sub-band.

4 Sub-band Decomposition	Best Statistical Threshold	Detection Rate (%)	False Alarm Rate (%)
First Sub-band	$\lambda = \mu + 5\sigma$	-	-
Second Sub-band	$\lambda = \mu + 5\sigma$	-	-
Third Sub-band	$\lambda = \mu + 5\sigma$	-	-
Fourth Sub-band	$\lambda = \mu + 5\sigma$	-	-
Final Detection	-	85 %	23 %

For the wavelet packet sub-band detection with negative energy fluctuations-based time-varying threshold the best results are those obtained with a 4 sub-band decomposition and the threshold is set to $\lambda(t) = \mu(t) + 6\sigma(t)$. The detection rate is 99 % and the false alarm rate is 11 %. The results are presented in Table 4.12.

Table 4.12: Results (Detection Rate and False Alarm Rate) for 4 sub-band wavelet packet decomposition with $\lambda(t) = \mu(t) + 6\sigma(t)$ time-varying threshold used in each sub-band.

4 Sub-band Decomposition	Best Time-Varying Threshold	Detection Rate (%)	False Alarm Rate (%)
First Sub-band	$\lambda(t) = \mu(t) + 6\sigma(t)$	-	-
Second Sub-band	$\lambda(t) = \mu(t) + 6\sigma(t)$	-	-
Third Sub-band	$\lambda(t) = \mu(t) + 6\sigma(t)$	-	-
Fourth Sub-band	$\lambda(t) = \mu(t) + 6\sigma(t)$	-	-
Final Detection	-	99 %	11 %

Testing Phase

In Figure 4.17 we present the results of the testing phase of the wavelet packet 4 sub-band detector with constant empirical threshold, the wavelet packet 4 sub-band detector with constant statistical threshold, the the wavelet packet 4 sub-band detector with negative energy fluctuations-based time-varying threshold.

For the 4 sub-band detector with constant empirical thresholds, the FAR is 22 %, and the detection rate is 88 %. For the 4 sub-band detector with constant statistical thresholds, the FAR is 22 %, and the detection rate is 88 %. For the 4 sub-band detector with negative energy fluctuations-based time-varying threshold the FAR is 6 % and the detection rate is 99 %.

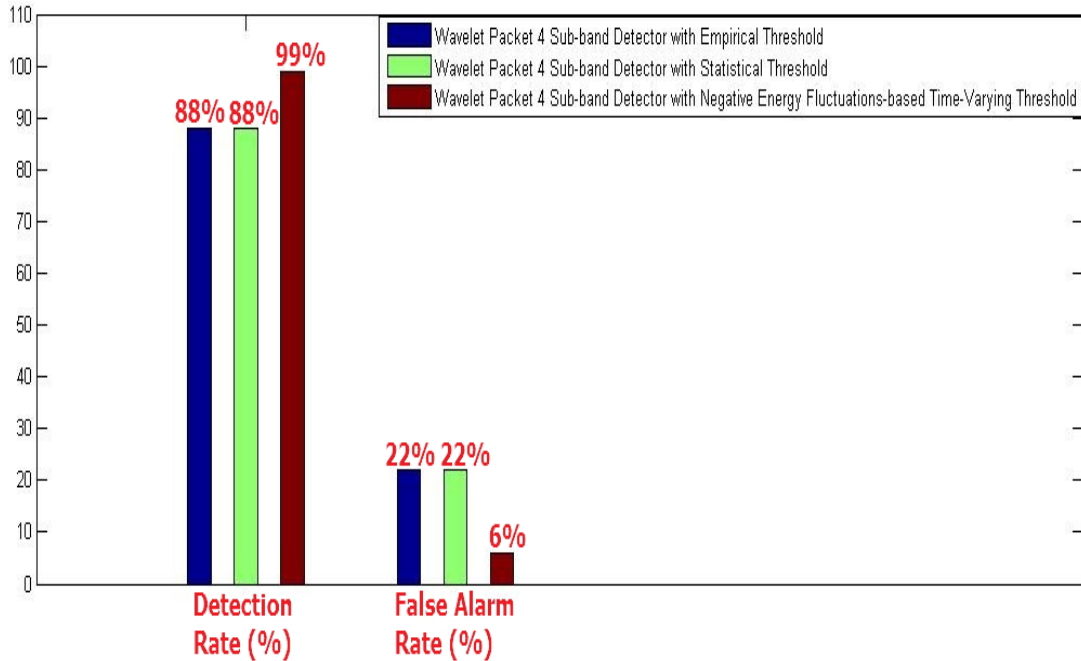


Figure 4.17: A comparison of the testing phase result of the 3 different wavelet packet sub-band detectors; those coupled with constant empirical thresholds, those with constant statistical thresholds and those with time-varying thresholds.

The results presented, show that the wavelet packet 4 sub-band detector with negative energy fluctuations-based time-varying threshold is the most performing between all wavelet packet sub-band detectors. It is able to reduce the FAR by more than half of the values obtained with 4 sub-band detectors with constant thresholds. Moreover, The detection rate achieved is increased by around 10 %. This verifies that our new negative energy fluctuations based method works best in different environments and under different techniques where the performance of constant thresholds could be boosted.

Moreover, by comparing Figure 4.17 to Figure 4.8 we conclude that using wavelet packet decomposition allows the constant thresholds to perform better. The detection rates associated with the latter detectors are increased and the false alarm rates are decreased specially that of the detector with empirical threshold. However, the results for the negative energy fluctuations-based detector were nearly the same when STFT sub-band decomposition is performed where the detection rate is increased by 1 % while the false alarm rate is 2 % higher. This verifies the stability of this detection under different conditions.

4.6 Conclusion

In this chapter, we have first introduced sub-band decomposition, through a bank of n ideal Short Time Fourier Transform frequency filters, as a powerful mechanism for micro-embolus detection. In a number of cases in which the micro-embolic signal can not be clearly distinguished from the background energy by whole band detection, it can be distinguished through

4.6. CONCLUSION

sub-band filtering. By applying decomposition of the whole Doppler spectral band into a bank of n ideal frequency bands, the concept is to reduce the number of Red Blood Cells contributing in the background Doppler signal. Hence, this allows amplification of the contrast between the micro-embolus Doppler energy and the background Doppler energy.

The sub-band detector is composed of n detectors associated to n Doppler frequency sub-bands where the detection procedure is repeated in each and every sub-band simultaneously. The final step in the sub-band detection process is merging the results from each sub-band and assuring that the same embolus detected in more than one sub-band is counted only once in the final detection.

The detection decision in each sub-band depends on the events detected above a threshold in a sub-band. Therefore, sub-band decomposition is coupled with constant and time-varying thresholds to complete the embolus detection. By coupling sub-band detection with a time-varying threshold constructed from negative energy fluctuations we introduced in the previous chapter, an extremely high performing detection system is obtained. This coupling outperforms sub-band coupling with constant thresholds and is able to detect nearly all micro-emboli with a very high detection rate reaching up to 97 % and an extremely low false alarm rate of around only 4 %.

Furthermore, we prove that sub-band decomposition offers significant improvements over whole band detection, when all different types of thresholds are used.

Consequently, we confirm that sub-band detection is a strong tool for enhancing micro-embolus detection and that a detection based on the coupling of sub-band with a time-varying threshold constructed from negative energy fluctuations, would be highly reliable and robust than all detectors specially standard commercial techniques in which detection is performed on the whole Doppler frequency band and empirical constant detection thresholds are employed.

On another term, we also introduced the same procedures but with the sub-band decomposition performed using wavelet packet decomposition. The main aim behind introducing another procedure to apply sub-band decomposition is to verify that the negative-energy based method operates in different environments and under different techniques and can work better than standard methods in different cases. We concluded that using wavelet packet decomposed sub-bands the negative-energy fluctuations based detector is able to outperform the detectors with constant thresholds, even though they showed highly improved detection and false alarm rates compared to STFT sub-band decomposition, by providing high detection rate up to 99 % and a false alarm rate of about 6 %. These results are very similar to those obtained with STFT sub-band decomposition (97 % and 4 %) which verifies the stability of this detector under different conditions.

In the upcoming chapter we will introduce new tools for micro-embolus detection based on high order statistics.

CHAPTER 4. COUPLING OF A NEGATIVE ENERGY FLUCTUATIONS-BASED
DETECTOR WITH SUB-BAND DECOMPOSITION: A HIGHLY PERFORMING
EMBOLUS DETECTION TECHNIQUE

Chapter 5

Detection of Doppler Micro-Embolic Signals using High Order Statistics

5.1 Introduction

In chapter 3, we pointed out that the probability density function was even for Doppler signal free of embolic signature (refer to equation 3.6). This also means that the probability density function is no more symmetric when micro-emboli are present in the artery. Quantifying the symmetry properties could be an interesting information to improve the detection rate of micro-embolic signatures. One interesting tool to measure the symmetrical property of a probability density function is the skewness derived of high order statistics.

In the past few years, high order statistics (HOS) have been an extensive field of research as they represent descriptive statistics that can be used to detect signal outliers and measure different signal features.

High order statistics mainly the third moment skewness and fourth moment kurtosis have been extensively used in various bio-medical signal processing fields to define, estimate and detect several signal features. In (Colantonio and Salvetti, 2007), the kurtosis was selected as one feature among many for HITS detection. In (Mühlbacher-Karrer et al., 2008), the skewness and kurtosis were used as measures of the distribution of the signal magnitude in order to estimate the severity of carotid stenosis. In (Altunkaya et al., 2010), the skewness and kurtosis were used to differentiate between normally functioning mechanical heart valve from malfunctioning heart valves due to thrombosis. In (Chua et al., 2010), the skewness and kurtosis were used for the detection of non-stationary bio-acoustic signals and as indications for detecting regions with microcalcifications. In (Gholinezhadasnefistani et al., 2015), the skewness and kurtosis were used in the analysis of neonatal ECG signals.

In this chapter we propose new types of micro-embolic detectors based on the windowed calculation of the third moment skewness and fourth moment kurtosis of the energy signal. We will show that high order statistics detection can be considered another serious candidate for micro-embolus robust detection. This work is currently submitted to the 'Computational and Mathematical Methods in Medicine' journal.

5.2 The reference offline skewness and kurtosis-based micro-embolic detection

The skewness and kurtosis based detections are represented in Figure 5.1. The steps from the SD card extraction to the instantaneous energy calculation are all described in chapter 3.

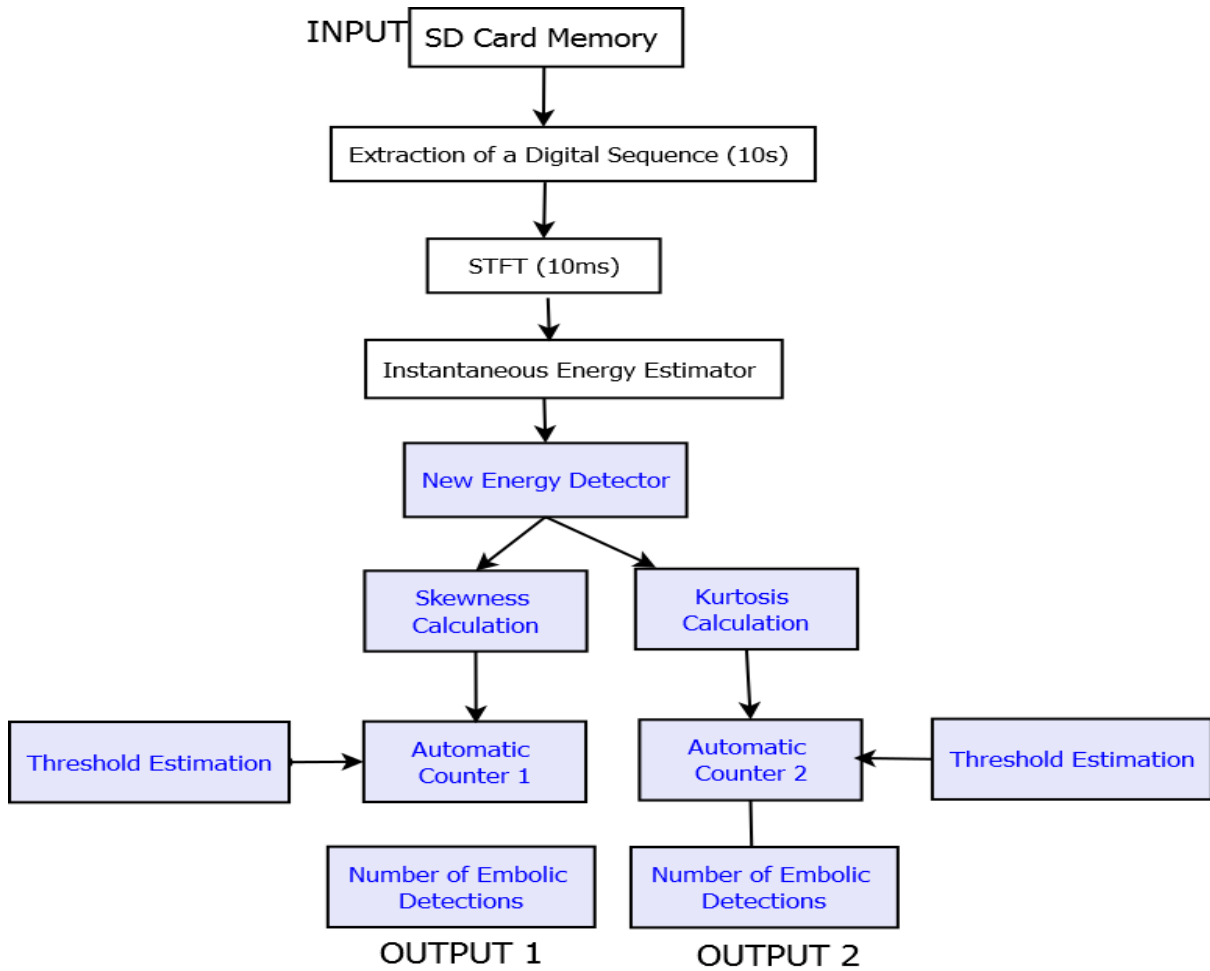


Figure 5.1: A skewness and kurtosis based embolus detection system.

The detection methods we propose are based on calculating the skewness and kurtosis from the energy signal presented in equation 2.5. The calculations are performed using a sliding window $g(t)$ where the optimal window length and overlap ratio are set during a training phase (see Results section).

The skewness is the third order standardized moment. When calculated instantaneously (by the sliding window) on the energy it is given by the following equation:

$$S(t) = \frac{ME[E(t) - \mu_E(t)]^3}{\sigma_E(t)^3}. \quad (5.1)$$

The kurtosis is the fourth order standardized moment. When calculated instantaneously on

the energy it is given by the following equation:

$$K(t) = \frac{ME[E(t) - \mu_E(t)]^4}{\sigma_E(t)^4} \quad (5.2)$$

where $\mu_E(t)$ and $\sigma_E(t)$ are the instantaneous mean and standard deviation of the energy while ME denotes the mathematical expectation value.

A micro-embolic detection based on the skewness and kurtosis signals is represented in Figure 5.2 b) and c). In Figure 5.2 a) we represent the detection through empirical constant thresholds discussed in chapter 3.

To prove that high order statistics, the skewness and the kurtosis, are suitable candidates for micro-embolus detection, consider a Doppler signal free of micro-embolic events and assume that the statistical distribution remains unchanged whatever the time position is even if the mean $\mu_i(t)$ and the variance $\sigma_i^2(t)$ vary with time. Suppose there exists two Gaussian random variables $X(t_2) = N[\mu_1(t_2), \sigma_1(t_2)]$ and $X(t_3) = N[\mu_2(t_3), \sigma_2(t_3)]$. It can be shown for the skewness S that $S(t_2) = S[X(t_2)] = S[X(t_3)] = 0$ and for the kurtosis K that $K(t_2) = K[X(t_2)] = K[X(t_3)] = 3$. In this example the skewness and the kurtosis are stationary since $S(t) = 0$ and $K(t) = 3$ for all t. This outcome can be verified whatever the distribution form while it remains unchanged over all time values. The only change occurs in the value of the skewness and the kurtosis but not in their stationarity. Consequently, when a micro-embolic event occurs at a time position t_1 , the distribution changes. The direct consequence is $S(t_1) \neq S(t_2)$ and $K(t_1) \neq K(t_2)$.

In order to complete the detection on the skewness and kurtosis signals, a threshold has to be set in order to pick up the peak signals. We decided to establish a statistical threshold for the skewness and kurtosis signals from their respective means μ_s and μ_k and respective standard deviations σ_s and σ_k . This threshold is defined as $\lambda_s = \mu_s + m\sigma_s$ for skewness and $\lambda_k = \mu_k + m\sigma_k$ for kurtosis, where m is a parameter whose value is adjusted using an optimization training phase in a manner that increases the system's detection rate and minimizes the false alarm rate (refer to Results section). The thresholds are represented in Figure 5.2 b) and c).

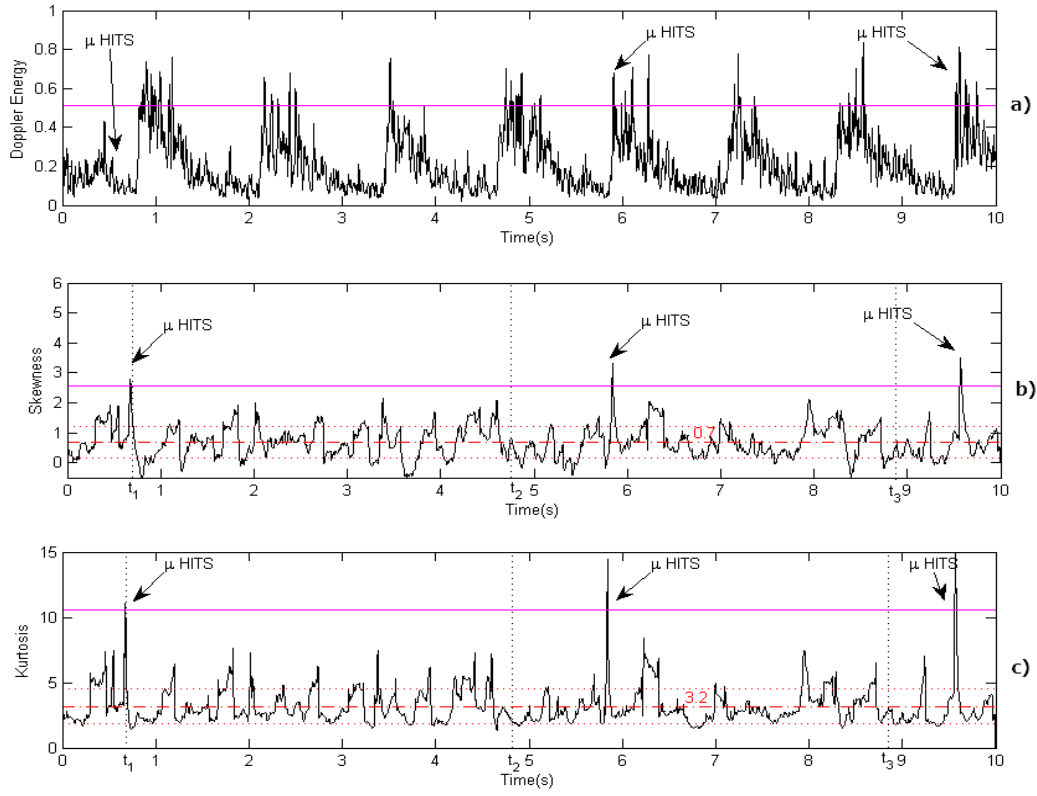


Figure 5.2: a) The Doppler energy signal. An empirical threshold is applied to obtain the micro-embolic standard detection discussed in chapter 3. b) Skewness signal calculated from the windowed energy signal. A statistical threshold is applied to complete the micro-embolic detection. The mean value of the skewness signal is 0.7 c) Kurtosis signal calculated from the windowed energy signal. A statistical threshold is applied to complete the micro-embolic detection. The mean value of the kurtosis signal is 3.2. Moreover, we choose in b) and c) three time positions: $t_1 = 0.72$ s during which an embolus is present, and $t_2 = 4.7$ s and $t_3 = 8.8$ s when no embolus is present. We detect in the case of absence of embolus: $S(t_2) \approx S(t_3) \approx 0.7$ and $K(t_2) \approx K(t_3) \approx 3.2$ while in the presence of embolus: $S(t_1) = 2.8 \neq S(t_3) \approx 0.7$ and $K(t_1) = 11 \neq K(t_3) \approx 3.2$

5.3 Results

5.3.1 Training phase results

Since the skewness and kurtosis calculations are performed using a sliding window $g(t)$ on the energy signal, an experimental test on the training phase signals is initialized to determine the optimal length of the window $g(t)$ and the optimal overlap ratio. The optimal temporal window length is 0.0073 seconds and the optimal overlap used is 95 %.

Also, using these settings we test in the training phase the best statistical thresholds $\lambda_s =$

5.3. RESULTS

$\mu_s + m\sigma_s$ and $\lambda_k = \mu_k + m\sigma_k$ for the skewness and kurtosis signals respectively. Values of m ranging between 3 and 7 are tested. Table 5.1 shows the statistical threshold for the skewness and kurtosis signals that best maximizes the detection rate and minimizes the false alarm rate.

Table 5.1: Training phase results of the optimal thresholds that best maximize the detection rate and minimize the false alarm rate for the skewness and kurtosis based detectors.

	Optimal Threshold	Detection Rate (%)	False Alarm Rate (%)
Skewness Detector	$\lambda_s = \mu_s + 4\sigma_s$	76 %	9 %
Kurtosis Detector	$\lambda_k = \mu_k + 5\sigma_k$	77 %	9 %

5.3.2 Testing phase results

Figure 5.3 represents the testing phase results for the two different energy detectors. For the energy detector based on skewness calculation the detection rate is 78 % and the false alarm rate is 9 %. For the energy detector based on kurtosis calculation the detection rate is 80 % and the false alarm rate is 10 %.¹

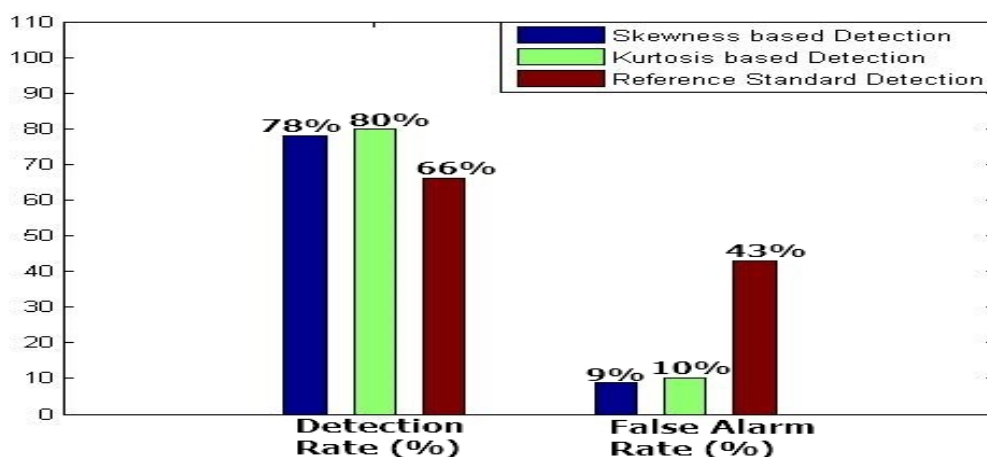


Figure 5.3: Detection and false alarm rate results for the skewness and kurtosis based detection. The results of the standard detection proposed in chapter 3 is also presented as a reference.

If compared to the standard detection using empirical constant thresholds presented in chapter 3 in Figure 3.9, the above results show that the new detectors are able to reduce the

¹Please recall here that the training and testing phases are derived from the same database used in the previous chapters.

false alarm rate by more than 30 %. Moreover, the detection rate of the new detectors is increased by 12 % for the skewness detector and 14 % for the kurtosis detector compared to that achieved by standard detectors. These results assert the accuracy and superiority of the detection based on skewness and kurtosis calculation of the Doppler energy signal over the standard detection.

In view of the fact that we have proposed 2 detectors, one based on skewness detection and the other on kurtosis detection, it is convenient to give note that the two detectors perform very similarly and yield very close results. The only difference that could be observed is that the kurtosis signal displays small fluctuations around the embolic peak detected while the skewness signal fluctuates more strongly around the embolic peaks. This provides the kurtosis detection with a small advantage in terms of the detection threshold which can be more easily and robustly set. This also means that the distortion observed in the probability density function seems to affect more the curvature than the symmetry.

5.4 Particular H-shaped peaks

We should point out that in some cases, the signals corresponding to the micro-embolic detections in the skewness and kurtosis signals appeared as H-shaped and thus are composed of 2 alternative peaks that are distanced apart by a certain distance. To determine this distance and thus count the two H-shaped parallel detections as one detection, we initialized an experimental study to calculate this distance over the different signals we used. The distance is constant showing a value of 170 milliseconds. The H-shaped peaks are shown in Fig. 5.4

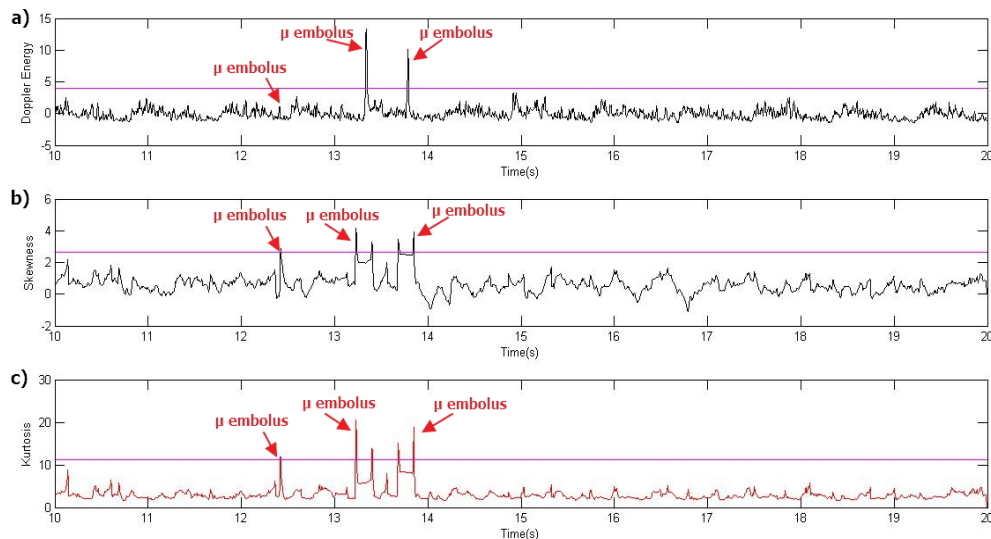


Figure 5.4: A demonstration of H-shaped peaks corresponding to micro-embolic detections.

5.5 The relative intensity increase of the smallest detectable micro-embolus

In an aim to discover the characteristic embolus relative intensity increase that the skewness and kurtosis-based detectors are capable of detecting we choose a sample of 175 embolic events having intensity increases below 15 dB. For each detector we evaluate the embolic events that it is capable of detecting and we discover out of these detections the embolus with the smallest relative intensity increase. The results are presented in Figures 5.5.

As depicted in Figure 5.5, the detector based on skewness calculations is able to detect micro-embolic signatures with relative intensity increases as low as 1.6 dB. The same results were obtained with the detector based on kurtosis calculations.

To be noted that the micro-embolic size corresponding to these relative intensity increase values is around $67.33 \mu\text{m}$. The calculations are provided in the appendix.

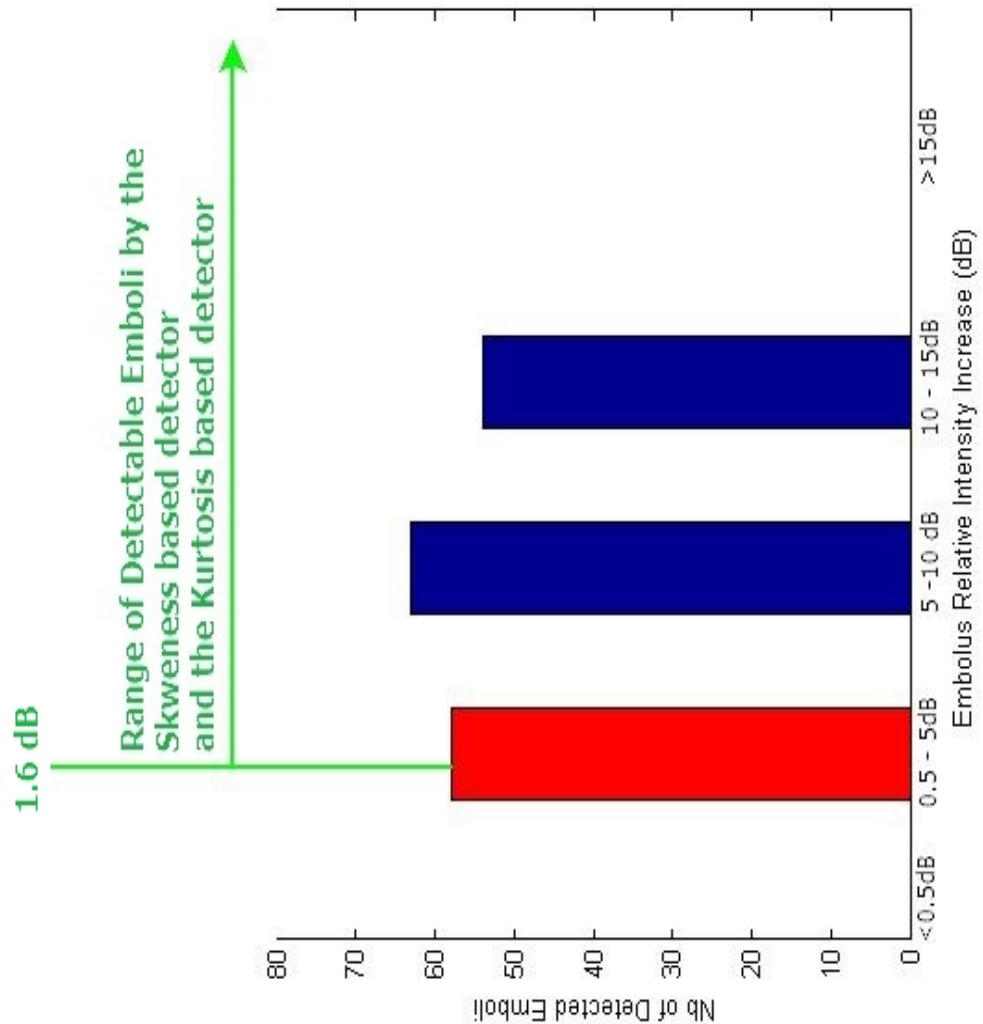


Figure 5.5: Embolus Intensity Increases relative to background blood energy for a sample of 175 chosen embolic events. The smallest detectable embolus by the detector based on skewness calculations is as low as 1.6 dB and that detected by the detector based on kurtosis calculations is also 1.6 dB.

5.6 Conclusion

In this chapter, we proposed two detectors based on the calculation of the skewness and kurtosis of the Doppler energy signal, as a tool for an enhanced micro-embolus detection.

The results obtained were clear. The methods based on HOS gave high detection rates with very low false alarm rates. They were superior to standard detection using empirical thresholds discussed in chapter 3. The reason explaining such superiority lies in the HOS sensitivity in modifying the distribution form. Based on the fact that the occurrence of a micro-embolus su-

5.6. CONCLUSION

perimposed on the Doppler energy signal imposes changes in the distribution of this signal, the skewness and kurtosis provided a new tool to detect this distribution change. During embolus-free periods the Doppler energy signals' distribution is fixed and its skewness and kurtosis are never altered. They do not show any variations. However, in the presence of a micro-embolus superimposed on the energy signal, the skewness and kurtosis signals are altered and the embolus is attributed with a peak whose peakedness level is higher than all the other points of the signal.

Consequently, we can affirm that skewness and kurtosis can be considered as new techniques for enhancing micro-embolic detection systems.

We should point out that after having implemented the HOS as a detection tool, we planned to introduce and test the use of time-varying thresholds and also sub-band decomposition into the HOS detection process. However, due to time constraints the latter steps were initialized but not completed. This will construct a future work.

Chapter 6

A Signal Processing Hierarchical Method for Artefact Rejection

6.1 Introduction

As stated previously in chapter 2, artefacts are High Intensity Transient Signals that appear in the Doppler signal due to probe tapping, probe displacement, patient movement and other external factors during TCD recording.

Although artefact rejection is not taken into account in many embolus detection systems, nevertheless it remains a fundamental step in any complete and robust detection system. Indeed, misinterpreting artefacts as embolic detections has the potential to mislead researchers and also readers into thinking the embolus detection may be more clinically valuable than it actually is. Moreover, applying embolus detection on intentionally selected artefact free signal segments could also raise questions on the reliability and feasibility of the detection system. These facts could lead to many dangerous consequences ranging from unreliable embolus detection reports to causing risks on patient safety.

6.2 Pre-considerations

At our end, we have included in the complete embolus detection systems we proposed an artefact rejection phase that ensures eliminating artefacts present in our database signals and thus applying the embolus detection process on artefact-free 'clean' signals. In order to remind you of the placement of the artefact phase in our complete embolus detection systems, we represent Figure 6.1 extracted from Figure 2.3.

A widely known fundamental method to separate artefacts from emboli is the dual-gate or multi-gate TCD [(Georgiadis et al., 1996), (Smith et al., 1996), (Molloy and Markus, 1996) (Evans, 2001), (Brucher and Russell, 2002)]. The technique is based on tracking and tracing the movement of the embolus at 2 separate depths in the insonated artery. Therefore, more than one Doppler sample volume is used. The technique usually includes two sample volumes at different positions and the signal from each volume or gate is monitored for transient increases in power. If an embolus is passing, then it will enter the first sample volume before the second

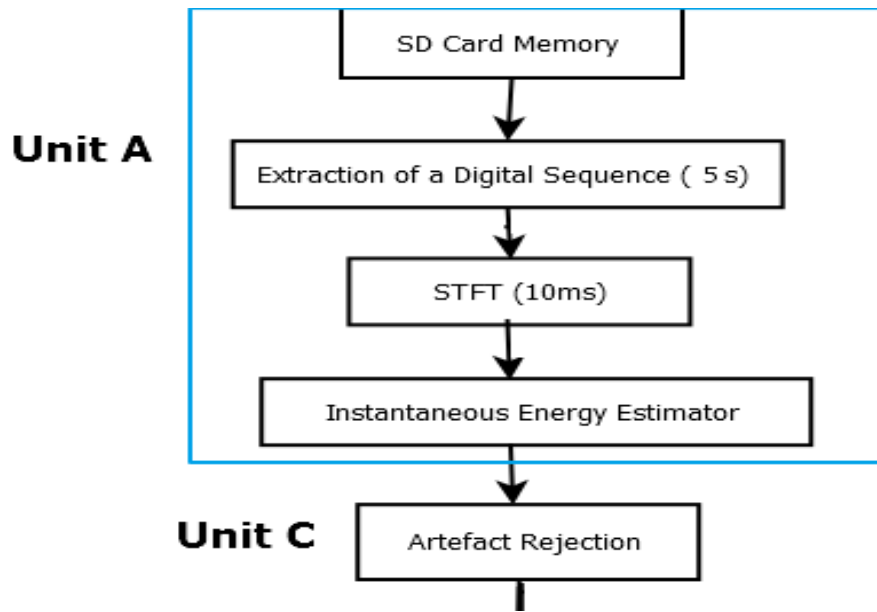


Figure 6.1: Extracted part form Figure 2.3 in chapter 3 to show the artefact rejection phase position in our complete detection system.

sample volume in the direction of embolus movement. Therefore, the resulting transient increase from the first sample volume will occur before that in the second sample volume with a time delay. In a second case, where transient increases is not due to an embolus, it is likely that either the increase in power will occur only in one sample volume or in both samples simultaneously.

However when a single-gated system is to be used, other artefact features should be considered to perform rejection. The latter case resembles the situation of this dissertation, where the Holter system used allows only single gated emission. Therefore, we represent Doppler signal-gated based artefact rejection procedures.

When using single-gated TCDs, the leading method for artefact rejection depends on a strong hypothesis stating that in the Doppler blood flow velocity spectrum artefacts are bidirectional while emboli are unidirectional. This method has been extensively proved and stated by Spencer et al. (1990), Markus et al. (1993), Ringelstein et al. (1998), Aydin et al. (2004), Choi et al. (2010) and Serbes et al. (2014). This means that artefacts exhibit velocity components both in the forward and reverse flows while emboli exhibit velocity components in the forward flow only. The forward flow denotes the channel that contains the main flow of blood while in the reverse no blood flow is present (noise signal).

However, a study performed by a former laboratory colleague (Biard et al., 2003) showed that artefact signals, even if rarely occurring, could be exclusively unidirectional in the forward flow. In one case of artefacts caused by probe displacement, it was shown that when this probe displacement happens in the same forward sense as the blood flow, tissue and wall motion artefacts will always show in the forward Doppler spectrum.

Based on this, and in order to discover the directionality properties of the artefacts we have in our database, we tested 218 artefacts using spectrogram visualization of the forward and reverse flows. 95 % of the artefacts are bidirectional and 5 % are unidirectional.

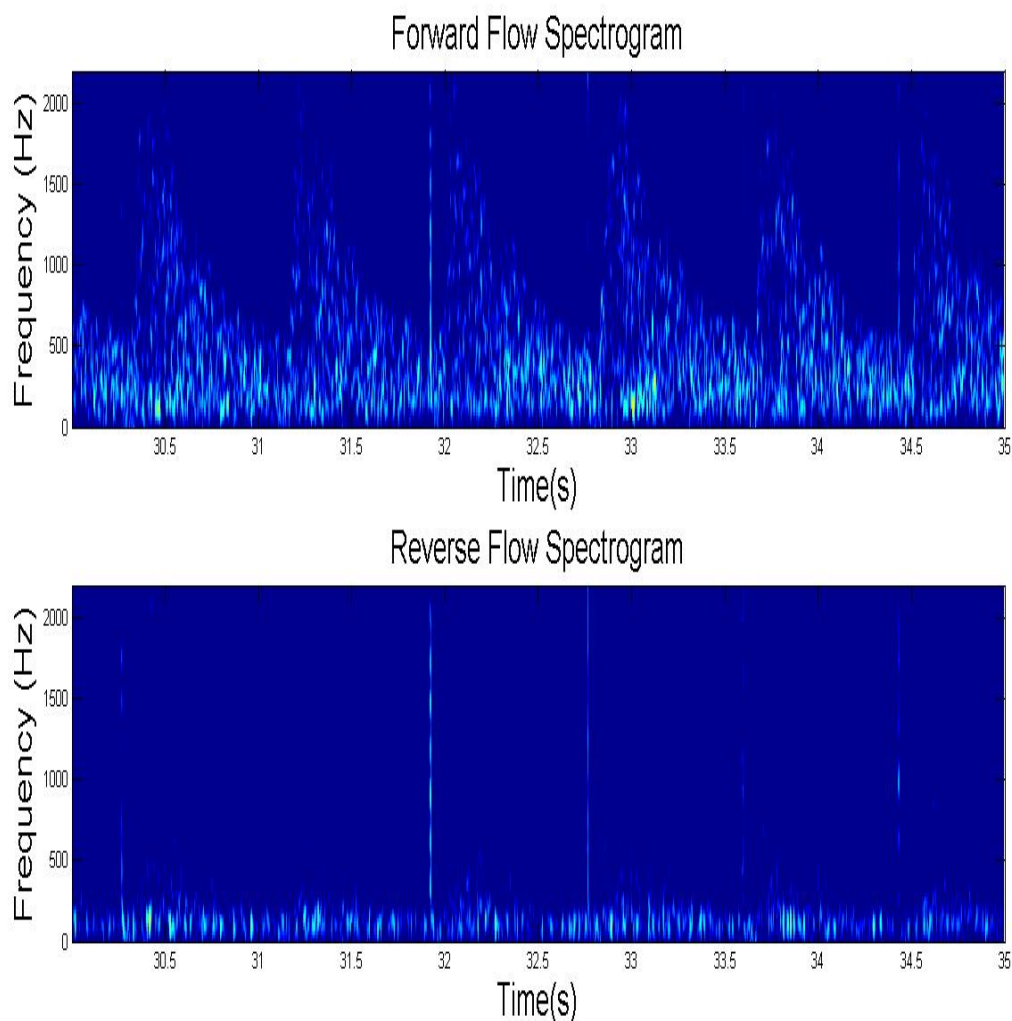


Figure 6.2: A representation of the forward flow and reverse flow spectrograms of a 5 second signal segment containing 5 artefacts. Note that in many cases artefacts show a straight line running through all the vertical spectrum.

6.3 Rejecting Bidirectional Artefacts

Since the majority of artefacts turned out to have a bidirectional behavior, we will first present the method we proceeded with to reject this type of artefacts. To better understand the procedure, we present in Figure 6.2 the forward and reverse spectrograms of a certain signal segment containing 5 artefact signatures. The calculated energies from these spectrograms are presented in Figure 6.3. As can be seen from the two figures, the artefact signals can be clearly depicted in the reverse flow spectrogram and in the calculated reverse energy signal.

The first step in this artefact rejection procedure is to identify and detect the artefacts in the reverse flow energy signal. The artefacts in this blood flow-free energy signal are always associated with higher peaks than the background noise. Thus, they can be easily and straightforwardly detected by a peak detection algorithm or by a threshold set above the maximum

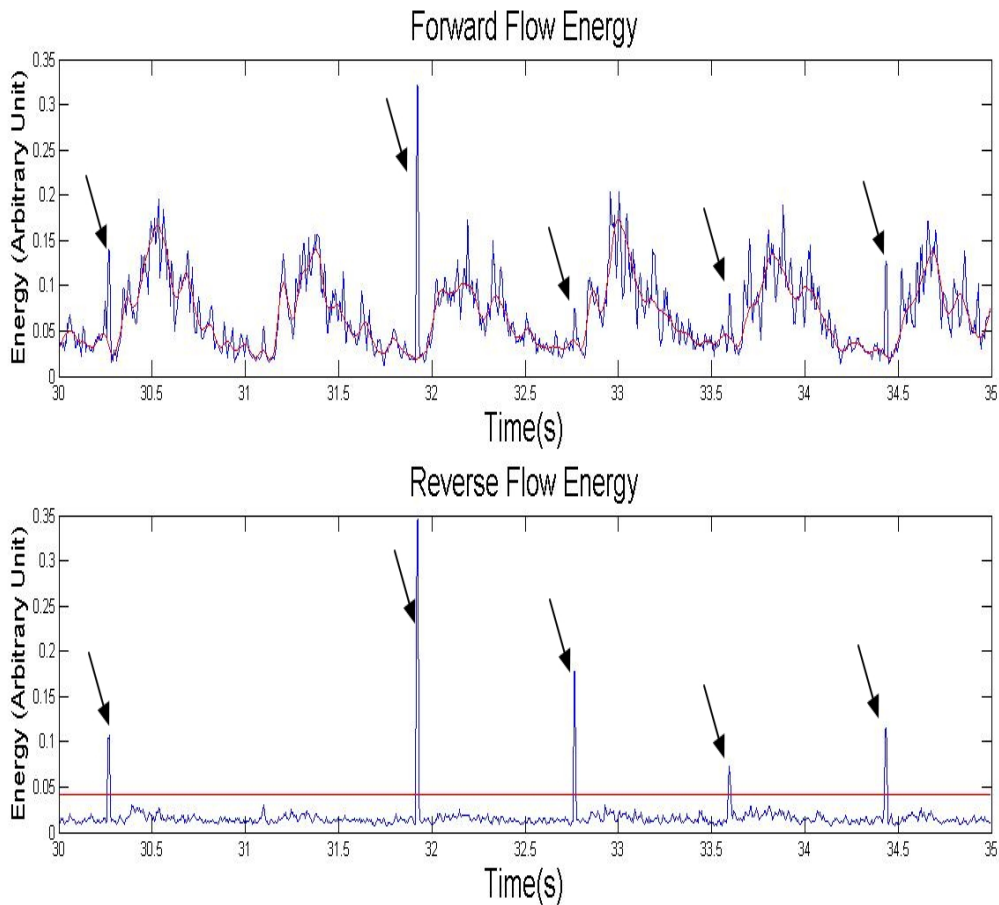


Figure 6.3: A representation of the forward flow and reverse flow energy signals calculated from the spectrograms in Figure 6.2.

background level as shown in Figure 6.3. Once the artefacts in the reverse flow are detected, the next step is to cancel these artefacts at their same positions in the forward flow. For clarification, we note that the artefact rejection is achieved on the forward flow signal since it is the signal where embolus detection is performed. Rejecting artefacts in the reverse flow is of no value.

Therefore, in order to reject the artefacts in the forward flow in a robust manner, we tend to cancel their associated forward signature. In a technical manner, canceling the artefact signature in the forward flow resembles setting it to zero. However, since the energy is not centered (mean of the energy is not zero), technically setting the value of the forward artefact to zero results in a misshaped or malformed signature directed in a descending form in the forward signal. So in order, to overcome this problem, we propose to set the value of the artefact signature in the forward flow equal to the value of the smooth signal presented in chapter 3. The smooth signal, being a description of the trend of the energy signal, contains only blood flow and is free of embolic or artefact signatures. Its value at artefact signatures is approximately zero. Therefore, setting the artefact signature to the value of the smooth will cancel it out in the

6.3. REJECTING BIDIRECTIONAL ARTEFACTS

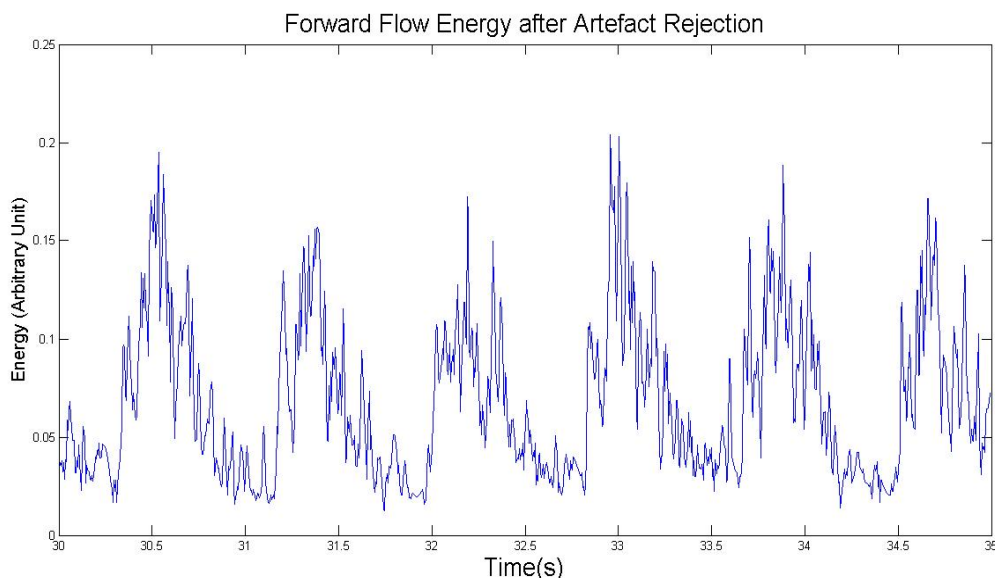


Figure 6.4: A representation of the forward flow energy signal of Figure 6.3 after the artefact rejection procedure.

energy signal. In a mathematical representation we can say that:

$$Energy_{artefact\ position}(forward\ flow) = Smooth_{artefact\ position}(forward\ flow). \quad (6.1)$$

In Figure 6.4, we show the artefact signatures of the energy signal of Figure 6.3 after being set to the smoothed value at their position. The artefacts are well canceled.

To be noted that a primary rejection was first based on subtracting the energy amplitudes of the detected artefacts in the reverse flow from their amplitudes in the forward flow. However, the method was disturbed by the fact that the artefact energies in the forward and reverse flow are never the same. Indeed the energy in the forward flow is usually greater. This is because in the forward flow the energy of the blood flow adds up to the signal. While in the reverse flow, no blood flow is conducted thus only negligible noise adds up to the energy. After this achieved study, we would like to address the fact that the energy of the artefact reverse and forward components is never identical.

6.3.1 Showers of Artefacts

In particular cases, artefacts produce very large signals of long duration and high amplitude. They induce intense burden on the energy signal to a level that the energy signal disappears and can no longer be seen or detected. For these types of artefacts it is nearly impossible to cancel them by the previous method we introduced. In this case, the whole reverse flow energy is subtracted from the forward flow energy in order to completely remove the large artefacts. In the case of showers, and as stated before, the forward flow energy of artefacts is always greater than the reverse energy of artefacts but the particularity here is that the energy amplitudes are approximately equal. Therefore, subtracting the two energy signals would yield perfect elimination of the artefacts. An example of a shower of artefacts is presented in Figure 6.5.

In Figure 6.6, the energies of the forward and reverse flows are represented. It can be noticed that the latter energies are approximately equal. Also in Figure 6.6, the subtraction of the forward and reverse flow energies is shown. It can be clearly seen how the subtraction allows perfect elimination of the artefact showers and also allows retrieving the forward energy signal (background) that had been embedded in the artefact showers. However, on another hand, at the positions where the artefacts were removed, the background flow was also removed. This is the price to pay with such techniques for rejecting artefact showers. No other solutions have been envisaged to overcome this at the moment, but the removed background flow will not greatly influence the application of detection techniques.

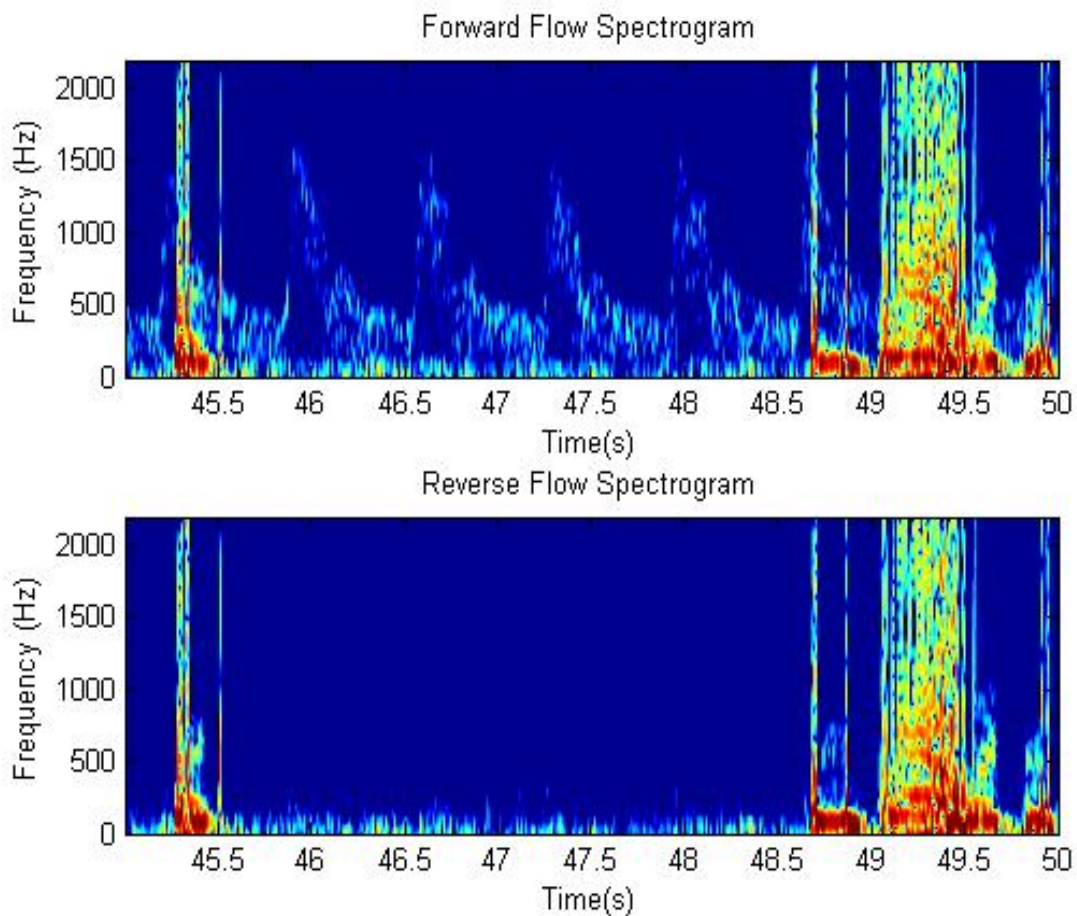


Figure 6.5: A representation of a shower of artefacts.

6.3. REJECTING BIDIRECTIONAL ARTEFACTS

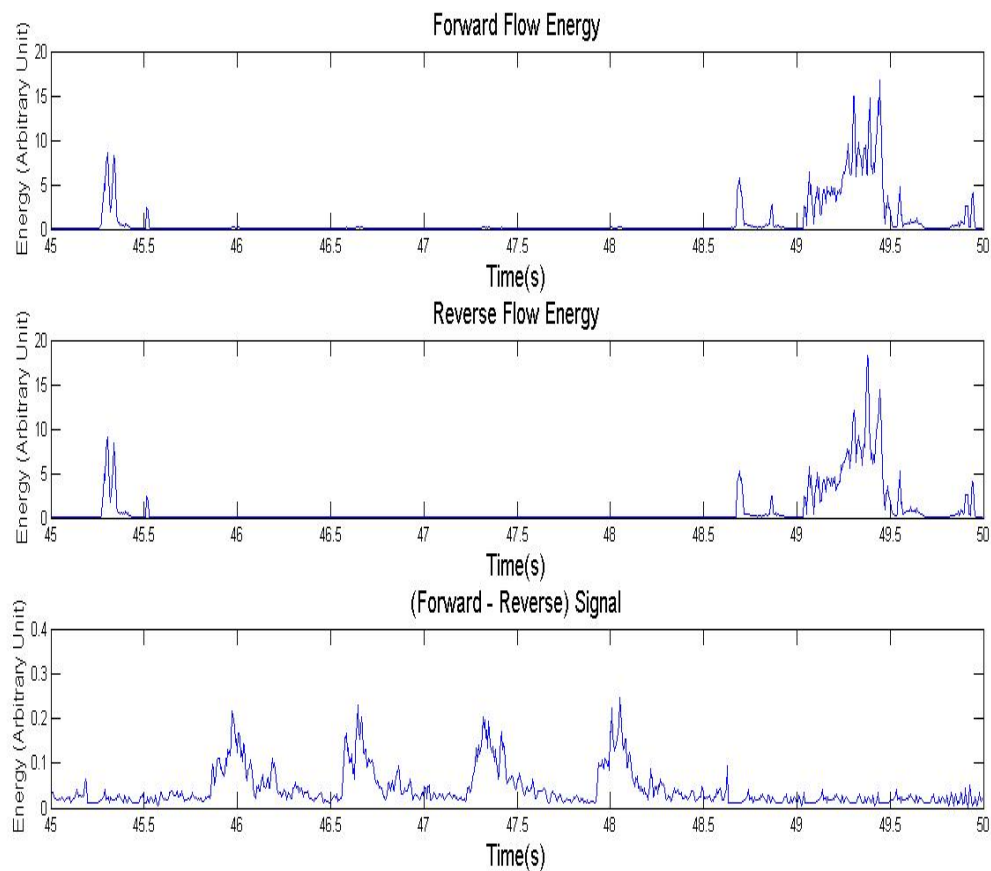


Figure 6.6: A representation of the forward and reverse flow energy signals of the spectrograms in Figure 6.5. By subtracting the reverse signal from the forward signal, the artefact shows are eliminated and the forward signal that had been embedded in the artefacts is retrieved.

6.3.2 Automatic Holter probe displacement Artefacts

Due to the automatic nature of the robotized Holter probe, this probe automatically displaces from one position to another at some instants during the recording time. During such rapid short movements, the signal recording is halted until the probe displaces and restarts again. After this restart of the probe insonification, an artefact associated to the probe displacement is directly recorded within an interval of 100 to 200 milliseconds. These occurring artefacts are eliminated by the method proposed in section 6.3. An example of this type of artefacts is given in Figure 6.7 and Figure 6.8.

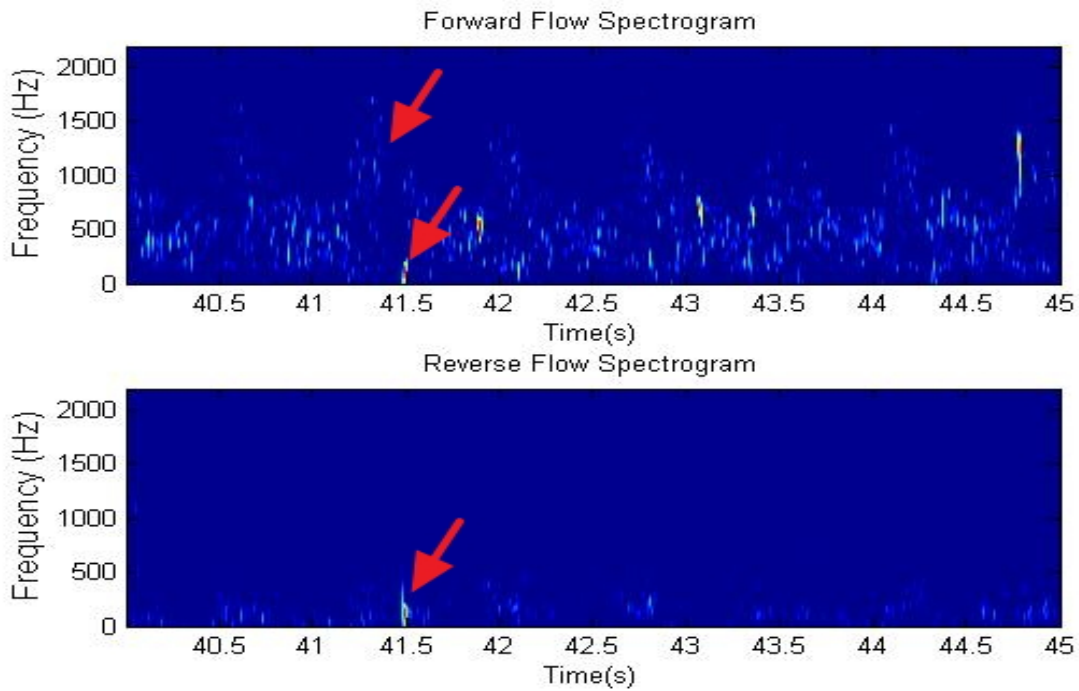


Figure 6.7: A representation of an artefacts resulting from the automatic Holter probe displacement .

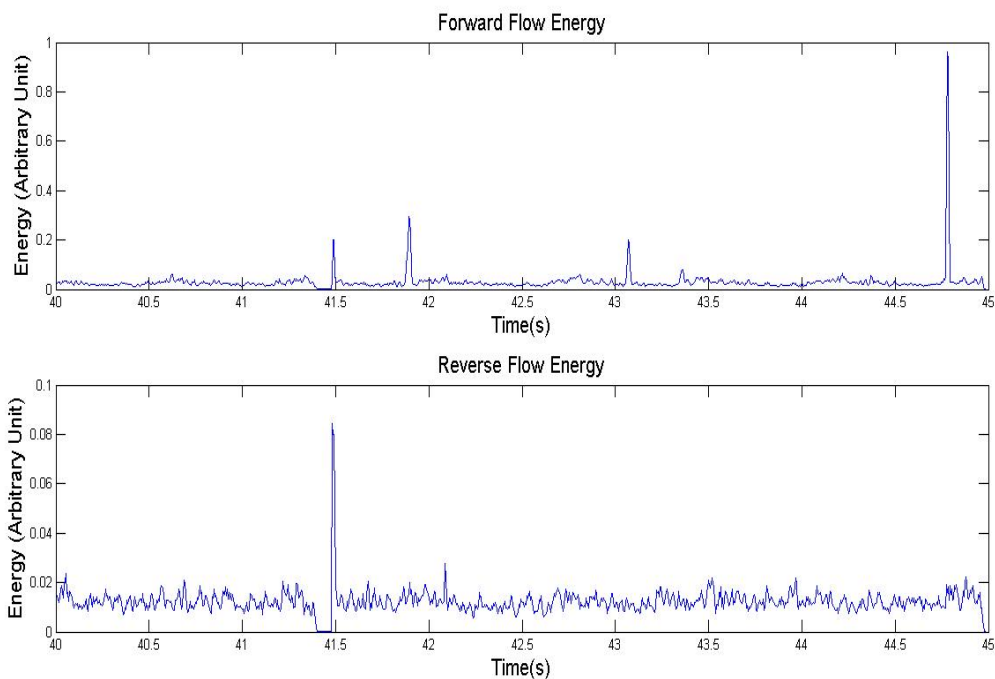


Figure 6.8: A representation of the signature of an artefact resulting from probe displacement in the reverse and forward flow energy signals. Both flow signals are halted when the probe is in displacement. This artefact is rejected using the method of section 6.3.

6.4 Rejecting Unidirectional Artefacts

While the bidirectional artefacts in the database were identified by using the reverse flow, the unidirectional artefacts were identified based on their frequency component in the forward flow spectrogram. The forward flow was used since the study of Biard et al. (2003) had demonstrated that artefacts could be unidirectional particularly in the forward flow. An example of a unidirectional artefact is presented in the spectrogram in Figure 6.9. The identification of the unidirectional artefacts in our database was primarily based on frequency since it has been widely mentioned that artefacts have lower frequencies than emboli [(Markus et al., 1993), (Devuyst et al., 2001), (Biard et al., 2003), (Darbellay et al., 2004)]. Therefore, we determined the embolic and artefact frequency range. The embolic frequency ranges from 631 Hz to 2005 Hz . The artefact frequency ranges from 125 Hz to 550 Hz . Then a search was initialized in the forward spectrogram for signatures with frequencies between 125 Hz to 550 Hz that would correspond to artefacts. If no corresponding signature is found in the reverse flow, then the forward signature is recorded as a unidirectional artefact. Moreover, in order to perfectly confirm that these signatures are artefacts, we searched for artefact-embolus discriminative parameters based on the energy signal rather than on the spectrogram. Two discriminative parameters were found, the rise rates and fall rates. These two parameters could assure the signature found in the forward flow spectrogram is an artefact. The results of the rise rates and false rates for both embolic and artefact signals are presented in Figure 6.10. Embolic signal rise rates range between 0.015 s and 0.05 s while the fall rates range between 0.02 and 0.03 s . Artefact signal rise rates range between 0.002 and 0.01 s while the fall rates range between 0.002 s and 0.015 s . At the end, 11 unidirectional artefacts were depicted and confirmed and then rejected by the same method in section 6.3 by setting them to the smooth value.

6.5 Results

218 artefact signals are included in our database constituted of 25 signals. As stated in the introduction section 207 are bidirectional artefacts (95 %). By applying the bidirectional procedure for removing artefacts we succeeded in removing 202 out of these 207 artefacts. Moreover, 11 artefacts (5 %) were identified as unidirectional forward artefacts and were rejected. Therefore in total, out of the 218 artefacts, 213 were successfully removed.

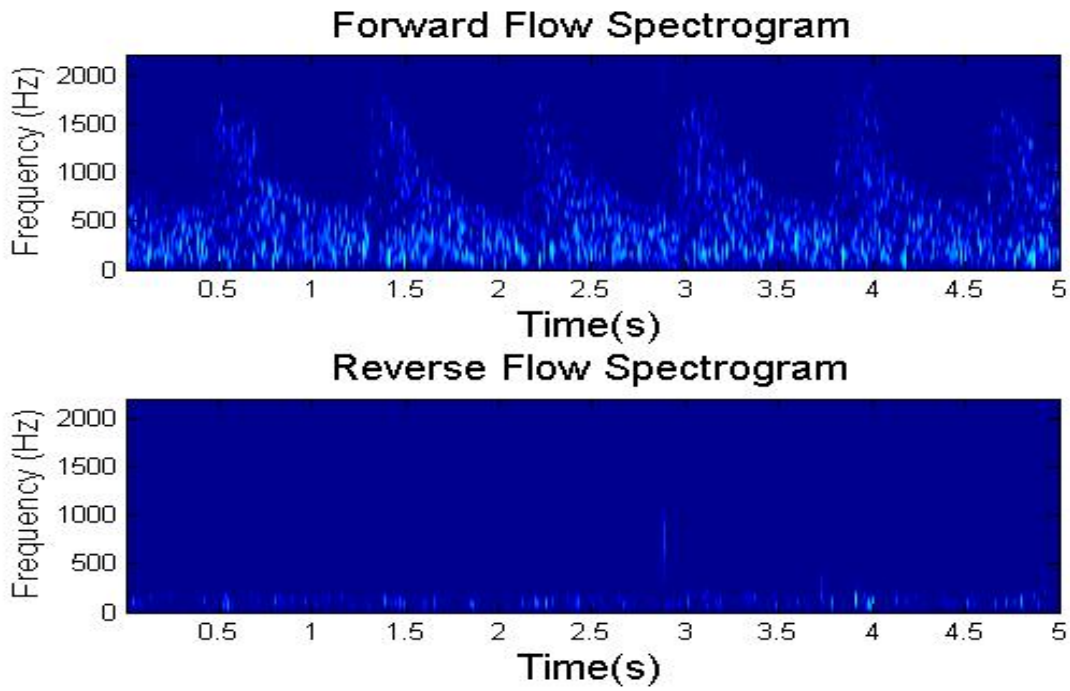


Figure 6.9: A spectrogram representation showing a unidirectional forward artefact pointed out in red in the upper spectrogram.

6.6. CONCLUSION

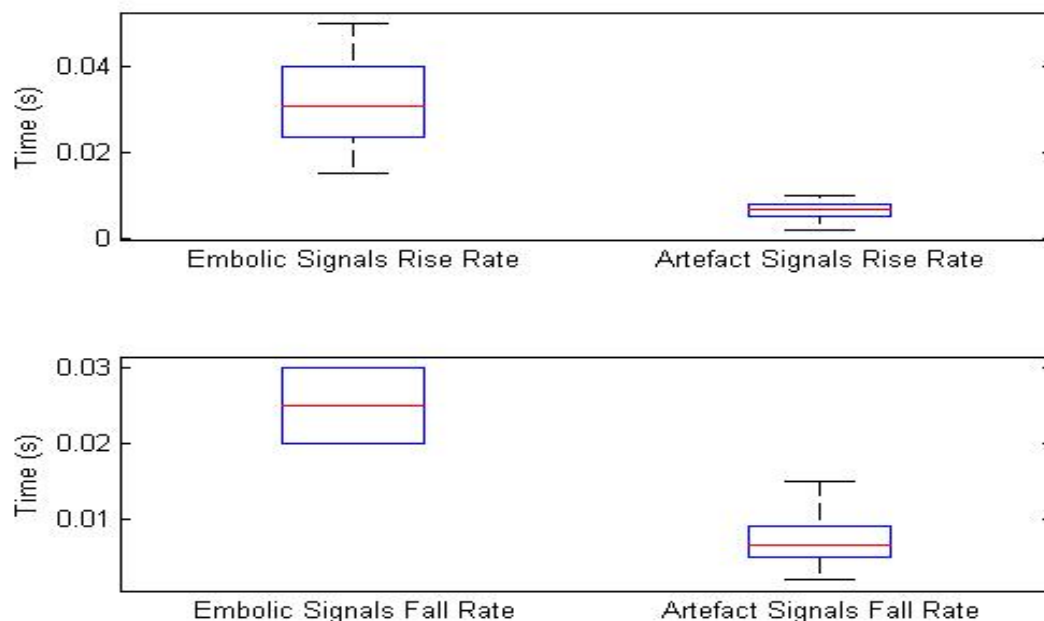


Figure 6.10: A box plot showing the rise rates and fall rates of embolic and artefact signals. Embolic signal rise rates range between 0.015 s and 0.05 s while the fall rates range between 0.02 s and 0.03 s. Artefact signal rise rates range between 0.002 s and 0.01 s while the fall rates range between 0.002 s and 0.015 s.

6.6 Conclusion

High intensity transient signals produced due to artefacts generated during the TCD recording could highly affect the performance and reliability of any embolus detection process. For this reason, we have included an artefact rejection phase applied before initialization of the embolus detection procedures in order to ensure that the signals are artefact-free clean signals. This artefact rejection phase provides more reliability and precision to the different embolus detection systems proposed.

We have covered the rejection and elimination of different bidirectional and unidirectional artefacts we might encounter in the database we use. The methods are founded on the fact that the Holter system is single-gated. Thus we prove that it is possible to robustly reject artefacts without necessarily using standard rejection procedures based on dual-gated or multi-gated TCDs.

Chapter 7

Conclusions, limitations and outlook

7.1 Conclusions

In order to understand the nature of micro-emboli and the importance of achieving a robust micro-embolic detection system, we have explained in this dissertation different biological and physical aspects of micro-emboli before discussing cerebral embolism and its relation to Cerebrovascular Accidents, the second cause of mortality worldwide. After introducing a literature review of the different detection methods previously introduced, we presented a technical demonstration of the TCD instrument of detection along with the new Holter TCD we use.

As a purpose to ameliorate the detection of micro-embolic signals, we have proposed several offline signal processing detection systems. The systems are original and based on several hypotheses that were not considered until now. Major improvements were achieved ranging from increasing micro-embolic detection rates, decreasing the false alarm rates, and detecting very small micro-emboli that could constitute in later stages precursors of coming large emboli with high stroke risks.

In the detection phase, first we implemented standard detection methods on the set of real signals constituting our database which was also proved to be homogeneous. From a conceptual point of view, the standard detection is defined by the detection applied on the whole Doppler energy signal with constant empirical thresholds used for the decision of detecting micro-embolic signals. We also re-implemented a detection similar to the standard but with the use of constant thresholds determined from the statistics of the energy signal. Both constant threshold-based detections were used as comparison tools with the new proposed detectors.

A novel technique we first introduced in chapter 3 is based on the detection of emboli from energy fluctuations rather than from the energy signal. We also developed a time-varying threshold rather than using traditional constant thresholds. The technique proved to be a very solid mean for detecting the smallest micro-emboli in a robust manner.

A second idea, presented in chapter 4, was to introduce sub-band decomposition as an additional tool that would boost the detection performances. Indeed, when the energy fluctuations-based detector was coupled with sub-band decomposition extremely powerful results were obtained. The detection rate was hugely increased and the false alarm rate severely decreased with the ability of detecting very small-sized micro-emboli. The sub-band decomposition method also proved to be effective when used with the standard detection where it helped increase the

performances of these detectors. Sub-band decomposition was introduced in two methods, first through decomposing the short time Fourier transform spectrum into n ideal frequency bands and second using the wavelet packet decomposition to obtain n ideal frequency bands.

On another hand, in chapter 5, we proposed yet two other detectors based on windowed calculation of the skewness and kurtosis of the energy signal. The implementation was original and carried effective solutions particularly in terms of decreasing the false alarm rates while preserving high detection rates.

Moreover, in order to ensure the reliability and well-functioning of the different detection systems, we included an artefact rejection procedure, in chapter 6, so that both bi-directional and unidirectional artefacts are eliminated. This in turn ensures that the presence of artefacts would not mislead the detection systems.

There are a number of implications for clinical strategies and patient outcome based on the highly-performing techniques we achieved. Due to low relative intensity increase-detected micro-emboli, detection of small micro-embolic events would be more achievable. High micro-embolic detection rates, would boost prevention of Cerebrovascular Accidents and enhance patient safety. Moreover, owing to the low false alarm rates achieved, more reliable and factual reports could be handed to medical doctors. Thus more truthful diagnosis and treatment would be offered to the patients by these medical doctors. Together, these factors should enhance the capabilities of medical diagnosis ranging from micro-embolic detection to patient treatment.

7.2 Limitations

- The different detectors were applied to artefact and embolic Doppler signals solely. The database lacked healthy signals (embolus and artefact free).
- Inability to consider an in vitro model where the presence of an embolus could be confirmed under controlled conditions.

7.3 Outlook

In this dissertation, we have contributed in clarifying and classifying the problematic of detection of micro-emboli and we brought along quantifiable solutions in terms of performance of detection.

Furthermore, the following points should be considered in the terms to come:

- Implementing time varying thresholds in the high order statistics based detection and also coupling this detection with sub-band decomposition. The latter steps were not achieved due to lack of time.
- Testing the performance of the different proposed detectors on a set of healthy signals.
- Testing the performance of the different proposed detectors on a set of signals acquired using a TCD system other than the Holter TCD.
- Applying the developed algorithms in an online Holter system.

7.3. OUTLOOK

- Build and test other signal processing techniques for the detection of micro-emboli such as using the Hidden Markov Model.
- Transform the built detection algorithms to commercial versions (C++ for instance) that could be used automatically on PCs, tablets, i-phones, etc.

Bibliography

- Aaslid, R., Markwalder, T.-M., and Nornes, H. (1982). Noninvasive transcranial doppler ultrasound recording of flow velocity in basal cerebral arteries. *Journal of neurosurgery*, 57(6):769–774.
- Ackerstaff, R., Babikian, V., Georgiadis, D., et al. (1995). Consensus committee of the ninth international cerebral hemodynamic symposium. *Stroke*, 26:1123.
- Altunkaya, S., Kara, S., Görmüş, N., and Herdem, S. (2010). Statistically evaluation of mechanical heart valve thrombosis using heart sounds. In *Proceedings of the World Congress on Engineering*, volume 1.
- Aydin, N. (2007). Dwt based adaptive threshold determination in embolic signal detection. In *Second NASA/ESA Conference on Adaptive Hardware and Systems (AHS 2007)*, pages 214–219. IEEE.
- Aydin, N. and Markus, H. S. (1999). Detection of embolic signals using wavelet transform. In *NSIP*, pages 774–778.
- Aydin, N. and Markus, H. S. (2000). Optimization of processing parameters for the analysis and detection of embolic signals. *European Journal of ultrasound*, 12(1):69–79.
- Aydin, N., Markus, H. S., and Marvasti, F. (2001). Detection and estimation of embolic doppler signals using discrete wavelet transform. In *Acoustics, Speech, and Signal Processing, 2001. Proceedings.(ICASSP'01). 2001 IEEE International Conference on*, volume 2, pages 1049–1052. IEEE.
- Aydin, N., Marvasti, F., and Markus, H. S. (2004). Embolic doppler ultrasound signal detection using discrete wavelet transform. *IEEE Transactions on Information Technology in Biomedicine*, 8(2):182–190.
- Aydin, N., Padayachee, S., and Markus, H. S. (1999). The use of the wavelet transform to describe embolic signals. *Ultrasound in medicine & biology*, 25(6):953–958.
- Biard, M., Kouame, D., Girault, J., and Patat, F. (2003). Discrimination between emboli and artifacts during transcranial doppler. In *the fifth World Congress on Ultrasonics Proceedings (WCU 2003), Paris*.
- Bierens, H. J. (2012). The wold decomposition.
- Brucher, R. and Russell, D. (2002). Automatic online embolus detection and artifact rejection with the first multifrequency transcranial doppler. *Stroke*, 33(8):1969–1974.

- Chen, Y. and Wang, Y. (2008). Doppler embolic signal detection using the adaptive wavelet packet basis and neurofuzzy classification. *Pattern recognition letters*, 29(10):1589–1595.
- Choi, Y., Saqqur, M., Asil, T., Jin, A., Stewart, E., Stephenson, C., Ibrahim, M., Roy, J., Boulanger, J.-M., Coutts, S., et al. (2010). A combined power m-mode and single gate transcranial doppler ultrasound microemboli signal criteria for improving emboli detection and reliability. *Journal of Neuroimaging*, 20(4):359–367.
- Chua, K. C., Chandran, V., Acharya, U. R., and Lim, C. M. (2010). Application of higher order statistics/spectra in biomedical signals—A review. *Medical engineering & physics*, 32(7):679–689.
- Chung, E., Fan, L., Degg, C., and Evans, D. H. (2005). Detection of doppler embolic signals: psychoacoustic considerations. *Ultrasound in medicine & biology*, 31(9):1177–1184.
- Colantonio, S. and Salvetti, O. (2007). Microembolic signal characterization by transcranial doppler imaging. *Pattern Recognition and Image Analysis*, 17(4):567–577.
- Cullinane, M., Kaposzta, Z., Reihill, S., and Markus, H. S. (2002). Online automated detection of cerebral embolic signals from a variety of embolic sources. *Ultrasound in medicine & biology*, 28(10):1271–1277.
- Cullinane, M., Reid, G., Dittrich, R., Kaposzta, Z., Ackerstaff, R., Babikian, V., Droste, D. W., Grossett, D., Siebler, M., Valton, L., et al. (2000). Evaluation of new online automated embolic signal detection algorithm, including comparison with panel of international experts. *Stroke*, 31(6):1335–1341.
- Darbellay, G. A., Duff, R., Vesin, J.-M., Despland, P.-A., Droste, D. W., Molina, C., Serena, J., Sztajzel, R., Ruchat, P., Karapanayiotides, T., et al. (2004). Solid or gaseous circulating brain emboli: are they separable by transcranial ultrasound? *Journal of cerebral blood flow & metabolism*, 24(8):860–868.
- Devuyst, G., Darbellay, G., Vesin, J.-M., Kemeny, V., Ritter, M., Droste, D., Molina, C., Serena, J., Sztajzel, R., Ruchat, P., et al. (2001). Automatic classification of hits into artifacts or solid or gaseous emboli by a wavelet representation combined with dual-gate tcd. *Stroke*, 32(12):2803–2809.
- Droste, D. W. and Ringelstein, E. B. (1998). Detection of high intensity transient signals (hits): How and why? *European journal of ultrasound*, 7(1):23–29.
- Evans, D. (2001). Multigate emboli detection. in *Cerebrovascular Ultrasound: Theory, practice and future developments*, Ed. eds, Cambridge University Press, Cambridge, 2001, pp. 360- 373.
- Evans, D. H. (2003). Ultrasonic detection of cerebral emboli. In *2003 IEEE Symposium on Ultrasonics*, volume 1, pages 316–326. IEEE.

- Evans, D. H., Smith, J. L., and Naylor, A. R. (1997). Characteristics of doppler ultrasound signals recorded from cerebral emboli. *Ultrasound in Medicine & Biology*, 23:S140.
- Fan, L., Evans, D. H., and Naylor, A. R. (2001a). Automated embolus identification using a rule-based expert system. *Ultrasound in medicine & biology*, 27(8):1065–1077.
- Fan, L., Evans, D. H., and Naylor, A. R. (2001b). Automated embolus identification using a rule-based expert system. *Ultrasound in medicine & biology*, 27(8):1065–1077.
- Ferroudji, K., Benoudjit, N., Bahaz, M., and Bouakaz, A. (2012). Selection of a suitable mother wavelet for microemboli classification using svm and rf signals. In *2012 24th International Conference on Microelectronics (ICM)*, pages 1–4. IEEE.
- Gençer, M., Bilgin, G., and Aydin, N. (2013). Embolic doppler ultrasound signal detection via fractional fourier transform. In *2013 35th Annual International Conference of the IEEE Engineering in Medicine and Biology Society (EMBC)*, pages 3050–3053. IEEE.
- Georgiadis, D., Goeke, J., Hill, M., König, M., Nabavi, D., Stögbauer, F., Zunker, P., and Ringelstein, E. (1996). A novel technique for identification of doppler microembolic signals based on the coincidence method in vitro and in vivo evaluation. *Stroke*, 27(4):683–686.
- Georgiadis, D., Grosset, D. G., Kelman, A., Faichney, A., and Lees, K. R. (1994). Prevalence and characteristics of intracranial microemboli signals in patients with different types of prosthetic cardiac valves. *Stroke*, 25(3):587–592.
- Gholinezhadasnefistani, S., Temko, A., Stevenson, N., Boylan, G., Lightbody, G., and Marnane, W. (2015). Assessment of quality of ecg for accurate estimation of heart rate variability in newborns. In *2015 37th Annual International Conference of the IEEE Engineering in Medicine and Biology Society (EMBC)*, pages 5863–5866. IEEE.
- Girault, J.-M. (2013). *Cerebral Microembolism Synchronous Detection with Wavelet Packets*, chapter 4, pages 245–287. Signal and Image Multiresolution Analysis. Wiley Online Library.
- Girault, J.-M., Kouamé, D., Ouahabi, A., and Patat, F. (2000). Micro-emboli detection: an ultrasound doppler signal processing viewpoint. *Biomedical Engineering, IEEE Transactions on*, 47(11):1431–1439.
- Girault, J.-M., Kouamre, D., and Tranquart, F. (2007). Synchronous detection of emboli by wavelet packet decomposition. In *2007 IEEE International Conference on Acoustics, Speech and Signal Processing-ICASSP'07*, volume 1, pages I–409. IEEE.
- Girault, J.-M., Ménigot, S., and Deibine, L. (2010). Automatic detection of micro-emboli by means of a generalized autoregressive conditional heteroskedasticity model. *The Journal of the Acoustical Society of America*, 128(4):2304–2304.
- Girault, J.-M. and Zhao, Z. (2014). Synchronous detector as a new paradigm for automatic microembolus detection. *International Journal of Biomedical Engineering and Technology*, 14(1):60–70.

- Gonçalves, I. B., Leiria, A., and Moura, M. (2011). Assessing the detection of embolic signals using continuous wavelet transform. In *Computational Vision and Medical Image Processing Conference Proceedings*, pages 387–392.
- Gonçalves, I. B., Leiria, A., and Moura, M. (2013). Stft or cwt for the detection of doppler ultrasound embolic signals. *International journal for numerical methods in biomedical engineering*, 29(9):964–976.
- Hennerici, M. (1994). High intensity transcranial signals (hits): a questionable 'jackpot' for the prediction of stroke risk. *The Journal of heart valve disease*, 3(2):124.
- Jensen, J. A. (1996). *Estimation of blood velocities using ultrasound: a signal processing approach*. Cambridge University Press.
- Krongold, B. S., Sayeed, A. M., Moehring, M. A., Ritcey, J. A., Spencer, M. P., and Jones, D. (1999). Time-scale detection of microemboli in flowing blood with doppler ultrasound. *IEEE transactions on biomedical engineering*, 46(9):1081–1089.
- Lueang-on, C., Tantibundhit, C., and Muengtaweepongsa, S. (2013). Abstract wmp60: Automatic embolic signal detection using adaptive wavelet packet transform and adaptive neuro-fuzzy inference system. *Stroke*, 44(Suppl 1):AWMP60–AWMP60.
- Markus, H., Cullinane, M., and Reid, G. (1999). Improved automated detection of embolic signals using a novel frequency filtering approach. *Stroke*, 30(8):1610–1615.
- Markus, H., Loh, A., and Brown, M. M. (1993). Computerized detection of cerebral emboli and discrimination from artifact using doppler ultrasound. *Stroke*, 24(11):1667–1672.
- Markus, H. S., King, A., Shipley, M., Topakian, R., Cullinane, M., Reihill, S., Bornstein, N. M., and Schaafsma, A. (2010). Asymptomatic embolisation for prediction of stroke in the asymptomatic carotid emboli study (aces): a prospective observational study. *The Lancet Neurology*, 9(7):663–671.
- Markus, H. S. and Reid, G. (1999). Frequency filtering improves ultrasonic embolic signal detection. *Ultrasound in medicine & biology*, 25(5):857–860.
- Markus, H. S., Thomson, N. D., and Brown, M. M. (1995). Asymptomatic cerebral embolic signals in symptomatic and asymptomatic carotid artery disease. *Brain*, 118(4):1005–1011.
- Martin, M. J., Chung, E. M., Ramnarine, K. V., Goodall, A. H., Naylor, A. R., and Evans, D. H. (2009). Thrombus size and doppler embolic signal intensity. *Cerebrovascular Diseases*, 28(4):397–405.
- Marvasti, S., Gillies, D., Marvasti, F., and Markus, H. S. (2004). Online automated detection of cerebral embolic signals using a wavelet-based system. *Ultrasound in medicine & biology*, 30(5):647–653.

- Mess, W. and Hennerici, M. (2001). High intensity transient signals. In *Cerebrovascular ultrasound*, pages 297–316. Cambridge University Press, Cambridge, United Kingdom.
- Moehring, M. A. and Klepper, J. R. (1994). Pulse doppler ultrasound detection, characterization and size estimation of emboli in flowing blood. *Biomedical Engineering, IEEE Transactions on*, 41(1):35–44.
- Moehring, M. A., Spencer, M. P., Davis, D. L., and Demuth, R. P. (1995). Exploration of the embolus to blood power ratio model (ebr) for characterizing microemboli detected in the middle cerebral artery. In *Ultrasonics Symposium, 1995. Proceedings, 1995 IEEE*, volume 2, pages 1531–1535. IEEE.
- Molloy, J. and Markus, H. S. (1996). Multigated doppler ultrasound in the detection of emboli in a flow model and embolic signals in patients. *Stroke*, 27(9):1548–1552.
- Morse, P. M. and Ingard, K. U. (1968). *Theoretical acoustics*. Princeton university press.
- Mühlbacher-Karrer, M., Munch, M., Svorkmo, M., and Trentin, C. (2008). Correlational study between the severity of carotid stenosis and bio-acoustic features.
- Murtagh, B. and Smalling, R. W. (2006). Cardioembolic stroke. *Current atherosclerosis reports*, 8(4):310–316.
- Ng, H. S., Hao, Q., Leung, T., Lawrence Wong, K., Nygaard, H., Hasenkam, J. M., and Johansen, P. (2008). Embolic doppler ultrasound signal detection using continuous wavelet transform to detect multiple vascular emboli. *Journal of neuroimaging*, 18(4):388–395.
- Organization, W. H. (2000). *The world health report 2000: health systems: improving performance*. World Health Organization.
- Padayachee, T., Parsons, S., Theobald, R., Linley, J., Gosling, R., and Deverall, P. (1987). The detection of microemboli in the middle cerebral artery during cardiopulmonary bypass: a transcranial doppler ultrasound investigation using membrane and bubble oxygenators. *The Annals of thoracic surgery*, 44(3):298–302.
- Patterson Jr, R., Kessler, J., Brennan, R., and Twichell, J. (1972). Ultrasonic detection of microemboli from artificial surfaces: evidence of microembolic tissue damage. *Bulletin of the New York Academy of Medicine*, 48(2):452.
- Piorkowski, M., Kläffling, C., Botsios, S., Zerweck, C., Scheinert, S., Banning-Eichenseher, U., Bausback, Y., Scheinert, D., and Schmidt, A. (2015). Postinterventional microembolism signals detected by transcranial doppler ultrasound after carotid artery stenting. *Vasa*, 44(1):49–57.
- Ringelstein, E. B., Droste, D. W., Babikian, V. L., Evans, D. H., Grosset, D. G., Kaps, M., Markus, H. S., Russell, D., Siebler, M., et al. (1998). Consensus on microembolus detection by tcd. *Stroke*, 29(3):725–729.

-
- Russell, D. (1995). The size of cerebral microemboli in prosthetic heart-valve patients. In *Stroke*, volume 26, pages 733–733. AMER HEART ASSOC 7272 GREENVILLE AVENUE, DALLAS, TX 75231-4596.
- Serbes, G., Sakar, B., Aydin, N., and Gulcur, H. (2014). An emboli detection system based on dual tree complex wavelet transform. In *XIII Mediterranean Conference on Medical and Biological Engineering and Computing 2013*, pages 819–822. Springer.
- Serbes, G., Sakar, B. E., Gulcur, H. O., and Aydin, N. (2015). An emboli detection system based on dual tree complex wavelet transform and ensemble learning. *Applied Soft Computing*, 37:87–94.
- Siebler, M., Sitzer, M., Rose, G., Bendfeldt, D., and Steinmetz, H. (1993). Silent cerebral embolism caused by neurologically symptomatic high-grade carotid stenosis. *Brain*, 116(5):1005–1015.
- Silbert, B., Evered, L., Scott, D., Rahardja, S., Gerraty, R., and Choong, P. (2014). Review of transcranial doppler ultrasound to detect microemboli during orthopedic surgery. *American Journal of Neuroradiology*, 35(10):1858–1863.
- Smith, J. L., Evans, D. H., Fan, L., Bell, P. R., and Naylor, A. R. (1996). Differentiation between emboli and artefacts using dual-gated transcranial doppler ultrasound. *Ultrasound in medicine & biology*, 22(8):1031–1036.
- Spencer, M. P. (1992). Detection of cerebral arterial emboli. *Transcranial doppler*, 19:215–230.
- Spencer, M. P., Thomas, G. I., Nicholls, S. C., and Sauvage, L. R. (1990). Detection of middle cerebral artery emboli during carotid endarterectomy using transcranial doppler ultrasonography. *Stroke*, 21(3):415–423.
- van Zuilen, E. V., Moll, F. L., Vermeulen, F. E., Mauser, H. W., van Gijn, J., and Ackersstaff, R. G. (1995). Detection of cerebral microemboli by means of transcranial doppler monitoring before and after carotid endarterectomy. *Stroke*, 26(2):210–213.
- WHO (2014). *World Health Organization*.
- WHO, W. H. O. (2010). *World health statistics 2010*. World Health Organization.

Appendix

Appendix A

Size estimation of the smallest detected micro-emboli

In an original step, we desire to calculate the actual size of the smallest micro-embolic signature that we have detected. For this purpose, we perform size calculations based on the relation stated by Moehring and Klepper (1994) and Evans (2003), in which the relative intensity increase of an embolus is given as a function of the backscattering cross section of the blood red blood cells and the backscattering cross section of the embolus itself.

$$RelativeIntensityIncrease = \frac{\sigma_{bloodEmb}}{\sigma_{blood}}. \quad (A-1)$$

with $\sigma_{bloodEmb}$ = the backscattering cross section from the blood when an embolus is present in the sample volume

and σ_{blood} = the backscattering cross section from the blood alone in the sample volume. It is calculated as:

$$\sigma_{blood} = N_{RBC} \times \sigma_{RBC} \quad (A-2)$$

where N_{RBC} is the number of RBCs and σ_{RBC} the backscattering cross section of one RBC given by:

$$\sigma_{RBC} = 4\pi \frac{V_{RBC}^2 \pi^2}{\lambda_0^4} \left[\frac{\kappa_{RBC} - \kappa_0}{\kappa_0} + \frac{\rho_{RBC} - \rho_0}{\rho_{RBC}} \cos(180^\circ) \right]^2 \quad (A-3)$$

where V_{RBC} is the volume of one red blood cell calculated as:

$$V_{RBC} = \frac{4}{3} \pi R^3 \quad (A-4)$$

with the red blood cell assumed to be a sphere of radius R approximately around $3.5 \mu\text{m}$ (Jensen, 1996). $\lambda_0 = 385 \mu\text{m}$ is the wavelength calculated from a frequency $f_0 = 4\text{MHz}$. κ_{RBC} and ρ_{RBC} are respectively the adiabatic compressibility and density of the red blood cell. They show small perturbation from the mean values κ_0 and ρ_0 of the medium (plasma) surrounding them. The values of the mass density and adiabatic compressibility for the red blood cells are $1.092 \text{ (g/cm}^3\text{)}$ and $34.1 \text{ (} 10^{-12} \text{ cm/dyn)}$ respectively. The values of the mass density and adiabatic compressibility for plasma are $1.021 \text{ (g/cm}^3\text{)}$ and $40.9 \text{ (} 10^{-12} \text{ cm/dyn)}$ respectively (Jensen, 1996).

Since V_{RBC} is the volume of one red blood cell and hematocrit, H , is the ratio of the red blood cells' volume to the total blood volume, the number of red blood cells N_{RBC} can be written as:

$$N_{RBC} = \frac{H}{V_{RBC}}. \quad (A-5)$$

Hence, the backscattering from the whole blood can be calculated as:

$$\sigma_{blood} = \frac{H}{V_{RBC}} \times \sigma_{RBC}. \quad (A-6)$$

On another hand, the backscattering cross section from the blood when an embolus is present in the sample volume $\sigma_{bloodEmb}$ can be given as the sum of the backscattering from the blood and the backsacterring from the embolus:

$$\sigma_{bloodEmb} = \sigma_{bloodE} + \sigma_{Emb} \quad (A-7)$$

Without loss of generality, by considering the embolus as a large RBC, the backscattering cross section of an embolus is given as:

$$\sigma_{Emb} = 4\pi \frac{V_{Emb}^2 \pi^2}{\lambda_0^4} \left[\frac{\kappa_{Emb} - \kappa_0}{\kappa_0} + \frac{\rho_{Emb} - \rho_0}{\rho_{Emb}} \cos(180^\circ) \right]^2 \quad (A-8)$$

where V_{Emb} is the quantity to be inferred, and from which we can calculate the radius of the embolus by

$$V_{Emb} = \frac{4}{3} \pi R_{Emb}^3 \quad (A-9)$$

κ_{Emb} and ρ_{Emb} are respectively the adiabatic compressibility and density of the embolus. The two quantities are given as $\rho_{Emb} = 928 \text{ kg/m}^3$ and

$$\kappa_{Emb} = \frac{1}{\rho_{Emb} \cdot c^2}. \quad (A-10)$$

σ_{bloodE} is the backscattering cross section backscattered by the rest of the blood that is not occupied by the embolus. In other words, it is that backscattered by the RBC that are not replaced by an embolus. It can be modeled as follows:

$$\sigma_{bloodE} = N_{RBC} \times \sigma_{RBC} - n \times \sigma_{RBC} \quad (A-11)$$

where n is the number of RBCs that the present embolus replaces.

However, in most cases $n \ll N_{RBC}$ and thus n can be neglected and σ_{bloodE} is the same as σ_{blood} .

The upper calculations, performed on the smallest detected emboli we presented in the chapters of part II, supplied the following diameters:

Table 1: The calculated diameters for the smallest detected micro-emboli

Detection Method	Relative Intensity Increase of the smallest detected embolus (dB)	Diameter (μm)
Whole band detection with constant empirical thresholds	5.8 dB	91.47 μm
Sub-band detection with constant empirical thresholds	2.6 dB	74.53 μm
Whole band detection with constant statistical thresholds	4.1 dB	83.06 μm
Sub-band detection with constant statistical thresholds	2.3 dB	72.56 μm
Whole band detection based on negative energy fluctuations	0.8 dB	59.02 μm
Sub-band detection based on negative energy fluctuations	0.55 dB	55.18 μm
Detection based on skewness calculations	1.6 dB	67.33 μm
Detection based on kurtosis calculations	1.6 dB	67.33 μm